Diesel Nozzle Flow and Spray Formation: Coupled Simulations with Real Engine Validation

A thesis accepted by the Faculty of Aerospace Engineering and Geodesy of the Universität Stuttgart in partial fulfilment of the requirements for the degree of Doctor of Engineering Sciences (Dr.-Ing.)

by

Dipl. Ing. Daniele Suzzi

Born in Bologna, Italy

main referee: Prof. Dr.-Ing. habil. Bernhard Weigand

co-referee: Prof. Dr. rer. nat. habil. Claus-Dieter Munz

Date of defence: 6. April 2009

Institute of Aerospace Thermodynamics

Universität Stuttgart

2009

Contents

List of Symbols

Latin Symbols

Symbol	Coherent SI Unit	Quantity
A	[m^2]	Area
B_T	[-]	Temperature transfer number
B_Y	[-]	Mass transfer number
c	[-]	Local surface curvature
c_p	[J/kg K]	Specific heat capacity at constant pressure
d	[m]	Droplet diameter
D	[kg/s]	Drag function
e	[J/kg]	Specific internal energy
F	[N]	Force
f	[-]	Function
f_d	[s/K m^5]	Distribution function
g	[m/s^2]	Gravity
h	[J/kg]	Specific enthalpy
H	[W/m^2]	Enthalpy source term
h_m	[m/s]	Mass Transfer Coefficient
I	[-]	Unity tensor
k	[W/(m K)]	Heat conductivity
K, C	[-]	Coefficient, factor
L	[J/kg]	Latent heat
L_i	[m]	Length scale
m	[kg]	Mass
M	[Kg/m s^2]	Interfacial momentum source
n	[-]	Number of phases
N	[1/m^3]	Number density
p	[Pa]	Pressure
P, G	[-]	Production or destruction terms
q	[W/m^3]	Volumetric heat source

Symbol	Coherent SI Unit	Quantity
r	[m]	Radius
S_i	[-]	Sources
t	[s]	Time
T	[K]	Temperature
T_{ij}	[Pa]=[N/m^2]	Reynolds stress tensor
u, v	[m/s]	Velocity
u, v, w	[m/s]	Velocity components in Cartesian coordinates
V	[m^3]	Volume
w_{ij}	[-]	Weighting factor
x	[m]	Position
x, y, z	[m]	Cartesian coordinates
Y	[-]	Mass fraction
$y+$	[-]	Non-dimensional wall distance
z_{mean}	[-]	Mixture fraction

Greek Symbols

Symbol	Coherent SI Unit	Quantity
σ	[N/m]	Surface tension
σ_S	[W/(m^2 K^4)]	Stefan-Boltzmann constant
α	[m^2/s]	Thermal diffusivity
α_i	[-]	Phase volume fraction
Γ	[kg/s]	Mass source term
ε	[m^2/s^3]	Turbulent dissipation
ε	[-]	Emissivity (radiation)
θ	[-]	Void fraction
κ	[m^2/s^2]	Turbulent kinetic energy (TKE)
λ	[m]	Wave length
μ	[Pa s]=[N s/m^2]	Dynamic viscosity
ν	[m^2/s]	Kinematic viscosity (=μ/ρ)
ρ	[kg/m^3]	Density
τ	[s]	Time scale
τ_{ij}	[Pa]=[N/m^2]	Shear stress tensor
Φ	[J/m^3]	Dissipation function
ϕ	[-]	Volumetric source term

Subscripts and superscripts

Symbol	Quantity
$\rightarrow$	Vector
$\cdot$	Rate of change or flux
∞	Free-stream
— *(overbar)*	Average value
$\wedge$	Instantaneous value
$\acute{}$	Fluctuation
a	Aerodynamic
B	Break-up
C	Collision/coalescence
d	Droplet
D	Drag
diff	Diffusion
E	Evaporation
e	Energy
eff	Effective value
EX	External
g	gas
G	Gravity and buoyancy
i, j, k, l	Indices
inj	Injection
int	Interface
l	Liquid
max, min	Maximum and minimum
P	Pressure
p, v, T, etc	At constant value of property
PB	Primary break-up
ref	Reference
rel	Relative
S	Surface value
s	Exchange function
SB	Secondary break-up
t	Turbulent
T	Turbulent dispersion
v	Vapour
vap	Vaporization

Dimensionless numbers

Symbol	Quantity
Le	Lewis number $(=Sc/Pr)$
Pr	Prandtl number $(=c_p\mu/k)$
Re	Reynolds number $(=uL/\nu)$
Sc	Schmidt number $(=\nu/D)$
Sh	Sherwood number $(=h_mL/D)$
We	Weber number $(=u^2L\rho/\sigma)$

Abbreviations

BDC	Bottom Dead Center
CFD	Computational Fluid Dynamics
DDM	Discrete Droplet Model
DI	Direct injection
FD	Finite Difference
FE	Finite Element
FV	Finite Volume
HCCI	Homogenous Charge Compression Ignition
IC	Internal Combustion
LDA	Laser Doppler Anemometry
PDA	Phase Doppler Anemometry
RANS	Reynolds Averaged Nevier-Stokes
TDC	Top Dead Center

Abstract

The main task of the engine 3D CFD simulation is to support combustion design development. New combustion concepts (e.g. Low Temperature Combustion, HCCI, multiple injection strategies …) can be analyzed and predicted by detailed thermo-dynamical computation. To achieve this aim many simulation tools are needed: each of them should be capable of reproducing the sensitivities of combustion design parameters through physically based models.

Experiments on DI Diesel engines show that different nozzle geometry at the same operative conditions can lead to dramatically different behaviors in emissions formation. The adoption of different nozzle configurations (Sac-hole, VCO …) with analogous specific mass flow and load pressure strongly affect mixture and therefore emissions formation. Nevertheless, the relation between local nozzle flow and spray development in the combustion chamber is still a challenging topic with a high improvement potential.

Nowadays simulation tools focus on singular aspects of a Diesel internal combustion engine: cavitating nozzle flow, spray, mixture formation, combustion and emissions. Simulation of transient nozzle flow provides information about the initialization of spray, whose actual standard is based on the Discrete Droplets Method (DDM). A step further consists of the adoption of a 3D-Eulerian Spray multiphase model, which allows a stochastic and physical improvement in the description of spray formation. The combustion process is then usually modeled on a single-phase solver with transport equations for the scalar species and chemistry-based models for emissions formation. The missing link in the simulation chain is between the Eulerian spray and the combustion calculation. The focal aim of the work will be the coupling of different models for 3D-nozzle flow, orifice-resolved primary breakup and mixture formation. The transient cavitating flow inside the injector body is combined to the Eulerian spray in an orifice resolved region just outside the nozzle hole. Primary break-up assumptions allow then to transfer the dynamic and turbulent boundary conditions from the injector orifice to the spray. The further engine domain is simulated in the classical one-phase approach, with spray transport via DDM model. The two codes for Eulerian spray and combustion are real-time coupled: source terms and boundary conditions are constantly mapped and exchanged between the solvers in order to achieve physical consistency. The coupling method implies the three-dimensional intersection of both computational domains and the exchange of data at defined interfaces.

The final achievement of the thesis is a technique, which could reproduce the nozzle flow effects on the 3D simulation of engine combustion cycle, together with an advanced physical and statistical treatment of mixture formation process.

The advantages of the method will be proven on an operative truck engine case, for which a complete set of experimental data (pressure curves, integral emissions level and transparent engine images) is available. The validation is performed on two different nozzle geometries, with the same specifications in terms of mass flow and maximum rail pressure: a sac-hole and a sac-less (VCO) nozzle. The Eulerian Spray will be coupled with previous transient nozzle flow simulations and validated through experiments on an optically accessible high-pressure chamber.

Kurzfassung

Die Hauptaufgabe von dreidimensionalen numerischen Motorsimulationen ist die Unterstützung der Verbrennungsdesignentwicklung. Neue Verbrennungskonzepte können durch detaillierte thermodynamische Berechnungen analysiert und vorausgesagt werden. Um dieses Ziel zu erreichen, benötigt man eine Reihe von Simulationstools, die die Sensitivität von Verbrennungsdesignparametern durch physikalisch basierte Modelle reproduzieren können.

Versuche an Dieselmotoren mit Direkteinspritzung zeigen, dass unterschiedliche Düsengeometrien unter gleichen Betriebsbedingungen zu dramatisch unterschiedlichem Schadstoffbildungsverhalten führen können. Der Einsatz von verschiedenen Düsenkonfigurationen (Sackloch, Sitzloch, …) mit vergleichbarem spezifischem Massendurchfluss und Leitungsdruck hat einen großen Einfluss auf die Gemisch- und Schadstoffbildung. Auch der Zusammenhang zwischen lokaler Düseninnenströmung und der Strahlentwicklung im Brennraum ist noch ein herausforderndes Thema mit hohem Verbesserungspotential und daher Inhalt dieser Arbeit.

Die Simulationstools setzen heutzutage den Akzent auf einzelne Aspekte der Dieselverbrennungsmotoren, z.B. kavitierende Düseninnenströmung, Strahl, Gemischbildung, Verbrennung und Emissionen. Die transiente Berechnung der Strömung in der Düse liefert Informationen über die Initialisierung des Sprays, dessen aktueller Standard auf der „Discrete Droplets Method" basiert. Ein weiterer Schritt besteht aus dem Einsatz von einem 3D-Euler'schen Strahlmodell, dass eine stochastische und physikalische Verbesserung in der Beschreibung der Spraybildung erlaubt. Der Verbrennungsvorgang ist dann in der Regel durch einen einphasigen Solver mit Transportgleichungen für Skalare und chemiebasierten Ansätzen für die Schadstoffbildung modelliert. Das fehlende Verbindungsglied in der Simulationskette befindet sich zwischen dem Euler'schen Spray und der Verbrennungsrechnung. Das Hauptziel dieser Arbeit ist die Kopplung von unterschiedlichen Modellen für dreidimensionale Düseninnenströmung, düsenaufgelösten Primärzerfall und Gemischbildung. Die transiente kavitierende Strömung im Düsenkörper steht mit dem Euler'schen Spray über ein direkt an das Düsenloch anschließendes Rechengebiet in Verbindung. Annahmen im Primärzerfall erlauben die Übertragung von dynamischen und turbulenten Randbedingungen vom Injektor zum Strahl. Die übrige Motordomäne ist mit der klassischen einphasigen Methode und Lagrange'schen Spraytransport berechnet. Die beiden Codes für Euler'schen Spray und Verbrennung sind echtzeitgekoppelt, d.h. dass die Quellterme und Randbedingungen ständig zwischen den Solvern projiziert und ausgetauscht werden um die physikalische Konsistenz zu erfüllen. Die Kopplungsmethode enthält eine dreidimensionale Überschneidung von beiden Rechengebieten und Datenübertragung an bestimmten Schnittstellen.

Das Endergebnis dieser Doktorarbeit ist eine Technik, die den Einfluss einer Düseninnenströmung auf die dreidimensionale Simulation eines Verbrennungsmotors, zusammen mit einer erweiterten physikalischen und statistischen Behandlung des Gemischbildungsprozesses, abbilden kann. Die Vorteile der Methode werden an einem Nutzfahrzeugmotor, für den ein komplettes Set von Messungen (Druckverläufe, integrale Emissionen und Bilder des transparenten Motors) verfügbar ist, untersucht. Die Validierung erfolgt auf zwei unterschiedlichen Düsengeometrien, einer Sackloch- und eine Sitzlochdüse, mit gleichen Spezifikationen für Massenstrom und maximalen Ladedruck. Der Euler'sche Spray wird mit den vorigen instationären Düseninnenströmungsrechnungen gekoppelt und mit Ergebnissen von einer optisch zugänglichen Hochdruckkammer validiert.

1. Introduction

1.1. Motivation

The advancement of progress led people to assume mobility as an everyday necessity. In the last decades connections and globalization contributed in shrinking the world and part of this process is surely due to the spread of internal combustion vehicles, whose development started after the explosion of the industrial revolution [71].

The impact of fuel exhausts on air quality and human health increased together with the accessibility of vehicles, above all in urban areas of high traffic density. The effects of exhaust gases on people were originally underestimated, nevertheless in the last years governments have concentrated more attention on the topic, as the poor air quality considerably increased respiratory and cardiovascular diseases. In order to contain the harmful vehicles emissions, the European Union has imposed emissions limits on all sold passenger cars since 1983 [18]. The pollutants that cause the most serious health problems are nitrogen oxides (NOx) and particulate matter (PM), even if carbon monoxide (CO) and unburned hydrocarbons (HC) are partly responsible for global heating and climate exchanges. The development of emissions standard for Diesel passenger vehicles is shown as an example in Figure 1.1.

Currently discussions on CO_2 emissions strongly blew up, mainly due to climatic changes and global warming. Engine consumption and efficiency gained increasing importance, leading automotive companies to invest in research on alternative techniques like hybrid, bio-fuels or hydrogen engines. As the development of these new concepts and the consequent distribution of new fuels could not be expected in the next few years, the short term objectives lie on the enhancement and the optimization of actual engine concepts.

The actual work focuses on Diesel engines for passenger cars and trucks, from which emissions of nitrogen oxides (NOx) and particulate matter (PM) are higher than for gasoline vehicles. The latter EU exhausts measure for cars is known as Euro 5 and will become valid during 2009: the new limit for particulate emissions from diesel is reduced by 80% compared to Euro 4. Carmakers are therefore more and more focused on technologies to optimize diesel engines in terms of fuel economy, power and, of coarse, exhausts reduction. Many technical factors directly affect quantity and composition of emissions, such as workload demand, engine type and tuning, atmospheric conditions or fuel quality. Also fuel development is necessary in order to meet the stronger emissions limits: an example is the introduction of unleaded gasoline to meet the Euro 1 standard.

In the strain to enhance engine efficiency and combustion processes, CAE (Computer Aided Engineering) methods and in particular CFD (Computational Fluid Dynamics) gained an important role in the recent years. The main reasons can be found on test bench costs and on the constantly increasing quality of simulation results, together with an improved

understanding of local phenomena, which could be hardly or impossibly detected from experimental techniques on a complete engine.

The main focus of this work is the modeling and prediction of DI (Direct Injection) diesel combustion, with a particular attention on the overall process of mixture formation, which represents a fundamental basis in obtaining a more efficient combustion and reducing pollutants.
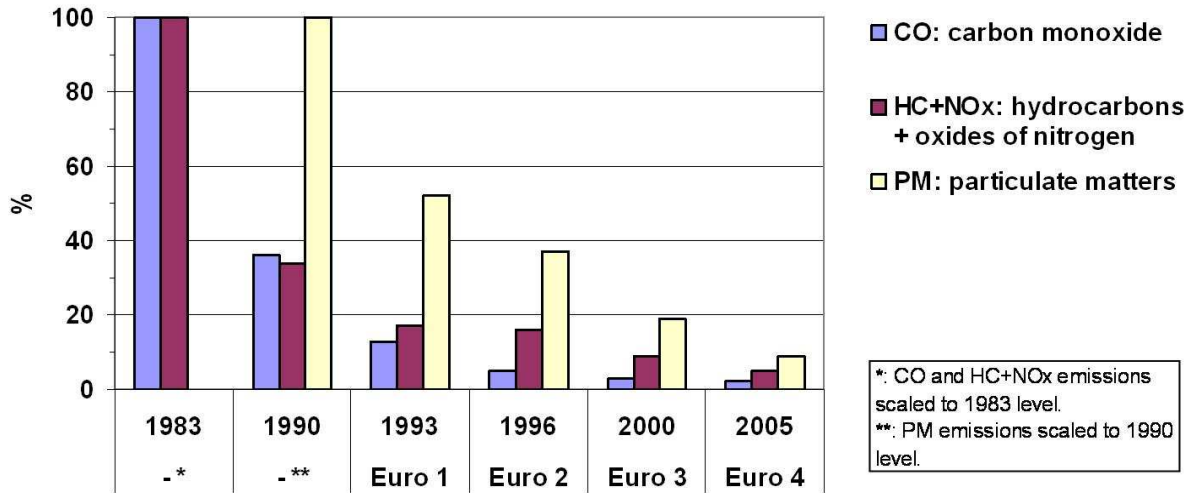

Figure 1.1: Emission standard development for Diesel engines in the EU (1983-2005) [18].

1.2. Objectives

The main goal of the work is to develop a simulation method that could describe the basics of a DI diesel engine, respectively nozzle flow, mixture formation and combustion. A summary of simulation methodology will be presented in Chapter 2, in order to get an overview of CFD fundamentals for 1-phase and multiphase solvers.

One of the most important aspects for a CFD analysis of combustion is the mixture preparation process, as it represents the fundamental basis on which further ignition and combustion models are built. The standard spray model, the Lagrangian Discrete Droplets Method (DDM), presents some weaknesses in the region near the nozzle outlet. For this reason a multiphase approach is more appropriate to analyze the transition between the continuous flow inside the nozzle and the spray, which rapidly disintegrates into droplets. The 1D ICAS model and the 3D Eulerian Model, appear the most adequate to simulate the spray formation. In order to understand limits and advantages of the previously described spray models, a detailed overview will be given in Chapter 3.

The effects of modern injection systems, like Common Rail or PLI, could be taken into account starting from the detailed nozzle flow simulation: the cavitation and turbulence development inside the injector body affect further spray formation in a substantial way. For this reason the transfer of orifice flow and turbulent conditions to the spray appears essential to describe the physical behavior of the mixture formation process. All these aspects will be discussed and explained in Chapter 4.

As mentioned, the Eulerian spray approach is suitable to describe the region near the nozzle orifice. Nevertheless, in the dilute spray region the nearly absence of already evaporated droplets, the robustness of scalar-controlled combustion models and the numerical efficiency

of 1-phase solver suggest the employment of the standard DDM Lagrangian model for droplets treatment. A disadvantage of the state-of-the-art methods is the lack of a coupling procedure between all the simulation tools. The requirement is therefore a link between the different numerical models specialized for a distinct part of the engine. The aim of this thesis is to couple all the highest quality simulation methods for nozzle flow, spray formation and combustion in order to make a step forward in the prediction of engine behavior. The crucial point will be the development of an interface between the different CFD codes. The physical data exchange and the spatial mapping between simulation grids will be shown in Chapter 4. Particular emphasis will lie on the motor application of the method and attempt to underline the advantages that such a procedure could supply in CAE applications. Nozzle geometry effects on spray formation and combustion will be therefore simulated and presented in Chapter 5.

1.3. State of the art

The following paragraphs give an overview of actual simulation methods in terms of combustion, injection systems internal nozzle flow, spray formation and coupling of codes. A large amount of literature extends beyond the mentioned fields: the main focus will be on the milestones, which actually permit the development of the current work. The analysis of experimental set ups and methods will only be quoted and not exhaustively outlined.

1.3.1. Combustion

The most diffused combustion concepts are shown in Figure 1.2. In gasoline engines, working in homogeneous conditions, fuel injection takes place in the intake manifold and mixture is ignited inside the cylinder by a sparkplug. The GDI (Gasoline Direct Injection) engines present the gasoline injector directly in the cylinder, leading to a stratified combustion concept, as before governed by a sparkplug ignition. In diesel DI engines the fuel is introduced directly in the combustion chamber and the self-ignition usually takes place on spray borders due to high pressure and temperature.


(a) Gasoline   **(b) GDI**   **(c) Diesel**   **(d) HCCI**
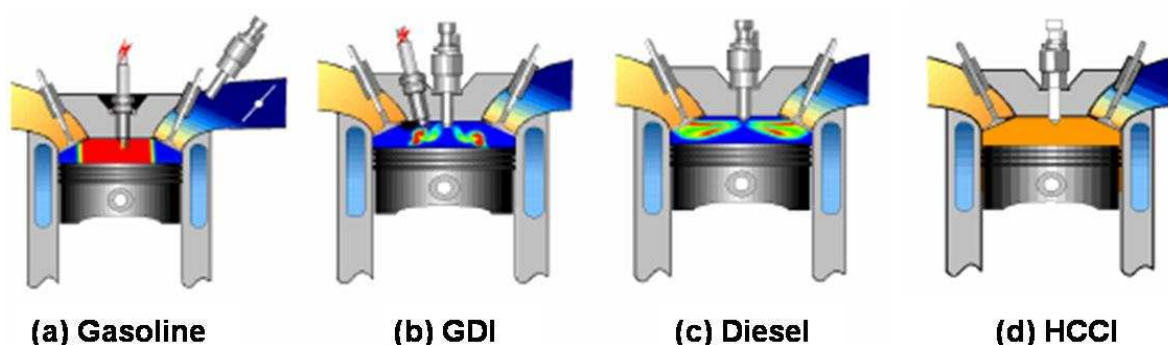
Figure 1.2: Principles of combustion process [44].

Due to inhomogeneous mixture distribution, diesel DI combustion leads locally to over stoichiometric fat zones, which are ideal for particulate formation. On the other hand nitrogen oxides are created in zones of lean mixture and high temperature. However NOx could be easier reduced than soot via catalyst exhaust systems.

The homogenous charge compression ignition (HCCI) [87] is one of the last concepts in terms of diesel combustion. It is based on the idea of getting the self-ignition when the mixture is homogeneous and lean: thanks to this no soot particles will be built and, furthermore, the low temperatures would lead to very low nitrogen oxides production. The problem of the concept is that in part load the air supply needs to be throttled, which means higher flow losses and consequently increased fuel consumption.

The 3D simulation of reactive in-cylinder flow dynamics is gaining more importance in combustion design, thanks also to the rapid increase of computing power. Of course the industrial requirements force the strain on combustion models with an acceptable degree of predictability and restricted computational costs. The aim is therefore to incorporate detailed turbulent flow prediction together with complex chemistry.

There are many approaches to predict the Diesel combustion process, from the old Magnusson model to the most recent ECFM3Z, Flamelet or Mixing Timescale [85]. In the present work the PDF-Timescale model [86] will be used, with the solution of chemical timescales based on detailed chemistry computations. The basic idea is to define a limited number of progress variables in order to describe the reactive phases of self-ignition and premixed and diffusion combustion (see Figure 1.3, a). This is important if cool flame effects occur and for analysing HCCI engine configurations.


| (a) | (b) |
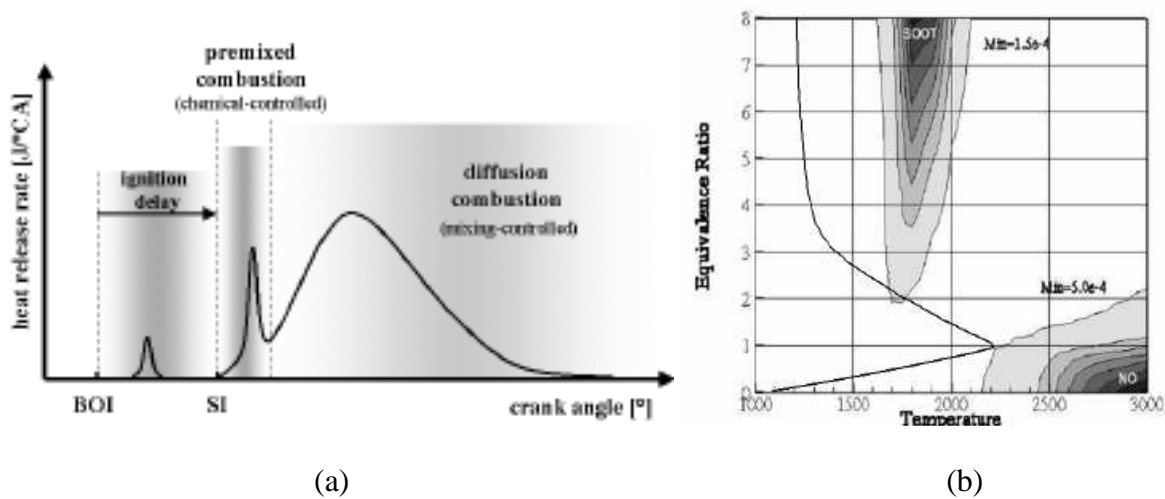
Figure 1.3: Diesel combustion phases (a) [85] and thermo-chemical regions for emissions formation (b) [5].

The CFD code resolves a transport equation for each progress variable and the mixture field is characterized in physical space by a mean fraction and its variance. Each transport equation is therefore closed through the stochastic weighting of the chemical solution with a probability density function (PDF), which accounts for turbulent mixture effects. The main goal of the method is to separate the solution of turbulent flow field from that of chemistry: consequently arbitrary complex chemistry could be associated to calculate the reaction progress.

Emissions formation is strongly dependent on thermodynamic local conditions inside the combustion chamber. According to temperature and mixture fraction space at a defined EGR (Exhaust Gas Recirculation) rate, it is possible to identify regions where Soot and NOx generate, as schematically shown in Figure 1.3, b. Soot formation, oxidation and size distribution could also be modelled through detailed chemistry assumptions [94].

1.3.2. Injection Systems and Nozzle Flow

In terms of diesel direct injection (DI) systems, the common rail (CR) and the pump-line injector (PLI) are the mostly used injectors [50]. Conceptually, the main difference exists in the way the load pressure is transmitted to the single injectors. While in the PLI system each injector is provided with a pump moved by the camshaft, the CR presents a high-pressure chamber connected to each nozzle [73]. In CR systems the rail rules the load pressure, thus it always remains practically at the same level, which could reach values up to 2200 bar. The PLI system generates a load pressure that increases during the injection period as effect of the camshaft rotation. In this case the maximal pressure is of the order of 2500 bar.

The presence of a constant load pressure in CR systems allows pre- and post-injection strategies, which lead to better driving comfort and emissions control. On the other hand, PLI injectors appear better to reduce NOx in engines running with low EGR, as the needle could open very fast while the load pressure increases slowly, leading to limited injected mass, weaker atomization and slower combustion process.

Another essential component of an injection system is the nozzle. Actually many types are produced and employed, even if the main classification could be made between sac hole and valve covered orifice (VCO) nozzles. Assuming the same injector system, barely different nozzle geometries create huge effects on exhaust gases, as shown in Figure 1.4 on production of soot.
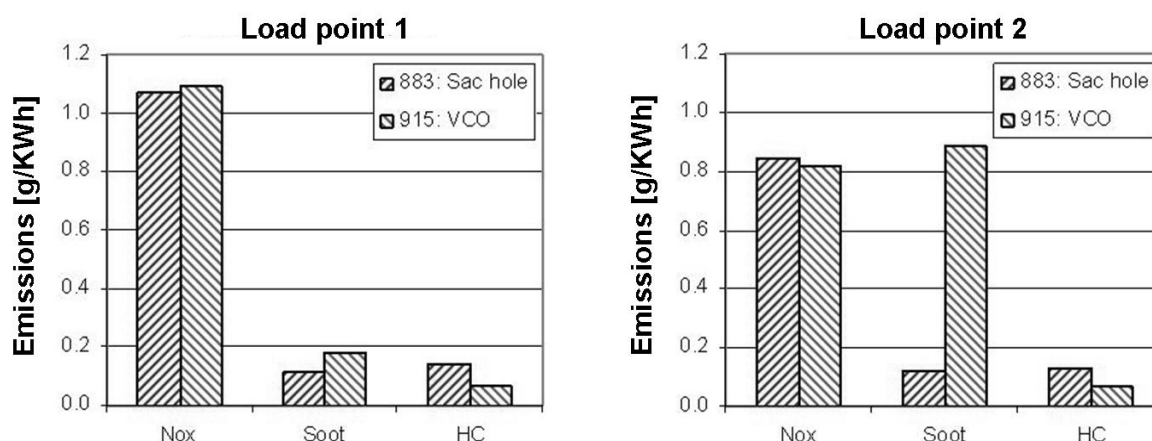

Figure 1.4: Emission production for a CR Diesel engine at different load points and with dissimilar nozzle geometries (Courtesy of DaimlerChrysler Group Research).

As presently shown, injector geometry and hence its internal flow have big effects on spray formation. Furthermore the occurrence of cavitation could imply not only flow perturbations, but also erosion and mechanical stresses on injector body. A deep understanding of dynamic and turbulent phenomenon inside the nozzle could provide improvement on the whole combustion design process. In any case, experiments are difficult to manage, due to the small scale, in the order of microns, and the high-speed of the flow, up to more than 500 m/s. For this reason internal nozzle flow simulations acquired an increasing role in engine development. Also in simulation of 3D CFD combustion processes, the knowledge of injected mass flow rate and flow asymmetries at nozzle orifice appear to be a key issue. Only a two phase flow model accounting for liquid and cavitation vapour seems to be able to provide an exhaustive description of the phenomenon. An example of capabilities of 3D cavitating nozzle flow simulation is shown in Figure 1.5: the agreement with experiments on transparent injectors allows considering this kind of calculation as a reliable tool.
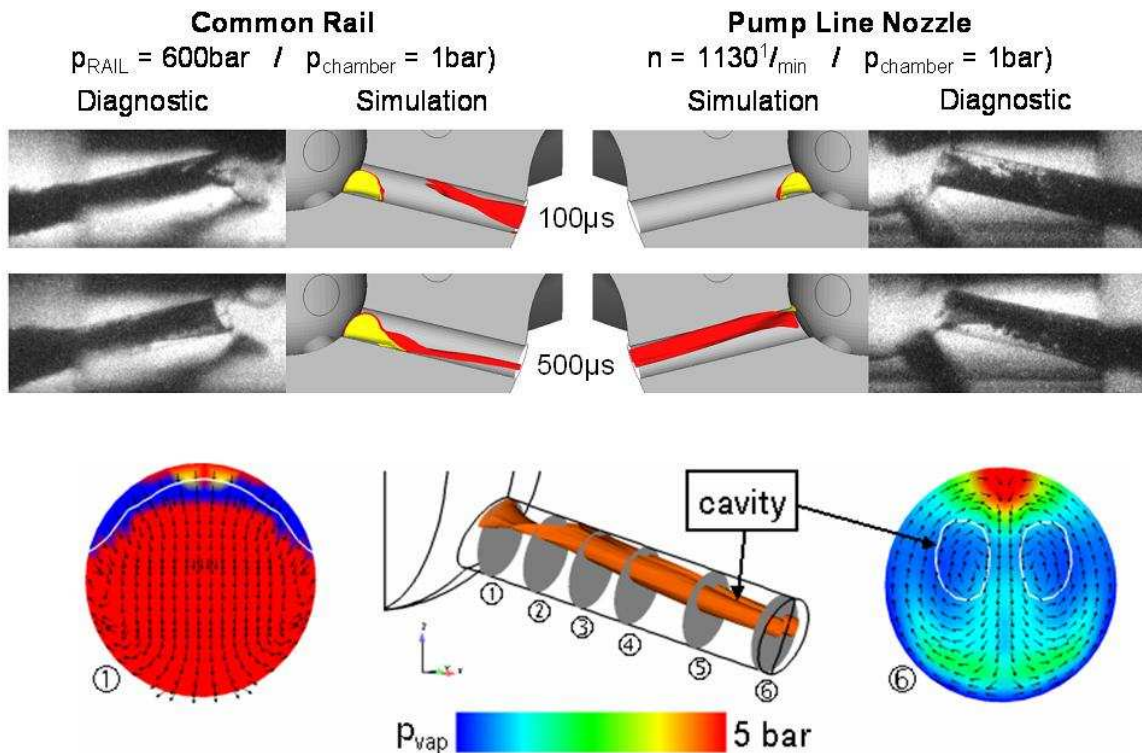
Figure 1.5: Examples of Nozzle Flow simulation with different injection systems in comparison with experiments (up) and detailed [52].

1.3.3. Spray

The fuel spray represents a very important aspect of combusting systems, as it's shape and composition strongly affects the ignition and flame propagation processes. Therefore, the simulation of mixture formation is a critical precondition for the further CFD calculation of combustion in IC engines. Historically [47], the first idea was to adopt a one-phase solver for the gas, in which the droplets were coupled as a carried property (Discrete Droplet Method, DDM). Spray parcels are therefore followed during their motion with a Lagrangian approach, while gas is modeled with a grid-based Eulerian RANS solver.

Another way is to consider the spray as a mixture of liquid and gas with a certain number of droplet classes, each of them bound to follow the conservation equations: this is the multiphase approach [12]. If the droplets-air drag interaction could be modeled with a Lagrangian/Eulerian or Eulerian/Eulerian assumption, many sub-models are needed to reproduce the evolution of spray parcels diameters and their interaction with the turbulent environment. Primary and secondary [67] atomization processes, evaporation [79], turbulent dispersion [25] or collision [56] are some of the most important aspects, which have been studied around the spray phenomenon.

Experimental results play a very important role in spray modeling. Detailed physical assumptions need constant development of investigation techniques. Visualization methods could help to understand spray development and break-up, both in cold and hot running chambers [14]. Also single droplets experiments are needed to define the small scale behavior of spray parcels, for example concerning the modeling of multi-component [96] or high pressure [90] evaporation.

1.3.4. Code Coupling

The expansion of complexity of new simulation methods and physical models led to a spread of multi-disciplinary knowledge. A single CFD code is often unable to ensure a comprehensive analysis of complex physical systems. Furthermore, in many cases the simulation of stand-alone phenomena reveals itself as a limit towards the solution of a real problem. The coupling of different simulation tools, each specialized in different physical aspects, is therefore becoming more and more important both in industrial and university based research applications. Thermal coupling, fluid-structure interaction or magneto-hydro dynamics are some examples of possible coupling applications. For instance, the high temperature gradients on an exhaust gas manifold lead to strong heat transfer and structure deformation, which could strongly affect the gas flow in a multi-cycle analysis (Figure 1.6 left). Another example could be the interaction of a fluid in motion with a rigid body (Figure 1.6, right): the structure is subjected to a pressure gradient and deforms its body under the effect of stress; analogously the fluid flow is affected by the modified geometry boundaries. To ensure the effectiveness of simulation and the quality of prediction, the coupling should be performed in real-time.


(a)   (b)
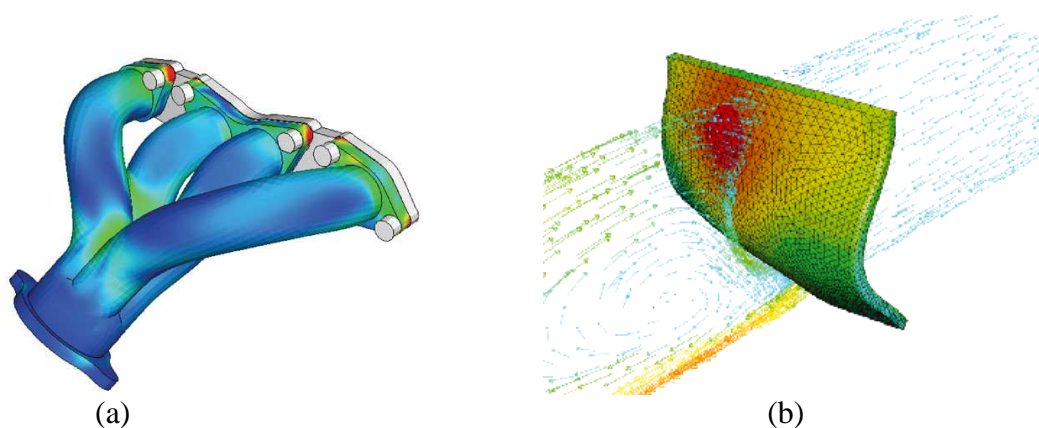
Figure 1.6: Coupled simulations of heat transfer between hot exhaust stream and car's manifold (Image courtesy of Fluent Inc. and ABAQUS) (a) and fluid-structure interaction (Fraunhofer-Institut SCAI; [29]) (b).

Sometimes not only numerical approaches are different (i.e. FV, FD or FEM), but also the codes are developed from different institutions, each one specialized on a particular topic. For this reason the solution appeared to be the connection of different codes. One example is the MpCCI (Mesh-based parallel Code Coupling Interface) developed by the Fraunhofer-Institut SCAI [29]. This application works like a connection server between different codes and computational domains, performing data transfer and mapping events. The MpCCI supports Fluent, StarCD, ABAQUS, Permas, RadTherm and could be adapted to most of the CAE codes. MpCCI could be seen as a development of the Message Passing Interface (MPI) [81]. AVL has autonomously developed in FIRE an interface called ACCI (AST Code Coupling Interface), which can also couple different codes during the simulation run.

Another basilar aspect of the coupling between codes is the spatial mapping between computational grids. As the current work will focus on CFD-CFD coupling, a general difficulty in simulating fluid flow problems is that a single grid is not always capable of describing complex geometries. In many cases, different grid types best represent different geometrical features. These difficulties could be solved by the construction of a grid system made up of overlapping grids, for example with the Chimera or Overset Grid approach [84]. According to this method a complex geometry is decomposed into a system of geometrically

simple overlapping grids. Furthermore boundary information is exchanged between these grids via interpolation of the flow variables, and many grid points may not be used in the solution (these points are sometimes called hole points). Each block has boundary points, which lie in the interior of a neighboring block (or blocks) and will require information from that containing block. The three steps to setting up an overset simulation are generally grid generation [17], hole cutting [61] and determination of interpolation weights. Usually the single grids can be generated separately. A number of preprocessing packages have been developed, with varying levels of complexity. NASA's PEGASUS [89], which is primarily a grid joining code, takes an existing grid and prepares it for use in an overset simulation.


(a)   (b)
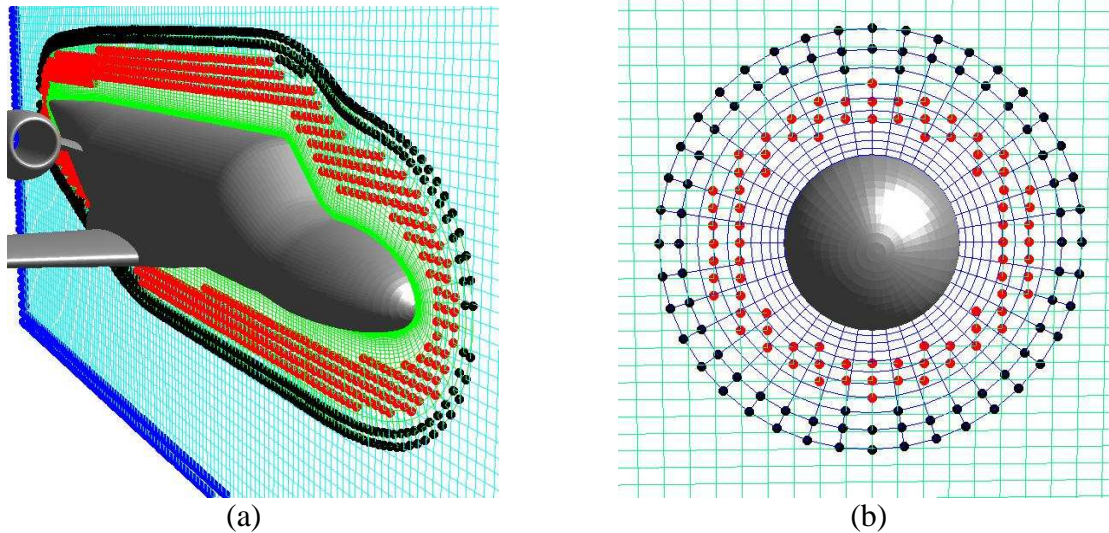
Figure 1.7: Examples of overlapping grids for wing body with Chimera approach [89].

In Figure 1.7 an example of PEGASUS application is shown. The blue lines represent the body grid, while the cyan ones the boxbody grid; red and black symbols are respectively the points receiving data from body and from boxbody.

The Chimera technique is most often associated with traditional finite volume/difference CFD codes, but it can, in principle, be applied with other discretization schemes. The approach developed by AVL and embedded in FIRE v8 assumes a volume intersection method for the mutual transfer of data between the running codes. More details will be presented in Chapter 5 of the current work.

2. Conservation Equations and Numerics

This chapter will address the basic principles of computational fluid dynamics, starting with an overview of its meaning and historical development. Afterwards, numerical approaches for the solution of fluids motion will be addressed. According to requirements of industrial applications, the more suitable simulation approach is the Finite Volume (FV) method [54]: the analysis domain is divided into computational cells where the thermodynamic and fluid dynamic terms acquire volume-averaged values. The main advantage of the FV method is the possibility to mesh complex geometries and to ensure the integral conservation of momentum, mass and energy, at least until rounding and sub-modeling errors. After the description of domain discretization techniques, conservation equations for single-phase flow and modeling of turbulence will be analyzed. Many physical problems, like spray formation or tank filling, need to be treated assuming the existence of two interacting phases. In this case a multiphase approach appears essential to describe the phenomenon. General equations and applications of the multiphase solver will be shortly described in paragraph 2.3, showing also its possible applications.

2.1. CFD Overview

The most common Computational Fluid Dynamics (CFD) applications are the simulation of gases and liquids flows, heat and mass transfer, moving bodies, multiphase physics, chemical reaction, fluid-structure interaction and acoustics. The final results are data and images, which predict the performance of the chosen design.

2.1.1. Historical Background

The study of fluids fascinated mankind since the dawn of civilization [28]. Already in antiquities, the Greek thinker Heraclitus postulated that "Everything flows", even if more in a philosophical sense rather than with scientific connotation. The initiation of hydrostatics, static mechanics and measure of objects density and volume is accountable to Archimedes, whose waterwork studies on aqueducts, canals, harbours and bathhouses were afterwards perfected to a science by the ancient Romans.

These ideas were abandoned until the spark of Renaissance in Southern Europe, where great artists with engineering attitudes started again to observe and study natural flows. Leonardo da Vinci was one of the first to analyse natural phenomena, trying to define their form and

structure in a pictorially way. In a nine-part treatise called "Del moto e misura dell'acqua" (About motion and measurement of water, [48]) he presented new contributions on fluids movement, waves and eddies, as well as studies of free jets, interference of waves and falling water. Some examples of his illustrations are presented in Figure 2.1.
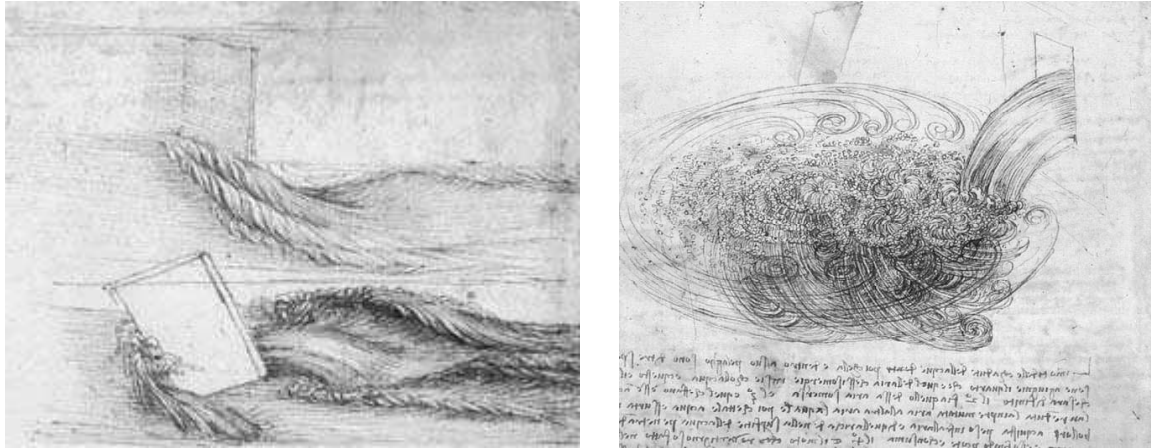

Figure 2.1: Leonardo da Vinci's study of water passing obstacles (l.) and water falling into still water (r.) [48].

In the 17th century Isaac Newton contributed new ideas to the prediction of fluid flow by the introduction of his elementary Newtonian equations. His most important results were the second law of fluid mechanics, the concept of Newtonian viscosity in which stress and rate of strain are linearly interpolated and the relationship between the speed of waves and their wavelength. Another important postulate was the reciprocity principle, stating that the force applied upon a stationary object by a moving fluid is equal to the change in momentum of the fluid deflecting around the object itself.

The following two centuries were marked by enhancements in the mathematical description of fluids motion. While Daniel Bernoulli (1700-1782) derived his famous equation, Leonhard Euler (1707-1783) postulated the conservation of momentum and mass for an inviscid fluid. Claude Louis Marie Henry Navier (1785-1836) and George Gabriel Stokes (1819-1903) made significant contributions to the development of the Euler equations: they introduced viscous transport in the solution of the fluid flow field, obtaining the now famous Navier-Stokes equations. These differential equations for conservation of mass, momentum and energy are still the basis of computational fluid dynamics. Nevertheless, the equations are so closely coupled and difficult to solve that a resolution for real flow problems within reasonable timescales had to wait until the advent of the modern digital computer in the 1960s and 1970s. Other important researchers of the 19th century who developed theories related to the fluids flow are Jean Le Rond d'Alembert, Joseph Louis Lagrange, Siméon-Denis Poisson, Jean Louis Marie Poiseuille, M. Maurice Couette, Pierre Simon de Laplace, John William Rayleigh and Osborne Reynolds.

The 20th century was marked by the efforts on refining theories of boundary layers and turbulence in fluid flow. Many theories of Ludwig Prandtl (1875-1953) are still acknowledged today, as the mixing length concept, compressible flows, boundary layers analyses and the Prandtl number. Other contributions were provided by Theodore von Karman (1881-1963) with his studies on what is now known as the von Karman vortex street and by Geoffrey Ingram Taylor (1886-1975) on a statistical theory of turbulence and the Taylor microscale. Andrey Nikolaevich Kolmogorov (1903-1987) introduced the concepts of universal energy spectrum for turbulence and the Kolmogorov scales, while George Keith Batchelor (1920-2000) contributed to the theory of homogeneous turbulence.

It is difficult to exactly date the first CFD calculation, at least in a modern sense of the term. Lewis Fry Richardson in England (1881-1953) is supposed to have developed the first numerical weather prediction system: he divided a physical space into grid cells and adopted as finite difference approximations the "primitive differential equations" of Bjerknes. The simulation of weather for an eight-hour period took six weeks of real time, ending however in failure. Trying to overcome the enormous calculation requirements of his model, Richardson proposed as a solution the "forecast-factory": a vast stadium filled with 64.000 people, each one with a mechanical calculator and performing a part of the whole flow computation under the direction of a leader in the centre. This kind of idea could be considered as a very rudimentary CFD calculation.

Thom in 1933 presented the earliest numerical solution for the flow past a cylinder [92], while Kawaguti in 1953 achieved similar results for flow around a cylinder by using a mechanical desk calculator, working for 18 months 20 hours per week.

A big contribution in the development of CFD numerical methods was done during the 1960s by the theoretical division of NASA at Los Alamos: Particle-In-Cell (PIC), Marker-and-Cell (MAC), Vorticity-Stream function, Arbitrary Lagrangian-Eulerian (ALE) methods and the ubiquitous k-ε turbulence model are still nowadays in use. Further steps ahead were made in the 1970s by Spalding's working group at the Imperial College of London, who went on developing the Upwind differencing scheme, as well as "Eddy break-up" and "presumed pdf" combustion models.

A milestone in the development of CFD codes was then the publication in 1980 of Patankar's "Numerical Heat Transfer and Fluid Flow", still a key book in the spreading of computational techniques. The first commercial codes started also to be purchased in the early 1980s, parallel to the diffusion of in-house and universities solvers. Nowadays CFD is part of the computer-aided engineering (CAE) spectrum of tools, which are constantly used in industry and research institutions.

2.1.2. Conservation equations of fluid flow

The governing laws of a flowing fluid are directly derived from physical conservation principles [93], which for a chosen system could be summarized by the following statements:

- Mass is conserved (continuity equation).

- Momentum rate of change is equal to the sum of acting forces (Newton's second law).

- Energy rate of change is equal to the sum of the rate of heat addition and the rate of work done on the system (first law of thermodynamics).

In the derivation of the governing equations, a fluid element is collected in a control volume, which represents the smallest possible entity of the system. The fluid is treated as a continuum, so that the conservation equations are supposed to exactly describe its thermodynamical evolution. According to this hypothesis macroscopic properties are not affected from the single molecules. The presented conservation equations are valid for a Newtonian fluid, which means a fluid where the viscous stresses are proportional to the rates of deformation.

The mass conservation for the fluid element states that rate of increase of mass inside the control volume equals the flow into the element. The continuity equation, representing the unsteady 3D mass conservation principle, could be formulated by

$$\frac{\partial \rho}{\partial t} + \frac{\partial (\rho u_x)}{\partial x} + \frac{\partial (\rho u_y)}{\partial y} + \frac{\partial (\rho u_z)}{\partial z} = 0 \tag{2.1.1}$$

or compactly

$$\frac{\partial \rho}{\partial t} + div(\rho \, \vec{u}) = 0 \tag{2.1.2}$$

with $\vec{u}$ representing the velocity vector (u_x, u_y, u_z). According to the second law of Newton, the momentum rates of change per unit volume in the three principal directions are defined in equations (2.1.3-2.1.5), where the terms S_{Mi} represent eventual sources in the three main directions.

$$\frac{\partial (\rho u_x)}{\partial t} + div(\rho u_x \vec{u}) = -\frac{\partial p}{\partial x} + div(\mu \, grad u_x) + S_{Mx} \tag{2.1.3}$$

$$\frac{\partial (\rho u_y)}{\partial t} + div(\rho u_y \vec{u}) = -\frac{\partial p}{\partial y} + div(\mu \, grad u_y) + S_{My} \tag{2.1.4}$$

$$\frac{\partial (\rho u_z)}{\partial t} + div(\rho u_z \vec{u}) = -\frac{\partial p}{\partial z} + div(\mu \, grad u_z) + S_{Mz} \tag{2.1.5}$$

Using the Newtonian model for viscous stresses for the internal energy equation it is possible to obtain

$$\frac{\partial (\rho e)}{\partial t} + div(\rho e \vec{u}) = -p \, div \, \vec{u} + div(k \, grad T) + \Phi + S_e \tag{2.1.6}$$

The term S_e represents an eventual energy source, while Φ is the dissipation function, which embodies all the effects due to viscous stresses and therefore represents a source of internal energy due to deformation work on the fluid particle.

$$\Phi = \mu \left\{ 2\left[\left(\frac{\partial u_x}{\partial x}\right)^2 + \left(\frac{\partial u_y}{\partial y}\right)^2 + \left(\frac{\partial u_z}{\partial z}\right)^2 \right] + \left(\frac{\partial u_x}{\partial y} + \frac{\partial u_y}{\partial x}\right)^2 \right. \\ \left. + \left(\frac{\partial u_x}{\partial z} + \frac{\partial u_z}{\partial x}\right)^2 + \left(\frac{\partial u_y}{\partial z} + \frac{\partial u_z}{\partial y}\right)^2 \right\} + \lambda \left(div \, \vec{u} \right) \tag{2.1.7}$$

Equations (2.1.3-2.1.5) are known as Navier-Stokes equations and describe the motion of fluid elements both for laminar and turbulent flows. The assumption of substance continuity allows a deterministic solution of the governing equations, which are non-linear second-order partial differential equations.
In the case of internal combustion engines, turbulence phenomena acquire a magnitude that makes it impossible to solve numerically the Navier-Stokes equation within realistic time

frames. For this reason the closure of fluid motion needs to be separately resolved through the introduction of RANS (Reynolds Averaged Navier Stokes) approximations and turbulence modeling, as described in the following section.

2.1.3. Turbulence modeling

It is difficult to make a strict definition of turbulence, as many flows present turbulent behavior. Thus, some properties could be addressed to describe the phenomenon [60]:

- Turbulence produces unsteady three-dimensional velocity fluctuations, whose maximum variation is usually in the order of 10-20 percent of the mean velocity. The turbulent fluctuations cannot mathematically be described as random variables, even though a time history of turbulent flows appears stochastic.
- A gradient in the mean flow velocity profile, called mean shear, keeps the turbulence self-sustaining.
- Turbulence diffuses in the non-turbulent flow.
- Turbulence is dissipative, as the kinetic energy in the small eddies is transferred to internal energy of the surrounding fluid.

The prediction of turbulent flows could be done with different approaches [9], each one with increasing complexity and consistency level. The main solution methods could be then classified in six categories.

- **Direct Numerical Simulation (DNS)**
The most accurate and conceptually simplest approach in turbulence simulation is to solve the Navier-Stokes equations without approximations other than numerical discretizations. In order to capture all the significant structures of turbulence, the computational domain must be at least as large as the largest turbulent eddy.

- **Large Eddy Simulation (LES)**
The largest scale motions of the flow are solved, while only the small scales are modeled. The basic idea is that the large eddies are generally much more energetic than the small ones, consequently they are the most effective transporters of the conserved properties. DNS is usually the preferred method whenever feasible, while LES is adopted in the case of too high Reynolds number or too complex geometries.

- **Two-point closure**
The velocity components at two different points are mathematically correlated or, more often, the Fourier transform of these equations is used. These methods are rarely used, except for homogeneous turbulence.

- **Reynolds averaged Navier-Stokes (RANS)**
The equations of motion are averaged over time and over a set of imagined flows in which all controllable factors are kept fix. This approach is called one-point closure and leads to a set of partial differential equations known as the Reynolds averaged Navier-Stokes equations. The equation set is not closed, therefore the method requires the introduction of approximations in terms of turbulence models. The problems addressing the numerical solution of RANS are discussed later in this chapter.

- **Integral equations**

This solution approach involves the integration of equations of motion over one or more coordinates. The method usually reduces the problem to one or more ordinary differential equations that could be easily solved.

- **Correlations**

Relationships between thermo-dynamical flow properties are introduced. For example the friction factor is written as a function of the Reynolds number or the Nusselt number of heat transfer is related to Reynolds and Prandtl numbers. This method does not require the use of a computer and is limited to simple types of flows.

For engineering purposes, the standard approach in accounting turbulence effects is the Reynolds Averaged Navier-Stokes, mostly for the acceptable costs in terms of computational efforts. Therefore, an overview of RANS method will be given ([27], [87], [93]).

Fluctuations of the mean flow are produced by irregularities of the instantaneous flow, which could be consequently decomposed in a mean and a fluctuating component. The most frequent decomposition is that of Reynolds:

$$\hat{\phi} = \Phi + \phi' \qquad (2.1.8)$$

The instantaneous component $\hat{\phi}$, function of instantaneous position and time, is divided into the mean component Φ and the fluctuating component ϕ', defined so that its mean value is equal to zero. In the case of stationary flow, or flow slowly varying in time, the mean flow values are of interest rather than the temporal histories. The mean component could be then expressed as a function of position through a time averaging integration.

$$\Phi(x_i) = \lim_{\tau \to \infty} \frac{1}{\tau} \int_0^\tau \hat{\phi}(x_i, t) dt \qquad (2.1.9)$$

For unsteady flows, an ensemble average over n_e samples has to be preferred.

$$\Phi(x_i, t) = \lim_{\tau \to \infty} \frac{1}{n_e} \sum_{i=1}^{n_e} \hat{\phi}(x_i, t) \qquad (2.1.10)$$

Equation (2.1.8) could be then rewritten as

$$\hat{\phi}(x_i, t) = \Phi(x_i) + \phi(x_i, t) \qquad (2.1.11)$$

Instantaneous values for velocity, enthalpy and pressure could be also defined as

$$\hat{u}_i = U_i + u_i' \qquad \hat{h} = H + h' \qquad \hat{p} = P + p' \qquad (2.1.12)$$

The new variables u_i, h and p need to be modeled in order to close the equation system and account for turbulent effects on the flow. There are different approaches to resolve the so-called turbulence closure problem:

1. Algebraic models
2. One-equation models
3. Two-equations models
4. Reynolds stress models

The first three models are based on the assumption of Boussinessq, stating that the Reynold stress tensor τ_{ij}, used in the Navier-Stokes equations, is related to velocity gradients multiplied by the turbulent viscosity μ_t.

$$\tau_{ij} = -\rho \overline{u_i u_j} = \mu_t \left(\frac{\partial U_i}{\partial x_j} + \frac{\partial U_j}{\partial x_i} \right) \tag{2.1.13}$$

Direct analogies to the equations of molecular and turbulent flux of momentum, heat and species allow modifying the thermodynamical properties of flow eddies in order to account for turbulence. Effective values for eddy species i diffusivity $D^{(i)}_{eff}$, temperature diffusivity α_{eff} and dynamic viscosity μ_{eff} have to be added by the turbulent summands.

$$D^{(i)}_{eff} = D^{(i)} + D^{(i)}_t \qquad \alpha_{eff} = \alpha + \alpha_t \qquad \mu_{eff} = \mu + \mu_t \tag{2.1.14}$$

According to the eddy viscosity approach, conservation equations for transport are solved as for laminar flows, except that molecular exchange coefficients are replaced by effective values related to velocities. Nevertheless, this assumption introduces nonlinear terms in the solving equations. The closure problem is then reduced to the estimation of eddy viscosity and diffusion coefficients. Based on dimensional analysis, turbulent viscosity could be formulated as the product of a characteristic turbulent length scale L_t and velocity scale U_t.

$$\frac{\mu_t}{\rho} \propto L_t U_t \tag{2.1.15}$$

At a first approach, the scales L_t and U_t could be respectively estimated from flow geometry and mean flow properties. Still, as turbulence is a local phenomenon and evolves in time, it is better to bind eddy viscosity to turbulence parameters. Prandtl and Kolmogorov correlated the velocity scale to the turbulent kinetic energy κ, whose average intensity $\kappa^{1/2}$ is given in equation (2.1.16).

$$U_t \sim \kappa^{1/2} = \sqrt{\frac{1}{2} \left(\overline{u}_x^2 + \overline{u}_y^2 + \overline{u}_z^2 \right)} \tag{2.1.16}$$

Also turbulent length scale has then to be modeled, according to algebraic or empiric geometrical assumptions.
A further step ahead is to adopt differential eddy viscosity models, which are classified depending on the number of resolved differential equations. In one-equation models a differential equation for κ is computed, whereas the turbulent length scale is algebraically modeled, mostly through geometrical parameters. The two-equation models introduce a further transport equation for L_t, whose solution is obtained either directly or in combination with the turbulent kinetic energy. One-equation models are for sure easier and computationally faster than two-equations ones. Nonetheless, algebraic estimations of length

scale are inadequate for complex internal flows, where also turbulence and flow history play a primary role. The most common two-equations model is the so-called κ–ε model, which provides in most situations reasonable predictions of the mean flow. The basic idea is to solve transport equations for turbulent kinetic energy κ and dissipation ε. The κ-equation is derived from the time averaged Navier-Stokes equations and includes terms for convection, production, turbulent diffusion and dissipation.

$$\rho \frac{\partial \kappa}{\partial t} + \rho U_j \frac{\partial \kappa}{\partial x_j} = P + G - \varepsilon + \frac{\partial}{\partial x_j} \left(\mu + \frac{\mu_t}{\sigma_\kappa} \frac{\partial \kappa}{\partial x_j} \right) \tag{2.1.17}$$

Respectively, the terms P and G represent the production of turbulent kinetic energy by mean flow deformation and the production or destruction of turbulent kinetic energy by body forces. The ε-equation could not be directly extracted from the governing laws, whereas from assumptions of analogy with the transport equation for turbulent kinetic energy.

$$\rho \frac{D\varepsilon}{Dt} = \left(C_{\varepsilon 1} P + C_{\varepsilon 3} G + C_{\varepsilon 4} \kappa \frac{\partial U_k}{\partial x_k} - C_{\varepsilon 2} \varepsilon \right) \frac{\varepsilon}{\kappa} + \frac{\partial}{\partial x_j} \left(\frac{\mu_t}{\sigma_\varepsilon} \frac{\partial \varepsilon}{\partial x_j} \right) \tag{2.1.18}$$

This similarity hypothesis directly leads to the introduction of modeling constants, which are mostly derived from empirical or experimental achievements and gain the standard values presented in table 2.1.

C_μ	$C_{\varepsilon 1}$	$C_{\varepsilon 2}$	$C_{\varepsilon 3}$	$C_{\varepsilon 4}$	σ_κ	σ_ε	σ_ρ
0.09	1.44	1.92	0.8	0.33	1	1.3	0.9

Table 2.1: Constants in the κ-ε model

In the Reynolds Stress Model (RSM) each component of the Reynolds tensor $\overline{u_i u_j}$ is transported, together with an equation for the turbulent length scale. The model could provide better results as it accounts for the anisotropy of the turbulent flow. Nevertheless, the computational demand is too high for most of the operative applications.

The κ-ε model represents the standard model for all simulations presented in this thesis, as for engineering purposes actual computational power does not allow the embracing of more detailed approaches like LES or DNS.

2.1.4. Numerical Solution Methods

Flows and related phenomena could be described by partial differential or integro-differential equations, which can be solved analytically only in special cases. To obtain an approximate solution discretization methods can be used. Differential equations are approximated by systems of algebraic equations, which can be numerically solved on a computer. The approximations are applied at discrete locations in space and time, where the conservation laws are computed.

The most important discretization methods are finite difference (FD), finite volume (FV) and finite element (FE) methods.

- **Finite Difference (FD) method**

The solution domain is divided into a grid and each nodal point is associated to a discrete field value. Differential equations are then approximated by replacing the partial derivates with functions related to the grid points variables. One algebraic equation per node has then to be solved. According to the chosen approximation, the variable value at the considered node and at a certain number of neighbor points is unknown. An overview of the most common approaches for the solution of a FD problem can be seen in [54].

In principle the FD method can be adapted to any grid type, even if to maintain an easy and effective formulation, it is usually applied to structured grids. Nevertheless, high order differential schemes are simpler to obtain on regular grids. The limitation of the method is that conservation is not assured unless particular care is taken. Moreover, the restriction to simple geometries does not allow the resolution of complex flows.

- **Finite Volume (FV) method**

The starting point of the FV method is the integral form of the conservation equations. The domain is then divided into a discrete number of control volumes (CVs) on which the conservation equations are applied. The variable values are defined at nodal points corresponding to the centroids of each CV. In order to calculate surface integrals, the variables at CV surface are obtained through suitable interpolations of CV-center values. The final result is an algebraic equation for each control volume depending also on neighbor nodal values.

Basically, the advantages of the FV approach are that it is conservative by construction and that it can be used with any type of grid and complex geometries. The common CFD industrial applications are therefore mostly based on FV methods. A disadvantage of FV approaches is that schemes of order higher than second are more difficult to be developed than with FD methods.

- **Finite Element (FE) method**

The domain is divided into a set of discrete volumes or finite elements, which are usually unstructured. The computational meshes are typically made of triangles or quadrilaterals in 2D domains and tetrahedra or hexahedra in 3D spaces. Before the integration over the entire domain, the solution equations are multiplied by a weighting function. In the simplest case the weight function is approximated within each element by a linear shape, which can be constructed starting from its values at the elements corners. Afterwards, this approximation is introduced into the weighted integral of the conservation law. The solving equations are obtained by imposing the derivative of the integral at each nodal value to be zero. The result is a set of non-linear algebraic equations, whose solution corresponds to the best fitting function with minimum residual.

The main advantage of the FE methods is the easiness to deal with arbitrary geometries, even if the matrices of the linearized equations are not as well structured as in regular grids. This aspect, common to any method using unstructured grids, leads to difficulties in the definition of an efficient solution method. The application of FE methods, usually implemented for structural mechanics problems, is nevertheless of little interest in the solution of the Navier-Stokes equations.

2.2. Multiphase Flow Theory

A mixture of different constituents composes almost every physical material. The conservation equations discussed in section 2.1.2 are valid for homogeneous materials, even if

they could be extended to so–called classical mixtures or solutions, where the singular components appear unphysically distinct and the mixing resides at a molecular level [20]. Examples of such materials are air, composed ofy nitrogen, oxygen and other species in small amounts, water or liquid fuels.

Nevertheless, the assumption of intermiscibility is not appropriate for all physical situations. Suspensions of particles in water or granular propellants are some examples of identifiable solid structures surrounded by one or more continuous media. As long as no chemical reaction happens, each constituent maintains its integrity. These materials are called multicomponent mixtures. The solution of the problem could be described with a Lagrangian approach: the evolution of position and deformation of each particle is solved, together with the complete history of the transporting flow field. Averaging processes for the parcels could then be used to reduce the computational effort. There are also situations where the multicomponent mixture is made by immiscible and continuous materials. In these cases the interfaces between fluids constantly vary in time and place. Some examples are all the liquid-gas and liquid-liquid interaction phenomena. These phenomena seem to be better defined by a Eulerian approach, where the evolution of interfaces is evaluated in each singular control volume.

2.2.1. General equations

Conceptually, the multiphase governing laws could be directly derived from the Navier-Stokes equations for single component flow, with the addiction of a term for the volume fraction of phase α_k.
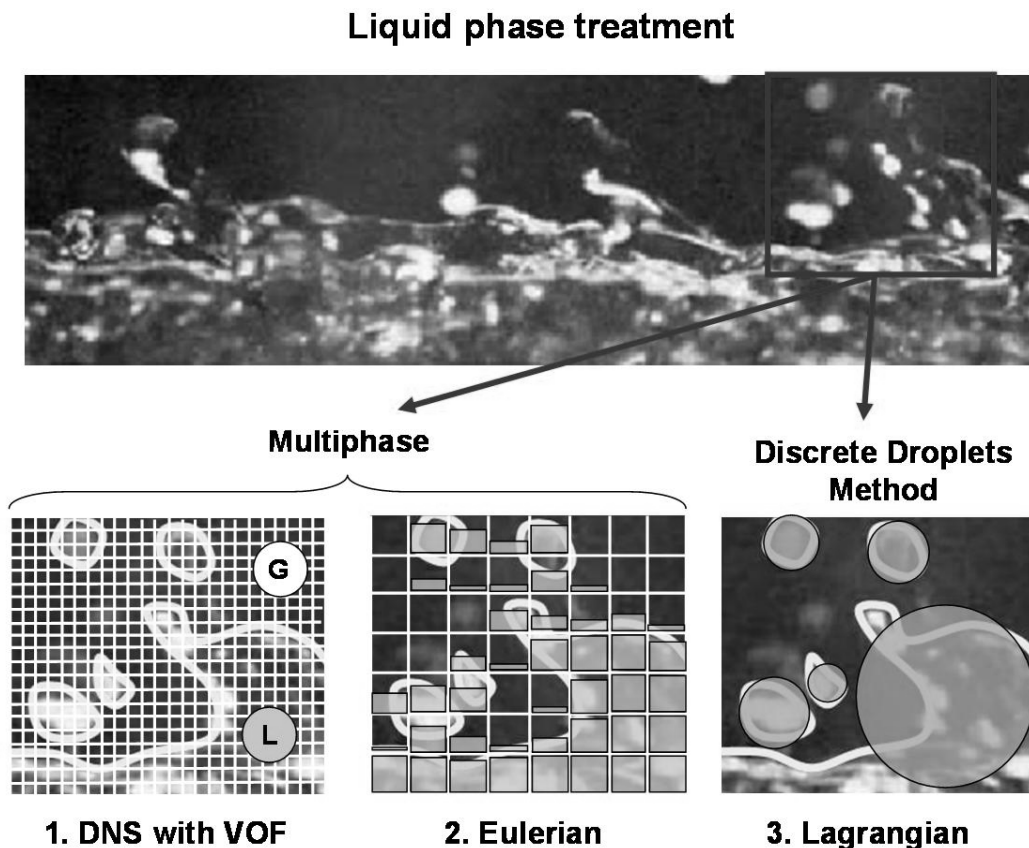
Figure 2.2: Different approaches to treat the liquid continuous phase.

The mathematical foundation of the multiphase approach is treated in the works of Drew and Passman [20], Ferziger and Peric [27] or Lahey and Drew [46]. The mass conservation equation for the single phase (2.1.2) could be exact formulated [3] in multiphase coordinates for the phase k as

$$\frac{\partial \alpha_k \rho}{\partial t} + \nabla \cdot (\alpha_k \rho \, \vec{u}) = \rho(\vec{u} - \vec{u}_{\text{int}}) \cdot \nabla \alpha_k \qquad (2.2.1)$$

with the term $\vec{u}_i$ representing the velocity of the interface between the phases. Momentum conservation assumes then the form

$$\frac{\partial \alpha_k \rho \, \vec{v}}{\partial t} + \nabla \cdot (\alpha_k \rho \, \vec{u} \, \vec{u}) = \nabla \cdot \alpha_k (-pI + \tau) + \alpha_k \rho \, \vec{g}$$
$$-(-pI + \tau) \cdot \nabla \alpha_k + \rho \, \vec{u}(\vec{u} - \vec{u}_{\text{int}}) \cdot \nabla \alpha_k \qquad (2.2.2)$$

with I as the unity tensor and τ the shear stress tensor. The equations (2.2.1) and (2.2.2) represent the exact solution of the conservation equations for each single phase k. A typical multiphase flow is for example a liquid jet in air, as shown in figure 2.2. In order to compute the multicomponent stream, discretization approaches have to be introduced.

2.2.2. Solution methods

The most detailed solution method of the multiphase flow is the VOF (Volume of Fluid) approach [38], which could be principally classified as a DNS (Direct Numeric Simulation) surface tracking technique. The basic idea is to locally resolve the interfaces between the phases through the adoption of very fine grids, as shown in figure 2.3. Starting from the exact solution of the conservation equations, the mass conservation for a N-components mixture is rewritten introducing a source term Γ_{kl} between the phases k and l, which accounts for the mass exchanges between the phases.

$$\frac{\partial \alpha_k \rho_k}{\partial t} + \nabla \cdot (\alpha_k \rho_k \vec{u}_k) = \sum_{l=1, l \neq k}^{N} \Gamma_{kl} \qquad (2.2.3)$$

Momentum conservation is then resolved for the whole mass contained in a cell, assuming the mixture components flowing at the same velocity and introducing an additional source term for the surface tension acting along the interface between the fluids. The continuum surface force (CSF) model by Brackbill [15] proposes for example an interfacial force depending on the surface tension coefficient σ and on the local surface curvature $\vec{c}$. Cell density ρ is obtained with an averaging procedure on the single phases values.

$$\rho = \sum_{k=1}^{N} \alpha_k \rho_k \qquad (2.2.4)$$

In some VOF solvers the interface between the phases is reconstructed and tracked by the solution of an additional scalar transport equation [97]. The high computational requirements make the VOF methods unsuitable for standard engineering applications.

In order to save computing resources, the numerical simulation needs to be performed on coarser grids and the Eulerian approach has to be introduced. In this case the definition of distinct interfaces between the phases is no longer possible, as shown in the second grid of Figure 2.2. The mass conservation is still formulated as in (2.2.3), while the momentum equations are singularly resolved for each phase k with the introduction of source terms $\vec{M}_{kl}$.

$$\frac{\partial \alpha_k \rho\, \vec{u}_k}{\partial t} + \nabla \cdot (\alpha_k \rho_k \vec{u}_k \vec{u}_k) = -\alpha_k \nabla p + \nabla \cdot \alpha_k (\tau_k - T_k)$$
$$+\alpha_k \rho_k \vec{g} + \sum_{l=1,l\neq k}^{N} \vec{M}_{kl} + \vec{u}_k \sum_{l=1,l\neq k}^{N} \Gamma_{kl} \qquad (2.2.5)$$

The interaction between the phases needs to be modeled through the definition of suitable interfaces. More details will be given in the next chapter according to the resolution of multiphase sprays.

2.2.3. Applications

The adoption of the multiphase approach in simulation of physical problems was developing very fast in the last years. Excluding the pure aerodynamics applications, many phenomena are built due to the interaction between different materials and states of aggregation: the assumption of mean properties for different interacting fluids appears therefore as a strong limitation.
In the simulation of internal combustion engines the multiphase applications are quickly broadening, thanks to the faster computational power.
The Multiphase solver applications treated in the present work are the internal nozzle flow and the Eulerian Spray model. For the first one, three phases, liquid, vapor and air, will interact during the simulation of the injection process. The second one needs a phase for gas and a chosen amount for droplets. Both cases will be analyzed in detail. It is important to underline, that each simulation uses the same solver, but different sub-models to treat the interaction between the phases.
Other engine applications can be found in recent development for combustion modeling: a first step is to consider burned and unburned gases as two distinct entities; future development and detailed chemistry models could also lead to simulate different reactive species as interacting phases.

3. Spray simulation

3.1. Introduction

As introduced in the previous chapter, the spray formation process is a typical 2-phases phenomenon. For this reason the co-existence of interacting physical phases needs to be considered and modeled. The easiest approach, at least in terms of modeling complexity, is to adopt a Direct Numerical Simulation (DNS). The computational grid has to be fine enough to resolve all length scales of the problem, but no assumptions in terms of parcels or turbulence need to be made. On the other hand, the computational costs would be incompatible with today's requirements. For this reason PDF (Probability Density Function) assumptions have to be made and a spray equation is introduced, as discussed in paragraph 3.2.

The practical solution of the spray equation is obtained by collecting droplets with similar properties in diameter and velocity into statistical entities: equations of motion are solved for these parcels with the same thermodynamics conditions. The solution of spray transport could be subsequently done with two different methods, as presented in paragraph 3.3. The first one is the Lagrangian approach: the fundamental idea is to track the fluid particles in space and integrate the conservation equation over time. Meanwhile, the gas flow field surrounding the spray drops is calculated in Eulerian coordinates and interacts with them through exchange of source terms due to drag and evaporation. This method, called Discrete Droplet Model (DDM), is therefore an Eulerian/Lagrangian approach and it constitutes the standard scheme to describe the spray formation.

The second method consists of fixing for each phase defined control volumes, where the conservation equations are solved: this leads to a pure Eulerian/Eulerian approach. In this case a multiphase solver is needed for the stochastic spray evolution. The main idea is to collect droplets with the same thermodynamic properties and diameters into classes, which are then treated as interacting phases. No parcel is followed in its motion and classes volume fraction values identify the PDF droplets distribution inside a single computational cell. This kind of approach could provide the most advantages in the dense spray region near the injector, where the turbulent interaction between droplets is a dominant effect.

Advantages and limits of both methods will be also analyzed, together with the definition of the most important sub-models and main equations for the liquid/droplets phase.

Paragraph 3.4 will give an overview of the Lagrangian Discrete Droplets Method (DDM) and its application on spray simulation.

Paragraph 3.5 will analyze two different techniques to treat the Eulerian spray modeling, both of them directly adopted in the current work. The main focus will be to give an overview of the different approaches to treat droplets phases and exchange processes.

3.2. Statistical closure: DNS vs. PDF

The interaction between gas and liquid could be treated at different complexity levels, starting from detailed DNS with Volume Of Fluid (VOF) interface reconstruction [38], up to PDF assumptions on ligaments and droplets [68]. DNS analysis could reach a high level of accuracy, as they could resolve the microscopic structures of droplets and ligaments according to the achieved mesh definition. Furthermore, no assumptions for turbulence modeling are needed. On the other hand, DNS simulations are still too time-consuming for industrial application and evaporation treatment is still under development, for example with the non-commercial VOF code Free Surface 3D (FS3D) [70].

As a consequence of the mentioned reasons, the most used approach to simulate a spray is based on the introduction of PDF assumptions: the single spray entities are no more directly resolved and a spray equation is introduced for the transport of droplets ensembles [95]. The distribution function f_d represents the probability density of spray droplets, according to a chosen number of independent variables, for example droplets coordinates $\vec{x}_d$, velocity $\vec{u}_d$, radius r_d, temperature T_d (assumed uniform within the drop) and time t. As shown in Eq. (3.2.1), the integration of f_d provides the probable number N of droplets per unit volume at position $\vec{x}_d$ and time t, with the above-mentioned variables in the intervals $(\vec{u}_d, \vec{u}_d + d\vec{u}_d)$, $(r_d, r_d + dr_d)$ and $(T_d, T_d + dT_d)$.

$$f_d(\vec{x}_d, \vec{u}_d, r_d, T_d, t) \ d\vec{u}_d \ dr_d dT_d = N \tag{3.2.1}$$

The time evolution of f_d is obtained by solving a form of the spray equation (3.2.1).

$$\frac{\partial f_d}{\partial t} + \nabla_{\vec{x}}(f_d \ \vec{u}_d) + \nabla_{\vec{u}}(f_d \ \vec{u}_d) + \frac{\partial}{\partial r_d}(f_d \ \dot{r}_d) + \frac{\partial}{\partial T_d}(f_d \ \dot{T}_d) = \dot{f}_d \tag{3.2.2}$$

The quantities $\dot{\vec{u}}_d$, $\dot{r}_d$ and $\dot{T}_d$ are the time rates of changes for a single droplet according to its velocity, radius and temperature. The term $\dot{f}_d$ represents all the sources due to droplets collisions and breakup, which need to be provided by spray models.

Solving the spray equation according to the rates of change for mass, momentum and energy for all droplets at position $\vec{x}_d$ and time t, it is possible to obtain the exchange functions $\dot{\rho}^S$, $\vec{F}^S$, $\dot{q}^S$ and $\dot{W}^S$, as shown in Equations (3.2.3-6). The term $(\vec{u}_d - \vec{u}_g)$ represents the relative velocity between droplet and gas, $\vec{u}'$ is the gas-phase turbulence velocity, e_d and c_{pd} are the internal energy and specific heat of liquid drops.

$$\dot{\rho}^S = -\int f_d \ \rho_d 4\pi r_d{}^2 \dot{r}_d \ d\vec{u}_d \ dr_d \ dT_d \tag{3.2.3}$$

$$\vec{F}^S = -\int f_d \ \rho_d (4/3\pi r_d{}^3 \dot{\vec{u}}_d + 4\pi r_d{}^2 \dot{r}_d \vec{u}_d) \ d\vec{u}_d \ dr_d \ dT_d \tag{3.2.4}$$

$$\dot{q}^S = -\int f_d \ \rho_d \{4\pi r_d{}^2 \dot{r}_d [e_d + 1/2(\vec{u}_d - \vec{u}_g)^2] +$$
$$4/3\pi r_d{}^3 [c_{pd}\dot{T}_d + \dot{\vec{u}}_d(\vec{u}_d - \vec{u}_g - \vec{u}')]\} \ d\vec{u}_d \ dr_d \ dT_d \tag{3.2.5}$$

$$\dot{W}^S = -\int f_d \ \rho_d \, 4/3\pi r_d{}^3 \dot{\vec{u}}_d \vec{u}' \ d\vec{u}_d \ dr_d \ dT_d \qquad (3.2.6)$$

The above described exchange functions have physical meaning: $\dot{\rho}^S$ is the rate of mass evaporation from the droplets, $\vec{F}^S$ the force transmitted from drops to gas through drag effects, $\dot{q}^S$ is the energy transmitted to the gas by evaporation, by work due to turbulent fluctuations and by heat transfer, $\dot{W}^S$ is the rate of work done by turbulent eddies in dispersing the droplets. The exchange functions describe the interactions between spray droplets and gas phase, so that the solution of the spray equation directly expresses the evolution of drops in time and space.

3.3.   Different approaches for solving PDF

The droplets evolution in time and space is resolved by the mathematical closure of equation (3.2.2). Some researchers [33] adopted an Eulerian finite difference method to directly integrate the spray equation. Nevertheless, this method appeared to be impractical since each independent variable has to be discretized on a grid, and with the 9 independent variables of Eq. (3.2.1) the required computer storage becomes excessive: e.g. with a coarse mesh of only 10 mesh points in each dimension, 10^9 grid points would be necessary.

A practical solution technique is to use a stochastic particle model. The basic idea is to group the physical droplets into representative parcels, each one embodying a number of identical drops with the same values of velocity, radius, temperature and turbulent parameters. Afterwards, the evolution of droplets ensembles needs to be solved. The most common approaches are the so-called Lagrangian and Eulerian approaches.

The Lagrangian Monte Carlo method, also called Discrete Droplets Method (DDM), was proposed by Dukowitz [22] and first implemented in the CFD code KIVA [6]. The paths of statistic parcels of drops are followed in physical, velocity, radius and temperature space. Mathematically, Equation (3.2.2) is a hyperbolic equation and the paths represent characteristics in the solution space. The particles are directly moved to new locations in physical space after each time interval dt, following the force $\vec{F}$ obtained with Eq. (3.3.1).

$$\frac{d\vec{u}_d}{dt} = \vec{F} \qquad (3.3.1)$$

For a vaporizing spray, the change in drops size r_d is related to the time rate of change $\dot{r}_d$ of parcels radius, which need to be provided by a chosen evaporation model.

$$\frac{dr_d}{dt} = \dot{r}_d \qquad (3.3.2)$$

Droplets size is also influenced by break-up, coalescence and collision. These discrete phenomena lead also to a change in drops number in a particular size class and to the appearance or disappearance of parcels from the simulation. The sources $\dot{f}_d$ will be further described in paragraph 3.3.5.

$$\frac{df_d}{dt} = \dot{f}_d \tag{3.3.3}$$

The collection of all parcels in the computational domain represents the spray drop number distribution. Statistics are improved by increasing the parcels number, since only discrete values of independent variables are represented in the computation.

An alternative Lagrangian modeling approach is called PSI Cell (Particle-Source-in-Cell), proposed by Crowe [19] and most suited for steady-state spray computations. The solution procedure consists of solving the gas flow field assuming at first the presence of no parcels. Afterwards particle trajectories are computed, together with mass and temperature history on each trajectory. Mass, momentum and energy source terms for the gas are then calculated in each cell traversed by the particles and gas flow field is recomputed. New trajectories for the drops are then solved, again the source terms evaluated, and the process continues until convergence occurs. As the PSI Cell method is inappropriate for simulating spray dispersion effects in turbulent environments, itis adopted only in applications with steady flows.

The basic idea of the Eulerian Spray [12] consists of subdividing the spray droplets into a selected number of phases, each one with the same physical and thermodynamical properties. The surrounding gas is represented by an additional phase, which interacts with the statistical parcels. Each phase is represented by a volume fraction α_k of the containing cell and the droplets classes are classified by diameter.

As mentioned in the previous chapter, the core point of multiphase modeling is the definition of the exchange interface between the phases. Many approaches could be used to define this interface and eventually reconstruct it. In the current work the basic idea is the assumption of spherical droplets: with this hypothesis the volume fraction α_k of each droplet phase k could be directly linked to the parcel diameter d_k. As shown in Eq. (3.3.4), the value N_k represents the droplets number density in phase k.

$$N_k = \frac{6 \, \alpha_k}{\pi \, d_k^{\,3}} \tag{3.3.4}$$

Modification of the diameter values due to atomization or evaporation could be therefore directly linked to number density or volume fraction.

As for the Lagrangian approach, the exchange terms of Eq. (3.2.3-3.2.6) need to be transferred to the droplet phases. In this case the solution of the spray equation is performed in Eulerian coordinates: the multiphase solver recursively calculates each droplet phase on each cell of the computational domain. The liquid-liquid and liquid-gas interaction needs nonetheless to be modeled through the introduction of appropriate source terms, as it will be presented in paragraph 3.3.4.

An essential difference between Eulerian and Lagrangian approaches is also on the description of discontinuous processes as atomization. The first method could describe only continuous processes, while DDM parcels could be easily split into child droplets with smaller diameter. For this reason the modelization of break-up processes represents one of the most challenging problems for the Eulerian approach, as it affects directly the drops diameter and therefore phases definition and boundaries.

In the following paragraph the validity fields of Lagrangian and Eulerian methods will be analyzed, evaluating the reasons for the adoption of both in the current work.

3.3.1. Motivation

Spray dynamics and evaporation are strongly affected from the interaction with gas phase and from the interaction of droplets. In the study of fluid injection it is possible to identify different spray regimes [56]. The region where droplets occupy a consistent fraction of the mixture volume is located near the nozzle outlet and here the spray is classified as "thick" or "dense". Moving away from the injection location spray usually diverges according to turbulent dispersion phenomena and droplets size decreases under the effects of evaporation and atomization. In the "thin" and "very thin" regimes the particles are widely spaced and isolated drops correlations could be adopted to calculate the exchanges between parcels and gas: this is the region where the Lagrangian DDM model is most suitable to describe the spray dynamics. However, near the nozzle orifice the drops turbulent mixing and the strong particles interactions are difficult to be represented discretely, even with complicated collision and coalescence models [58].

A practical way to characterize the beginning of the "thick" spray regime could be taken according to the definition of gas-phase void fraction θ [56].

$$\theta = 1 - \int_{r_d}^{r_d + dr_d} \int_{\vec{u}_d}^{\vec{u}_d + d\vec{u}_d} \int_{T_d}^{T_d + dT_d} \frac{4}{3} \pi \, r_d^{3} f_d \ dr_d d\vec{u}_d \ dT_d \qquad (3.3.5)$$

Values of approximately $\theta < 0.9$ define the start of the regimes, where the spray itself may be hardly described by the DDM approach.
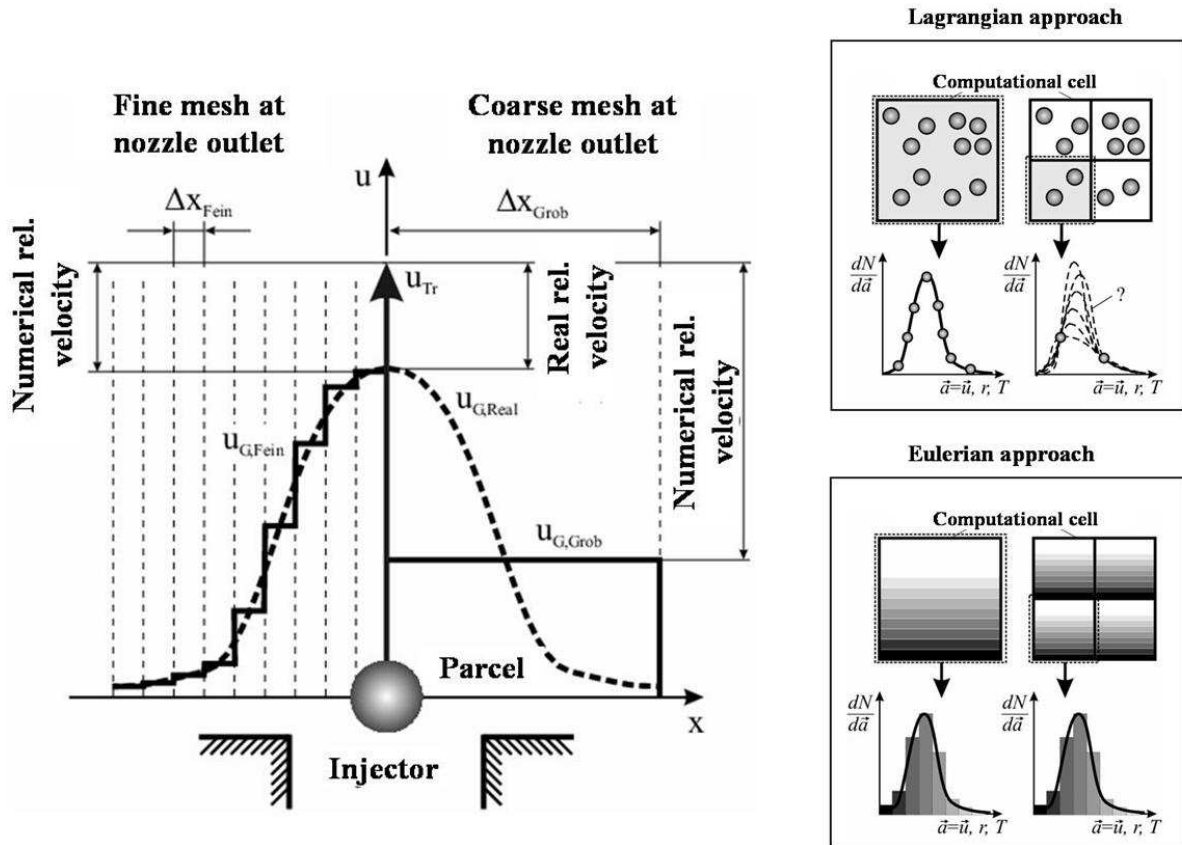
Figure 3.1: Spray formation: spatial resolution versus statistical convergence [36].

Another reason for the adoption of the Eulerian approach is the reliability of exchange processes in the nozzle orifice region. A typical high-pressure injection process usually leads to extremely high fuel mass flows, therefore large velocity gradients just outside the nozzle orifice. Thermodynamics length scales are in the order of the nozzle diameter and if the mesh does not resolve the injector hole, the relative velocity between droplets and gas phase is overestimated (see Figure 3.1). This leads to an incorrect calculation of exchange processes; moreover, the velocity profile of the gas phase could not be captured: turbulence production and turbulent viscosity are therefore under predicted.

In the standard Lagrangian stochastic approach the PDF expressing droplets statistics is transported by a number of parcels. To represent the PDF correctly the number of parcels per cell has to be sufficiently high. The contradiction of the Lagrangian approach is that increasing the space resolution to resolve the gas dynamics, the number of parcels per cell consequently diminishes together with the statistical convergence, as proven also in many investigations [34]. This is also a reason for the adoption of the Eulerian approach in the region near the nozzle hole, as the number of droplet classes is independent from cell dimension. Grid resolution could be hence improved without losing the stochastic models foundation.

The next paragraphs will show the formulation of conservation equations for the Lagrangian and the Eulerian approach, followed by the definition of the spray sub models used in the current work.

3.3.2. Transport with DDM

For each computational spray parcel a set of mass, momentum and energy conservation equations need to be solved. The continuity equation (3.3.6) presents the mass sources Γ_E, Γ_B and Γ_C, which account for evaporation, breakup and eventual collision/coalescence processes acting on droplets.

$$\frac{dm_d}{dt} = -\Gamma_E - \Gamma_B - \Gamma_C \tag{3.3.6}$$

The Lagrangian DDM method directly solves the motion of each spray parcel by integrating the momentum equation over time. Conceptually, the formulation (3.3.7) states that the rate of change of momentum is equal to the sum of acting forces on a spray droplet; therefore, it is directly derived from the second Law of Newton.

$$m_d \frac{d\vec{u}_{id}}{dt} = \vec{F}_{iD} + \vec{F}_{iG} + \vec{F}_{iP} + \vec{F}_{iEX} \tag{3.3.7}$$

The terms on the right hand side of equation (3.3.7) represent the components of resulting actions on droplet i: the drag force F_{iD}, the gravity and buoyancy force F_{iG}, the pressure force F_{iP} and the external force F_{iEX}. The formulation of drag force will be given in the sub models section 3.3.4. After the solution of the particle velocity components u_{id}, the instantaneous parcel position x_{id} could be integrated then.

$$\frac{dx_{id}}{dt} = \vec{u}_{id} \tag{3.3.8}$$

Parcels are tracked in the physical space without a dependence on the mesh distribution. Grid effects come from the definition of relative velocity between drops and gas cells.

The energy equation is presented according to the Dukowicz [21] assumptions for heat and mass transfer: droplets are spherical, with a quasi-steady gas film around the surface and uniform temperature. Furthermore, the surrounding fluid owns uniform physical properties and the liquid-vapour mixture on drops interface is in thermal equilibrium. These hypotheses lead to the energy conservation equation (3.3.9), which states that the rate of change in droplet temperature is determined assuming that the energy conducted to the droplet either heats up the parcel or supplies heat for vaporization.

$$m_d c_{pd} \frac{dT_d}{dt} = L_d \frac{dm_d}{dt} + \dot{q} \qquad (3.3.9)$$

The terms c_{pd}, T_d and L_d represent the specific heat of the liquid, the droplet temperature and the latent heat of evaporation. The convective heat flux from the gas to the droplet surface is expressed by $\dot{q}$ and, together with the rates of change in drops mass dm_d/d_t and temperature dT_d/d_t, need to be expressed through evaporation models.

The above described source terms for mass, momentum and energy could be expressed with different modeling approaches, as described later in section 3.3.4.

3.3.3. Transport with Eulerian approach

For each phase the complete set of conservation equations is resolved, i.e. mass, momentum and enthalpy. The resolution in the droplets diameter space increases with the number of phases, leading to an increase in computational effort.

The multiphase formulation of conservation equations for mass, momentum and enthalpy are shown in Equations (3.3.10), (3.3.11) and (3.3.12) [20]. Additional transport equations for turbulence kinetic energy and turbulence dissipation rate according to the k-ε model and a transport equation for the vapour mass fraction in the gaseous phase are solved.

$$\frac{\partial \alpha_k \rho_k}{\partial t} + \nabla \cdot \alpha_k \rho_k \vec{u}_k = \sum_{l=1,l\neq k}^{n} \Gamma_{kl} \qquad (3.3.10)$$

$$\frac{\partial \alpha_k \rho_k \vec{u}_k}{\partial t} + \nabla \cdot \alpha_k \rho_k \vec{u}_k \vec{u}_k = -\alpha_k \nabla p +$$

$$\nabla \cdot \alpha_k (\tau_k - T_k) + \alpha_k \rho_k \vec{g} + \sum_{l=1,l\neq k}^{n} \vec{M}_{kl} + \vec{u}_k \sum_{l=1,l\neq k}^{n} \Gamma_{kl} \qquad (3.3.11)$$

$$\frac{\partial \alpha_k \rho_k h_k}{\partial t} + \nabla \cdot \alpha_k \rho_k \vec{u}_k h_k = \nabla \cdot \alpha_k (q_k + q_k^t) +$$

$$\alpha_k \rho_k \theta_k + \alpha_k \tau_k \nabla \cdot \vec{u}_k + \alpha_k \frac{dp}{dt} + \sum_{l=1,l\neq k}^{n} H_{kl} + h_k \sum_{l=1,l\neq k}^{n} \Gamma_{kl} \qquad (3.3.12)$$

The exchange terms Γ_{kl}, M_{kl} and H_{kl} between the phases, visualized in Figure 3.2, are contained in the right hand sides of the previous equations. The corresponding models are conceptually the same as in the Lagrangian approach, even if the assumption of discrete droplets classes and the presence of volume fraction require some adjustments, which will be properly analyzed in the following paragraphs.
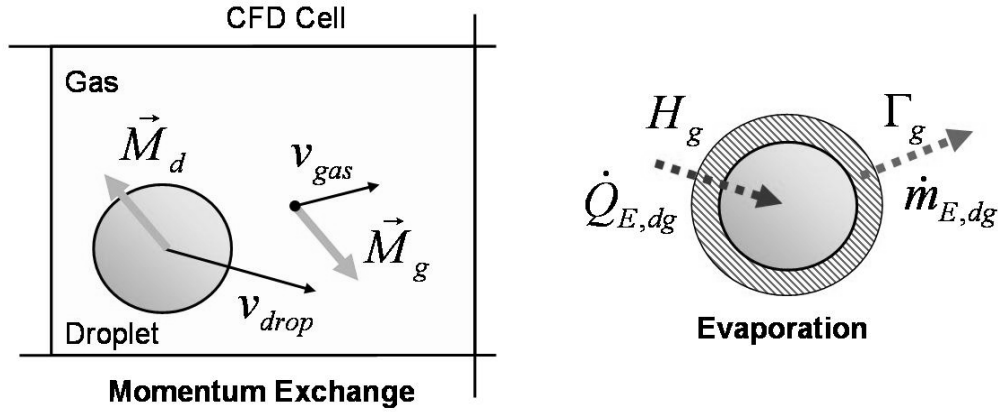

Figure 3.2: Drag (l.) and evaporation (r.) source terms between generic droplet *d* and gas *g*.

• **Mass exchange**

The contributions for the interfacial mass exchange Γ_{kl} between phase *k* and *l* come from evaporation $\Gamma_{E,kl}$, primary break-up $\Gamma_{P,kl}$ and secondary break-up $\Gamma_{S,kl}$, as shown in equation (3.3.10). All the sources could theoretically get a negative or positive sign, according to a loss or a gain of mass. All the mass exchange rates are modeled for a single droplet, therefore they need to be multiplied by the number of droplets per unit volume, called droplet number density, which is given by $N_k = 6\alpha_k/\pi d_k^3$.

$$\Gamma_{kl} = \Gamma_{E,kl} + \Gamma_{P,kl} + \Gamma_{S,kl} = \frac{6\alpha_k}{\pi\, d_k^3}\left(\pm \dot{m}_{E,kl} \pm \dot{m}_{PB,kl} \pm \dot{m}_{SB,kl}\right)$$

$$\text{with} \quad \dot{m}_{PB,kl} = \rho_k \pi\, d_k^2 \left(\frac{dr_k}{dt}\right)_{PB,kl} ; \; \dot{m}_{SB,kl} = \rho_k \pi\, d_k^2 \left(\frac{dr_k}{dt}\right)_{SB,kl} \tag{3.3.13}$$

The term $\dot{m}_{E,kl}$ represents the mass exchange rate of a single droplet, which is calculated according to the chosen evaporation model. In the case of adoption, the primary break-up model describes the disintegration process from the bulk liquid phase n into the other liquid droplet phases. The term $\dot{m}_{PB,kl}$ is related to the radius decay rate *(dr/dt)$_{PB,kl}$* of the parcels initialized at the nozzle hole. The secondary atomization process is defined by the term $\dot{m}_{S,kl}$, which is proportional to the radius change rate *(dr$_k$/dt)$_{S,kl}$* of each liquid phase in each cell.

• **Momentum exchange**

Drag forces $M_{D,kl}$ and turbulent dispersion forces $M_{T,kl}$ determine the momentum exchange M_{kl} between gaseous phase and each liquid one, as shown in equation (3.3.14).

$$\vec{M}_{k1} = \vec{M}_{D,k1} + \vec{M}_{T,k1} =$$
$$= c_D \frac{6\alpha_k \rho_1}{d_k} |\vec{u}_1 - \vec{u}_k| (\vec{u}_1 - \vec{u}_k) + c_T \rho_1 k_1 \nabla \alpha_k = -\vec{M}_{1k}$$

(3.3.14)

Drag coefficient c_D is modelled as in the Lagrangian approach, therefore as a function of Reynolds number, droplet deformation and, in this case, liquid volume fraction. Turbulent dispersion force and its coefficient c_T [49] are taken into account only in the multi-dimensional Eulerian formulation.

- **Enthalpy exchange**

The term H_{k1} in equation (3.3.15) represents the interfacial enthalpy exchange between gas and liquid phases and is determined by the evaporation model. The heat flow rate $\dot{q}_{E,kl}$, which represents the energy exchange between a single droplet and the surrounding gas, is calculated according to the chosen evaporation model.

$$H_{k1} = N_k \dot{q}_{E,k1} = \frac{6\alpha_k}{\pi d_k^3} \dot{q}_{E,k1} = -H_{1k}$$

(3.3.15)

3.3.4. Sub models

In this section the most common spray models will be briefly outlined; as affecting source terms or parcel diameter variation, the models themselves could be used both for Lagrangian and Eulerian approach. The description of droplets through discrete parcels or volume fraction then requires formal adjustments in model implementation, which will not be presented in the current thesis.

- **Drag**

Drag force represents the momentum interaction between droplets and surrounding gas and it could be expressed as a function of the relative velocity u_{rel} between both entities:

$$\vec{F}_{iD} = D \, \vec{u}_{i,rel} = D \, (\vec{u}_{ig} - \vec{u}_{id})$$

(3.3.16)

D is the drag function and it is generally formulated as a function of the cross sectional area of the parcel A_d.

$$D = \frac{1}{2} \rho_g A_d C_D |\vec{u}_{rel}|$$

(3.3.17)

The drag coefficient C_D depends on the droplet Reynolds number Re_d and is expressed in different forms according to the assumed particles shape. For example the drag coefficient for a single sphere could be formulated like in equation (3.3.19) [75].

$$Re_d = \frac{\rho_g |\vec{u}_{rel}| d_d}{\mu_g}$$

(3.3.18)

$$C_D = \begin{cases} \dfrac{24}{Re_d}\left(1 + 0.15 Re_d^{0.687}\right), & Re_d < 10^3 \\ 0.44, & Re_d \geq 10^3 \end{cases}$$

(3.3.19)

Turbulent dispersion effects could be included in the drag force as a statistical fluctuating component [57]. In the case of fuel injection the drag force is the most relevant in terms of magnitude. By neglecting pressure and external forces, the droplet motion equation could be rewritten as

$$\frac{d\vec{u}_{id}}{dt} = \frac{3}{4}C_D \frac{\rho_g}{\rho_d}\frac{1}{d_d}|\vec{u}_{ig} - \vec{u}_{id}|(\vec{u}_{ig} - \vec{u}_{id}) + \left(1 - \frac{\rho_g}{\rho_d}\right)\vec{g}$$

(3.3.20)

- **Evaporation**

The described evaporation approach follows the Dukowicz formulation [21]. The basic idea is to use a two-component system in the gas-phase, composed of the vapour and the non-condensable gas, even though each component may consist of a mixture of different species. The governing law for the mass flux may be formulated defining $\dot{q}_s$ and $\dot{m}_{vs}$ as local surface heat flux and vapour mass flux, with the assumption of uniformity of droplet surface conditions.

$$\frac{dm_d}{dt} = \dot{q}\frac{\dot{m}_{vs}}{\dot{q}_s}$$

(3.3.21)

Starting from equation (3.3.9), the droplet energy equation could be then rearranged.

$$m_d c_{pd}\frac{dT_d}{dt} = \dot{q}\left(1 + L_d \frac{\dot{m}_{vs}}{\dot{q}_s}\right)$$

(3.3.22)

Both equations describe the rates of change in droplet mass and temperature, with the term $\dot{m}_{vs}/\dot{q}_s$ which needs to be modeled.

$$\frac{\dot{m}_{vs}}{\dot{q}_s} = \frac{\rho\beta}{k}\left(\frac{1}{1 - Y_{vs}}\right)\frac{\nabla_s Y_v}{\nabla_s T}$$

(3.3.23)

The expressions Y_v and Y_{vs} respectively describe the local mass fractions of vapour and its boundary value at parcel surface, β the binary diffusion coefficient and k the heat

conductivity. An analogy consideration on heat and mass transfer differential equations then leads to a formulation of the unknown term in equation (3.3.23).

$$\frac{\nabla_s Y_v}{\nabla_s T} = \frac{Le}{c_{pd}} \left[\frac{h_\infty - h_s}{Y_{v\infty} - Y_{vs}} - h_{vs} + h_{gs} \right] \qquad (3.3.24)$$

The index s and ∞ refers respectively to enthalpy h and vapour mass fraction Y_v at droplet surface and in the surrounding environment. Assuming Lewis number Le equal to 1 and defining the mass transfer number B_Y, the flux ratio could be written in equation (3.3.26) in its final form.

$$B_Y = \frac{Y_{v\infty} - Y_{vs}}{1 - Y_{vs}} \qquad (3.3.25)$$

$$\frac{\dot{m}_{vs}}{\dot{q}_s} = \frac{-B_Y}{h_\infty - h_s - (h_{vs} - h_{gs})(Y_{v\infty} - Y_{vs})} \qquad (3.3.26)$$

The vapour mass flux dm_d/dt could then be calculated and introduced into the energy equation (3.3.9). The convective heat flux from the gas to the droplet surface $\dot{q}$ could be formulated as a function of the droplet surface area A and of the convective heat transfer coefficient α through the film surrounding the droplet in the absence of mass-transfer.

$$\dot{q} = \alpha A (T_\infty - T_S) \qquad (3.3.27)$$

According to Dukowicz's model formulation for $\dot{Q}$, the energy equation for a droplet may be presented as

$$m_d c_{pd} \frac{dT_d}{dt} = L \frac{dm_d}{dt} + Nu \cdot 2\pi \, r_d \, k_g \left(T_g - T_d \right) \qquad (3.3.28)$$

where k_g is the heat conductivity, T_g the temperature of the ambient gas and Nu the Nusselt number (Nu) is modeled [63] as a function of Reynolds (Re) and Prandtl (Pr) numbers.

$$Nu = 2 + 0.6 \, Re^{1/2} \, Pr^{1/3} \qquad (3.3.29)$$

Transport properties like vapor viscosity, specific heat, thermal conductivity etc. are evaluated according to the reference temperature T_{ref} between the local domain fluid temperature T_∞ and the droplet surface temperature T_s.

$$T_{ref} = \frac{T_\infty - T_s}{2} \qquad (3.3.30)$$

Convection theories from Sparrow and Gregg [82] suggested the adoption of a 1/3-law for the reference temperature.

$$T_{ref} = \frac{2}{3}T_s + \frac{1}{3}T_\infty$$
(3.3.31)

The term T_{ref} consequently affects the values of the fluid properties in the computation of characteristic non-dimensional numbers, which are adopted for advanced evaporation modeling. Reynolds, Schmidt and Prandtl numbers for the droplets could be described by

$$Re = \frac{u_{rel}d_d\rho_{g,\infty}}{\mu_{g,ref}} \qquad Sc = \frac{\mu_{g,ref}}{\rho_{g,ref}\beta_{ref}} \qquad Pr = \frac{\mu_{g,ref}c_{p\,g,ref}}{\lambda_{g,ref}}$$
(3.3.32)

The approach of Dukowicz allows resolving both terms dm_d/dt and dT_d/dt according to the formulation of mass and heat flux relationship $\dot{m}_{vs}/\dot{q}_s$. Another idea for the modeling of single drops evaporation came from the studies of Frössling [31]: the derived model is known as Spalding model and it was first implemented in the KIVA II code. Droplet radius reduction is calculated independently from the mass flux, which is formulated with the Dukowicz approach. First of all the parcels energy equation (3.3.9) has to be re-written according to homogeneous spherical droplets of radius r_d.

$$m_d c_{pd}\frac{dT_d}{dt} - L_d\rho_d 4\pi r_d^{\,2}\frac{dr_d}{dt} = 4\pi r_d^{\,2}\dot{q}$$
(3.3.33)

The correlation for the rate of change in particles size could be expressed as

$$\frac{dr_d}{dt} = \frac{(\rho\beta)_g}{2\rho_d r_d}\cdot\frac{Y_{vs}-Y_{v\infty}}{1-Y_{vs}}Sh$$
(3.3.34)

where Sh is the Sherwood number, calculated by

$$Sh = 2 + 0.6Re^{1/2}Sc^{1/3}$$
(3.3.35)

and corrected by the factor $ln(1+B_Y)/B_Y$, accounting for the vapour diffusion away from the droplet (Stefan flow)

$$Sh = Sh_0\,\frac{\ln(1+B_Y)}{B_Y}$$
(3.3.36)

Heat flux is formulated with the Dukowicz approach, even if the Nusselt number is also corrected by the factor $ln(1+B_Y)/B_Y$. The resulting energy equation may be written as

$$\rho_d\frac{2}{3}r_d^{\,2}c_{pd}\frac{dT_d}{dt} = k(T_\infty - T_d)Nu\,\ln\frac{(1+B_Y)}{B_Y} + (\rho\beta)_g B_Y Sh$$
(3.3.37)

In comparison with the stationary droplet, the relative motion between spray particles and gas phase leads to increasing exchange processes. Starting from the Ranz and Marschall [63] empirical correction of Nusselt and Sherwood numbers,

$$Nu_0 = 2 + 0.552 \ Re^{1/2} Pr^{1/3} \tag{3.3.38}$$

$$Sh_0 = 2 + 0.552 \ Re^{1/2} Sc^{1/3} \tag{3.3.39}$$

Abramzon and Sirignano [1] proposed a further modification to account for the deviation of streamlines due to evaporating mass flow.

$$Nu^* = 2 + \frac{(Nu_0 - 2)}{F_T} \qquad Sh^* = 2 + \frac{(Sh_0 - 2)}{F_M} \tag{3.3.40}$$

The correction functions F_T and F_M have the same structure

$$F(B) = (1 + B)^{0.7} \frac{\ln(1 + B)}{B} \tag{3.3.41}$$

with B_Y and B_T as mass and temperature transfer numbers. The method is iterated until the correction on calculated B_T fulfills a defined convergence criterion. Although higher computational cost, the advantages of the model could be found in deeper physical accuracy and no limitations on Lewis number, set to 1 in the Dukowicz approximation.

In the current work the Eulerian spray model from AVL is run with the evaporation model from Abramzon and Sirignano, while StarCD uses the Dukowicz approach.

• **Secondary Break-up**

There are many methods to define the atomization process of liquid jets, from approximations of single droplets to direct numerical simulations [74]. In the CFD simulation of a combustion engine, sprays are usually assumed to be made of spherical parcels. Hence, the analysis of single droplets break-up represents the basis of standard atomization models, as the ones described in the current section.

In the break-up model from Reitz and Diwakar [67] the atomization process is divided into two regimes: bag and stripping break-up for low and high relative velocities between droplets and surrounding gas. The disintegration of drops into smaller particles is supposed to happen as they reach an unstable condition related to the droplets Weber number We_d. This correlation can be explained as the Weber number quantifies the relevance of inertia forces in comparison with surface tension forces, which tend to constrain the aerodynamic atomization process.

$$We_d = \frac{\rho_d u_{rel}^2 r_d}{\sigma} \tag{3.3.42}$$

As the unstable condition is reached, in the stripping regime the viscosity effects are dominant to determine the droplets break-up. The rate of change in droplets radius r_d is then defined with a logarithmic law as:

$$\frac{dr_d}{dt} = \frac{-(r_d - r_{d,stable})}{\tau_B}$$

(3.3.43)

The term $r_{d,stable}$ represents the droplet radius at a stable condition, while τ_B is the characteristic break-up time. Both terms are differently modeled according to the atomization regime, as shown in table 3.1.

	Regime criteria	Stable drop radius	Characteristic break-up time
Bag break-up	$We_d > 6$	$r_{d,stable} = \dfrac{6\sigma}{\rho_d v_{rel}^2}$	$\tau = C_1 \left(\dfrac{\rho_d r_d^3}{2\sigma} \right)^{0.5}$
Stripping break-up	$\dfrac{We_d}{\sqrt{Re_d}} > 0.5$	$r_{d,stable} = \dfrac{\sigma^2}{2\rho_d^2 v_{rel}^3 \nu}$	$\tau = C_2 \dfrac{r_d}{v_{rel}} \left(\dfrac{\rho_d}{\rho_g} \right)^{0.5}$

Table 3.1: Reitz-Diwakar break-up model.

The simulation time step dt is usually much smaller than the characteristic break-up time, therefore the droplets size is gradually reduced until they reach a stable state. The constants C_1 and C_2 then need to be adjusted in order to fit the experimental data.

Another widespread break-up approach is the WAVE model from Reitz [68], based on the Rayleigh-Taylor instability ([65] and [91]), which occurs when a dense, heavy fluid is accelerated by light fluid. The growth of a perturbation on the liquid surface is linked to its wavelength Λ and the unstable condition is linked to the droplet Weber number. At high velocities the size of the product droplets is set equal to the wavelength of the most probable unstable or fastest growing surface wave, with a correction factor C_1:

$$r_{d,stable} = C_1 \Lambda$$

(3.3.44)

The characteristic break-up time is formulated as in table 3.1 for the stripping regime. At low Weber numbers the Rayleigh type break-up occurs, leading to larger droplets than the original drops. Nevertheless, this last regime is not of interest for high pressure injection systems.

Literature proposes many other approaches in the modeling of spray atomization. Some examples are the Taylor Analogy Break-up (TAB) model from O'Rourke[59], the FIPA model from Pilch and Erdman [62] or the KH-RT model [88], based on the competition between the Kelvin-Helmoltz surface waves and Rayleigh-Taylor disturbances acting on droplets.

- **Primary Break-up**

The primary break-up models try to define the transition from the nozzle flow to the dispersed spray in the region close to the nozzle orifice. The effects of turbulent velocity fluctuations, collapsing cavitation bubbles and aerodynamic interactions lead to a complex process that strongly affects the initialization of the spray.

The primary break-up model implemented in Fire follows the work of Bianchi and Pelloni [13]. Originally developed by Huh and Gosman [39], the method considers the aerodynamic

surface wave growth and the internal turbulence stresses as two independent mechanisms. A coherent liquid core at the nozzle exit is assumed to lose mass under the action of turbulent fluctuations and aerodynamic pressure forces. The diameter of product droplets d_d is set equal to the turbulent length scale L_t at the nozzle orifice cross section.

$$d_d \approx L_t = C_1 C_\mu \frac{\kappa^{1.5}}{\varepsilon} \qquad (3.3.45)$$

The constant C_μ is set equal to 0.09, while C_1 could be varied in order to fit the experimental results. The break-up time scale is then related to the turbulent and aerodynamic time scales τ_t and τ_a.

$$\tau_t = C_\mu \frac{\kappa}{\varepsilon} \qquad (3.3.46)$$

$$\tau_a = L_t \left[\frac{\rho_g \; \rho_d \; u_{inj}^{\;\;2}}{(\rho_g + \rho_d)} - \frac{\sigma}{(\rho_g + \rho_d) \; L_t} \right]^{-0.5} \qquad (3.3.47)$$

The aerodynamic time scale is obtained from the Kelvin-Helmoltz instability theory, using the turbulent length scale L_t as the characteristic value for the unstable wavelength. The final expression of the break-up time τ_B is obtained with two weighting factors C_1 and C_3, both depending on calibration with experimental data.

$$\tau_B = C_1 \; \tau_t + C_3 \; \tau_a \qquad (3.3.48)$$

• Turbulent dispersion

The interaction between gas flow and particles could be correctly reproduced only with the solution of the singular turbulent eddies. As this condition is neglected by the RANS approach, a turbulent dispersion model is required. The interaction between parcels and turbulent flow is estimated from the time required by the particle to cross the eddy and the turbulent eddy life time.
In the model of O'Rourke [57] the interaction between the turbulent flow is not described with the introduction of a velocity fluctuation component, contrariwise new particle location and velocity are computed with a statistical approach. Gaussian distributions for velocity and position are used, with the variances σ^2 calculated as follows:

$$\sigma_{u'}^2 = \sigma^2 \frac{1 - e^{-D \, t_{turb}}}{1 + e^{-D \, t_{turb}}} \left(1 - e^{-2D \, \Delta_t} \right) \qquad (3.3.49)$$

$$\sigma_{x'}^2 = \frac{\sigma_{u'}^2}{D^2} + \sigma^2 \left[t_{turb} \Delta t - \frac{2 t_{turb}}{D} \left(1 - e^{-D \, \Delta t} \right) \right] \qquad (3.3.50)$$

The term σ is the standard deviation of the Gaussian distribution, D is the drag function already defined in equation (3.3.17), t_{turb} is the turbulence correlation time and Δt is the computational time step. Particle position x_{id} and velocity u_{id} are then updated from condition n to $n+1$ according to the turbulence persistence time t_{per}, which represents the dependency between velocity and position change.

$$t_{per} = \frac{\sigma^2}{\sigma_{u'}^2} t_{turb} \left(1 - e^{-D \Delta t}\right) - \frac{1}{D} \qquad (3.3.51)$$

$$u_{id}^{n+1} = u_{id}^{n+1} + \sigma_{u'} \qquad (3.3.52)$$

$$x_{id}^{n+1} = x_{id}^n + \sigma_{x'} - \sigma_{u'} t_{per} \qquad (3.3.53)$$

3.4. Lagrangian Spray Tests

Drops parcels are introduced at the injector hole location with a specified droplet diameter, velocity and temperature. Injection velocities are usually determined from measured mass flow rate of the injector nozzle. As mentioned in paragraph 3.3.1, a great problem of the DDM approach is the high mesh and environment conditions dependency.

In this section an evaluation of grid effects will be carried out through simulations by two different CFD codes, Star-Cd and Kiva-3v. The modified parameters will be meshes, spray initialization and turbulent dispersion models. The calculations will be performed in a cold environment, in order to avoid the influence of evaporation on the results. The simulations will be performed on two-dimensional orthogonal and spray adaptive meshes: the cells dimension distribution will change in the direction orthogonal to the injection axis.
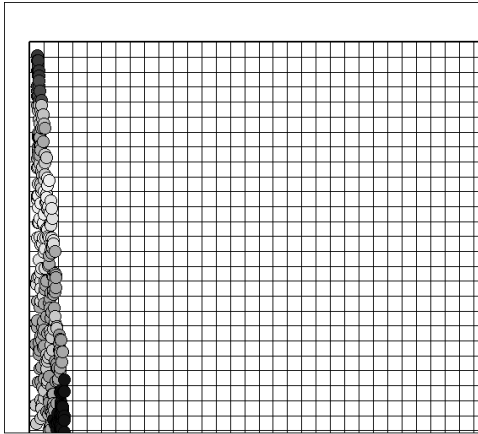
Mesh 1 - Orthogonal Rough
$\Delta x = 1$ mm (5000 cells)
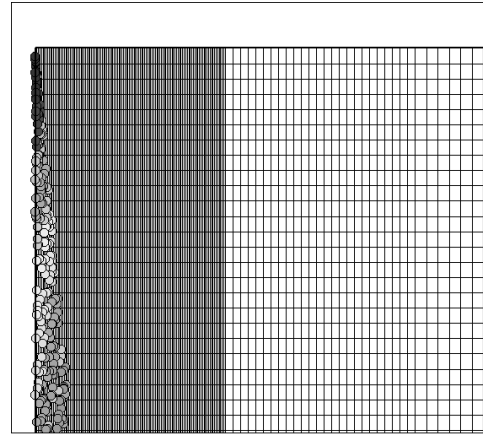
Mesh 2 - Orthogonal Fine
$\Delta x = 0.1$ mm (17000 cells)

Figure 3.3: Orthogonal 2D meshes.

The first meshes were created with a orthogonal Cartesian grid. They were made of a 0.5° rectangular sector with a constant cells spacing (Δy) of 1 mm in axial direction and variable (Δx) in radial direction: this could assure a different solution of the velocity gradient near the

injection point. The Δx values were chosen in a range from 0.1 to 1 mm, as shown in Figure 3.3. The dimension of the computational domain was 40x120 mm^2, in order to guarantee the spray penetrations obtained in the experimental data set.

Afterwards two adaptive meshes werewere considered, whose shape was directly extracted from a 3D bowl mesh of an internal DC truck engine (see Figure 3.4). Also in this case it is assigned to the 2D meshes the "fine" and "rough" identifications.

Simulation results will be compared to DaimlerChrysler experimental data in an optically accessible chamber. Injection rates and penetration curves are available for a common rail injection system, 6 holes nozzle, 800 bar rail pressure, 50% load, cold chamber (p = 20 bar; T = 293 K).

Mesh 3 – Adaptive Rough

2975 cells

Mesh 4 – Adaptive Fine

7296 cells
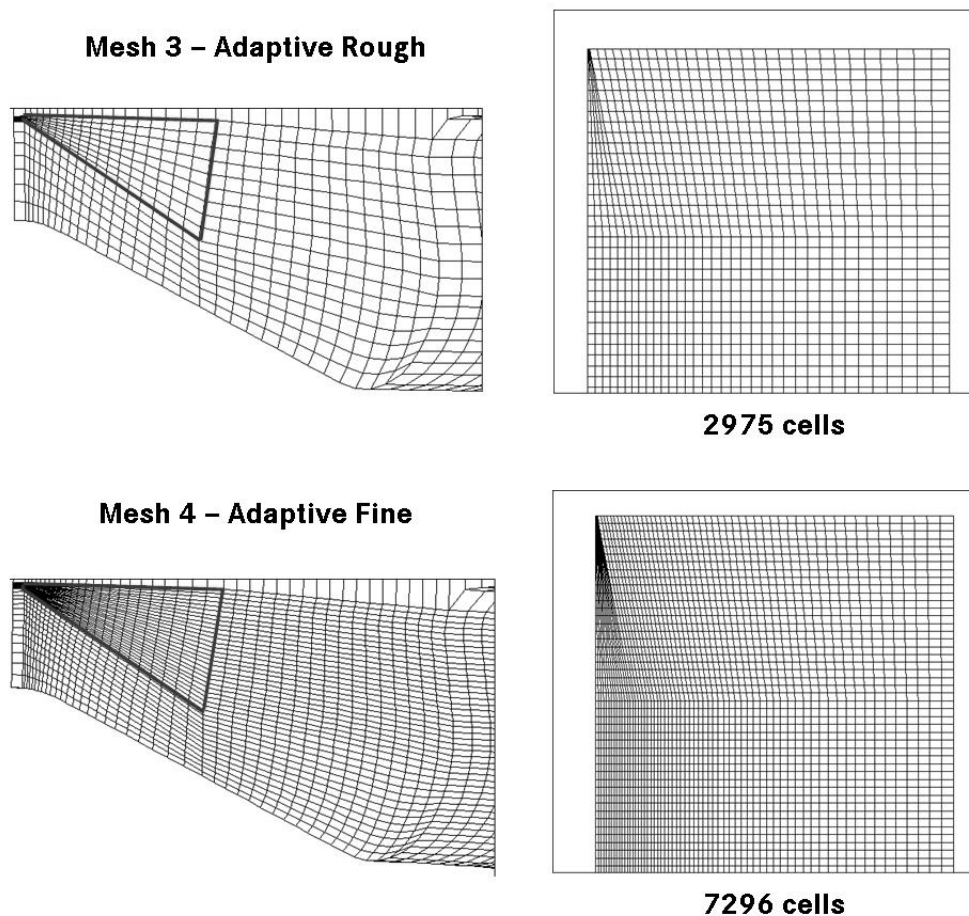
Figure 3.4: Creation of adaptive meshes.

The simulations were performed with Star-CD and Kiva-3v CFD codes. The aim is to compare the implementations of both codes. The entrainment of new particles into the domain is performed both with blob method coupled with break up model and with constant 1 μm diameter of parcels without break-up.

In the so-called blob method the injection process starts with large droplets of orifice diameter, introduced in the chamber at nozzle hole position. The dimension of parcels is reduced according to the rate approach of a chosen break-up model. The jet appears therefore to be represented by a series of parcels with diminishing diameters. In order to get an acceptable spray the break up rate needs to be increased, leading to fast atomization and fast reduction of droplets momentum. A disadvantage of the approach is the very slow evaporation process near the injector, due to the presence of parcels with high diameters.

The number of injected parcels amount to 5000 entities, a reasonable value according to the 0.5° simulation sector. Injection velocities are extracted from the experimental injection rate, according to an injected mass per-hole of $m_{inj} = 2.285e-5$ kg. The direction of injection could be randomly deviated by an angle α_{inj}, in order to force the spray dispersion near the injector. In our case two different angles were considered: 0° and 12°.

The thermodynamical conditions in the computational domains are a temperature T = 293 K, and a pressure p = 20 bar in N_2 ambient gas. The turbulence level is set to $\varepsilon = 1$ m^2/s^2 and $l_T = 0.001$ m.
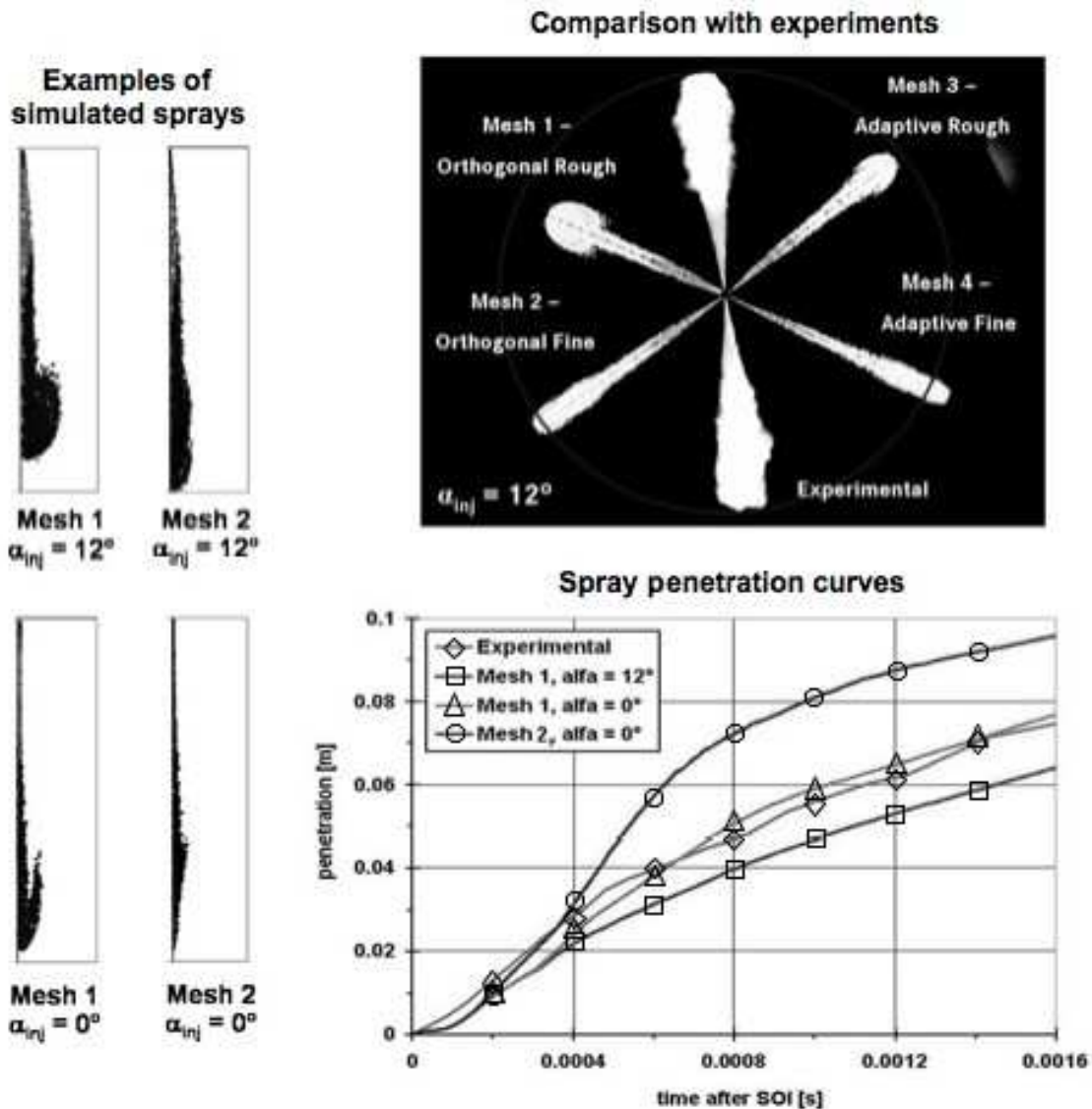
Figure 3.5: Star-CD spray simulations (pictures at t = 0.0016 s).

The first simulations werewere performed on the orthogonal meshes with Kiva-3v and Star-CD. It was clear immediately that the Star-CD standard dispersion model was heavily mesh-dependent and practically inapplicable for the finest cell dimensions. With an injection angle of $\alpha_{inj} = 0°$ the spray shapes appeared more and more like arrows moving towards finer grids: this can be easily seen in Figure 3.5. Also with an injection angle of 12° the spray showed a big mesh dependency, as seen in the penetration curves of Figure 3.5.

With the adaptive meshes the spray shapes appeared very thin and without the angular dispersion that the experimental images showed. Both in the orthogonal and adaptive cases,

the rough mesh led to a spray shape with a rounded head: this fact underlined that the dispersion only took place far away from the injector. The simulations in fine grids with injection angle of 12° showed better shapes and penetrations than the simulations in rough grids; nevertheless, the spray angle appeared simply defined from the initialization angle α_{inj}. Finally, penetrations for adaptive meshes were slightly better than for orthogonal ones (see experimental photo with superposed simulated spray images in Figure 3.5).

Also the influence of turbulence initialization was taken into account: a high turbulence level ($\kappa = 10$ m^2/s^2 and $l_T = 0.01$ m) was compared with a low turbulence level ($\kappa = 1$ m^2/s^2 and $l_T = 0.001$ m). The results showed a big influence of turbulence in orthogonal rough meshes, as penetration curves differed by nearly 1 cm at the end of thesimulation. Turbulence initialization had a lower influence in the orthogonal fine and adaptive grids, as penetrations appeared very close (see Figure 3.6).
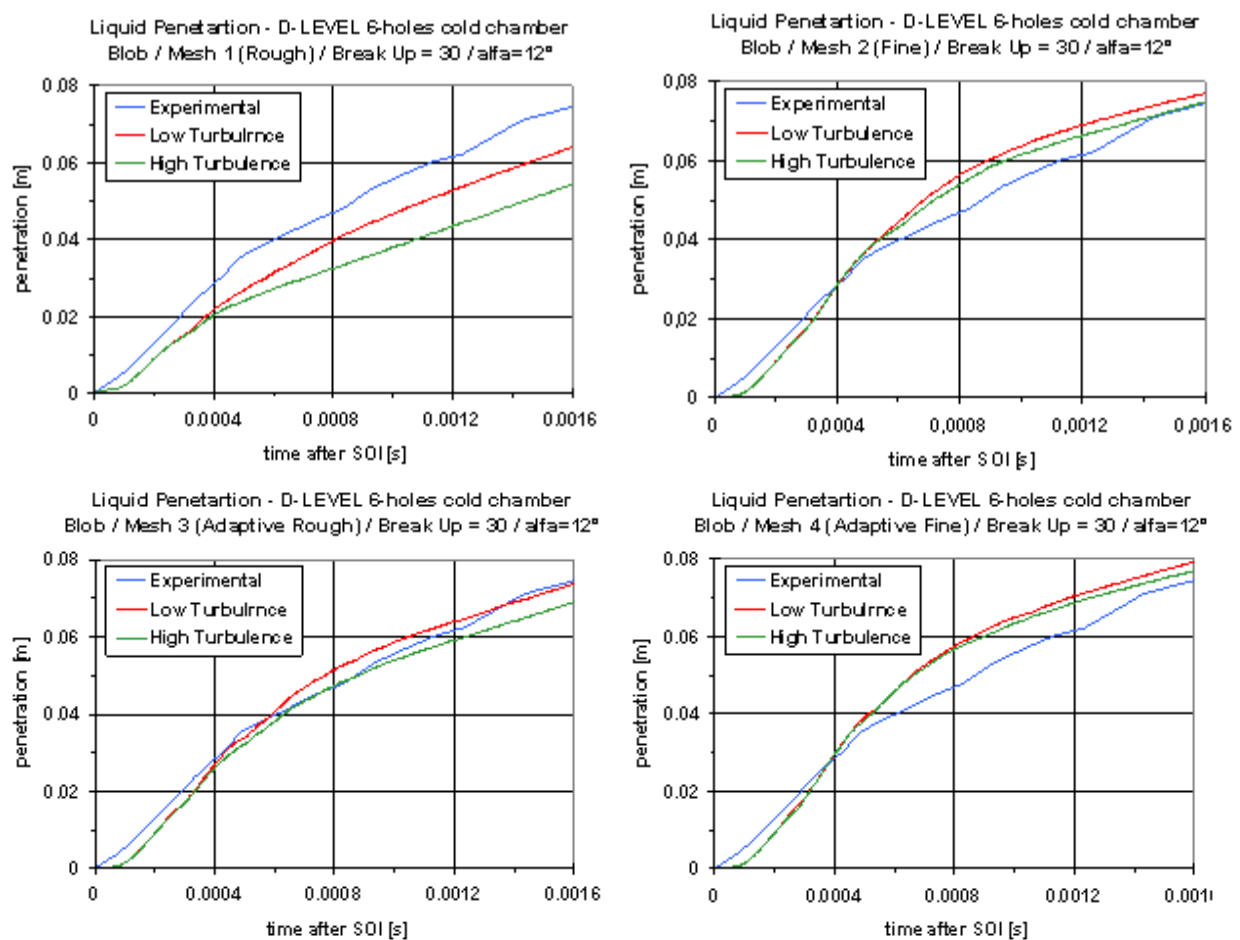
Figure 3.6: Turbulence influence in Star-CD spray simulations, $\alpha_{inj} = 12°$.

The simulations performed with Kiva-3v code showed a higher dispersion of the spray, even with an injection angle of 0°: the Kiva-3v spray shapes appeared wider and not concentrated along the spray axis, while Star-CD provided "arrow-shaped" sprays (see Figure 3.7). All the previous simulations were performed in both codes with a computational time-step of 1e-6 s, indispensable to resolve the spray dynamics.

The adoption of a new turbulent dispersion model for droplets [36] provided better results on spray formation. Anyway, the performed tests showed a great sensitivity to initialization and models. Mesh quality, turbulence level and injection angles appeared to have a great influence

on spray development, leading to the perception of a method requiring great tuning of parameters.
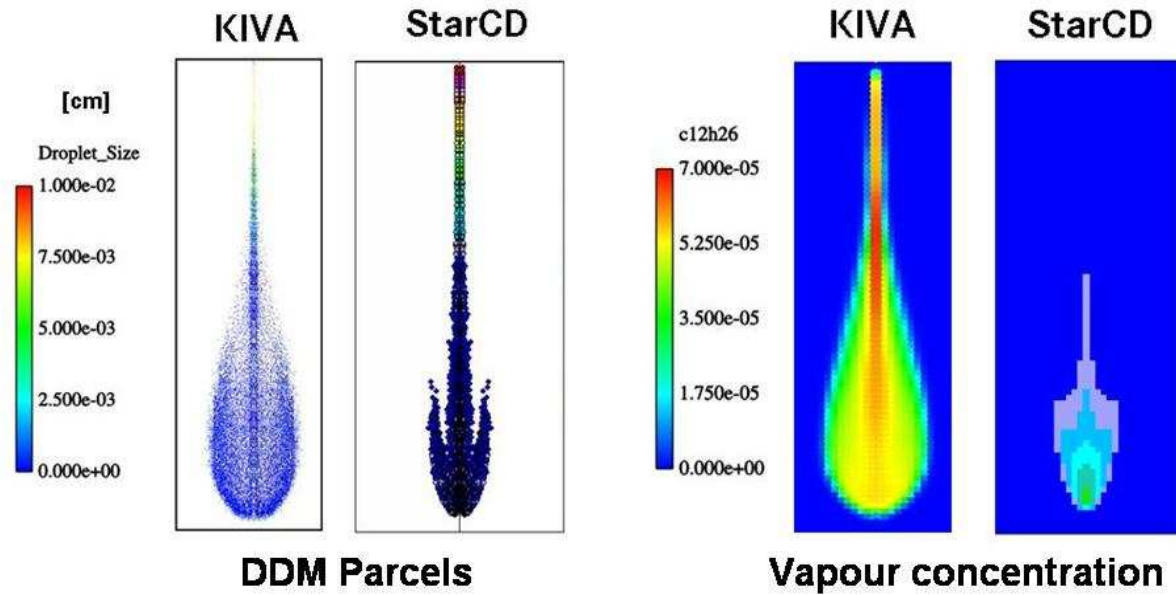
Figure 3.7: Comparison between Kiva 3v and Star-CD for coarse mesh and $\alpha_{inj} = 0°$.

3.5.   Eulerian Spray Concept

In this thesis two different Eulerian spray models will be adopted: the 1D ICAS and the AVL 3D Eulerian. These two approaches will be analyzed and compared in the following paragraphs, trying to underline limits and advantages of both.

In the case of the primary breakup model, a droplet phase could represent the bulk liquid of the flow streaming outside the nozzle hole. A schematic representation is shown in table 3.2.

Phase	1	2, ..., n-1	n
Physical	Gas mixture	Droplets	Bulk liquid

Table 3.2: Phase specification in the Eulerian spray

Further on two different multiphase spray approaches will be described and applied: the ICAS 1D-Model [44] and the 3D-Eulerian Spray developed from AVL [12]. Momentum, mass and energy exchanges between gas and droplets phases are described in the same way, as well as the vapour, transported as a scalar in the gaseous phase. Furthermore turbulent kinetic energy and dissipation rate are resolved in both approaches according to the $\kappa\text{-}\varepsilon$ model. The main difference consists of the modeling of the exchange terms between the droplets phases and on the definition of boundaries and mean value of each droplets class.

As shown in Figure 3.8, in the ICAS model droplets phases exchange terms only with the gas phase, modifying their characteristic diameter according to break-up and evaporation. On the other hand, the 3D Eulerian Model from AVL imposes the definition of constant class diameters and allows mass and momentum transfer between the parcels phases. A more detailed analysis will be held in the following paragraphs.
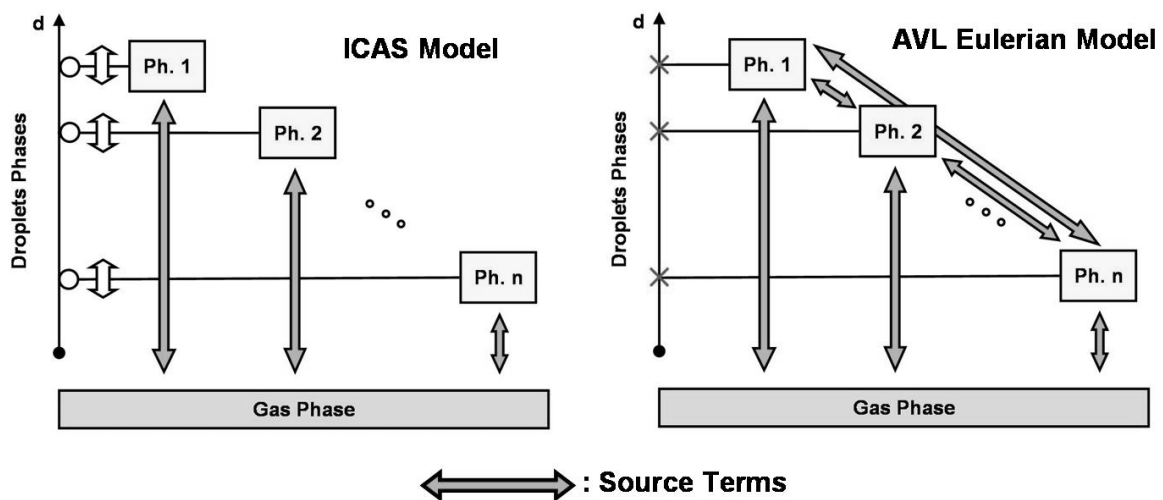
Figure 3.8: Conceptual differences between 1D-ICAS and 3D-AVL Eulerian Spray models.

3.5.1. 1D-ICAS Model

The Interactive Cross-Section Averaged Spray (ICAS) model [44] is a 1D Eulerian approach intended to describe the liquid jet atomization in a conical region just outside the nozzle. A chosen amount of droplets phases is transported along a one-dimensional grid extruding in the axial direction of injection. Adopting the ICAS model on an engine mesh, the source terms between the liquid and gas phase are mapped in a conical domain overlapping the two meshes through the selection of a defined spray angle.
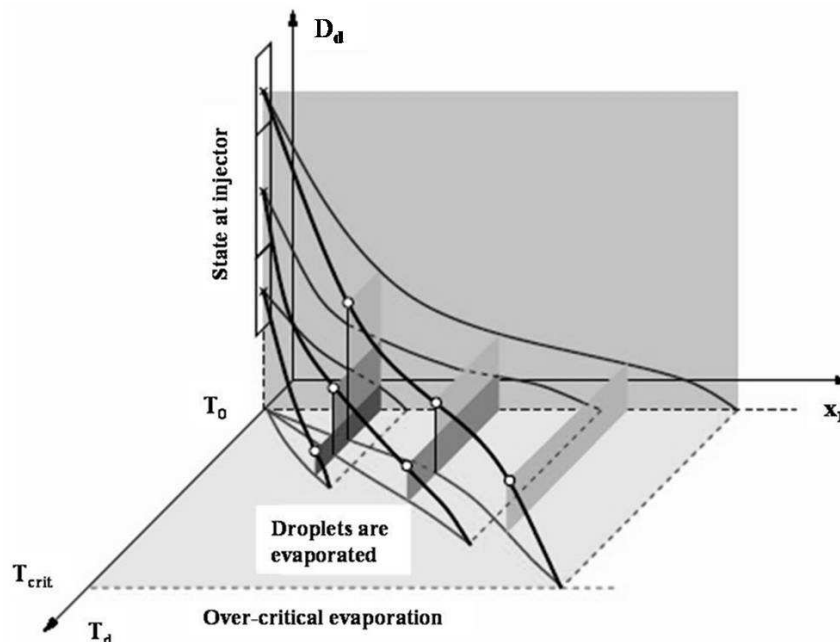
Figure 3.9: Process of class diameter reduction in ICAS model [44].

One of the most innovative concepts is the assumption that the border of each droplet class could change during the spray development. Processes like evaporation and break-up produce a constant decay of parcels diameter, as shown in Figure 3.9.

The limit of the method is primary to neglect more-dimensional effects, like turbulent dispersion or gas cross flow on spray. Nevertheless, the robustness and stability of the model affirmed its success in industrial applications at DaimlerChrysler.

The conservation equations and the models are a one-dimensional reduction of the 3D case: for this reason they will be treated in the following paragraph.

3.5.2. 3D Eulerian Spray

For each phase the complete set of conservation equations is resolved, i.e. mass, momentum and enthalpy. The resolution in the droplets diameter space increases with the number of phases, leading yet to an increase in computational effort. The adopted model was developed by AVL and is currently used in Fire v8 CFD code [7]. The main difference with ICAS is the hypothesis of constant droplets classes: the discrete process of atomization leads therefore to an exchange of mass between the liquid phases. An improvement of the model towards adaptive classes boundaries is under development.

3.5.3. Quantification of Numerical Errors

In order to estimate the mesh dependency of the adopted Eulerian Spray, a discretizations study was done. The considered method for error estimation is the Grid Convergence Index (GCI) [72]. The basic idea consists on the adoption of the Richardson extrapolation method [69], which is valid only for grids within an asymptotic range. The method itself requires the adoption of three meshes with increasing refinement and the definition of a key variable important to the objectives of the simulation study.
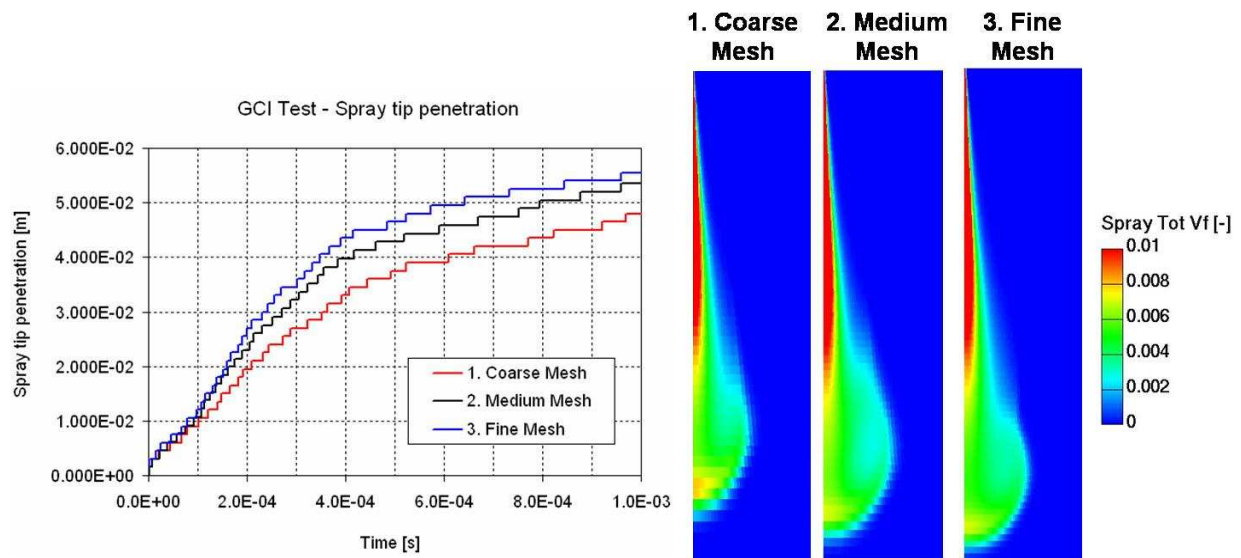
Figure 3.10: Penetration curves and spray shapes for the GCI numerical errors analysis.

First, a coarse two-dimensional grid (3) was meshed; afterwards, two further refinements were performed, creating an intermediate (2) and a fine (1) mesh. Injection velocities were taken from [11] and the three meshes present respectively 3, 4 and 5 cells at the inlet boundary. Spray tip penetration was chosen as the key variable for the GCI study. Figure 3.10 shows the results in terms of spray penetration and shape for the three cases.

The cells numbers N, the grid refinement factors r_{21} and r_{32}, the values of key variables ϕ, the approximate relative error, the extrapolated relative error e_{ext}^{21} and the fine grid convergence index GCI_{fine}^{21} are shown in Table 3.1.

	ϕ = Liquid tip penetration [m]
N_1, N_2, N_3	11700, 5200, 1950
r_{21}	1.310
r_{32}	1.387
ϕ_1	0.0555
ϕ_2	0.0535
ϕ_3	0.0480
e_a^{21}	3.60 %
e_{ext}^{21}	3.22 %
GCI_{fine}^{21}	4.16 %

Table 3.3: GCI calculation of discretizations error.

According to table 3.3, the numerical uncertainty in the spray penetration should be reported as 4.16 %. Unfortunately, a comparison with other CGI results was not found in the multiphase spray literature.

This kind of approach could not provide a quantification of modeling errors, as the GCI by definition estimates only the errors due to insufficient spatial discretization. Nevertheless, the adoption of a fine enough grid could lead to an acceptable error in terms of grid effects.

4. Nozzle Flow

Firstly an overview of the most important physical aspects of the internal flow through a nozzle will be given. The multiphase simulation of nozzle flow requires the definition of at least two phases, liquid and vapour fuel, and eventually air for the boundary conditions in the injection chamber. Thermodynamics of these states of aggregation plays a determining role on the selection of models and boundaries, therefore a brief introduction will be provided.
Afterwards, the main parameters that affect this kind of CFD calculation will be investigated. The analysis will start with the simulation input parameters, trying to give an overview on the computational mesh generation and the physical models.
The aim is to underline a methodology, which could allow setting up more reliable simulations, thanks to a deeper understanding of the involved physics and numerics.
The last part of this chapter will focus on methodologies to link the internal nozzle flow to the spray simulation.

4.1. Physical background

The internal nozzle flow and the occurrence of cavitation are strictly related to the physical properties of the injected fluid. A short description of the concurring fuel phases is therefore held, followed by the definition of the adopted cavitation model.

4.1.1. Thermodynamics of Phases

A set of preliminary assumptions has to be defined in order to reduce the complexity of the physical phenomena. The cavitating flow is simulated as a two phase flow with a continuous phase (fuel liquid) and a dispersed one (fuel vapour). The incompressibility hypothesis is then assumed, so that densities ρ_l and ρ_v are constant for each phase. In the following analysis the considered fuel is n-Dodecane ($C_{12}H_{26}$). Vapour is treated as a perfect gas and it exists only under vaporization (or saturation) pressure p_{vap}.

$$\rho_v = \frac{1}{R_m T} p \quad , \quad \forall p, p < p_{vap} \tag{4.1.1}$$

The vaporization pressure is a function of temperature T, and for n-Dodecane it varies by nearly six orders of magnitude between 270 K and 658 K (critical temperature), exactly from 1.23 Pa to 1.813e^{+6} Pa (see Fig. 4.1). This implies that it is difficult to define an initial value for vapour density, as it appears to be very sensible to the flow temperature inside the nozzle.

For the fuel a temperature around 300 K is usually assumed, but heat transfer into the nozzle could easily affect the vapour formation.
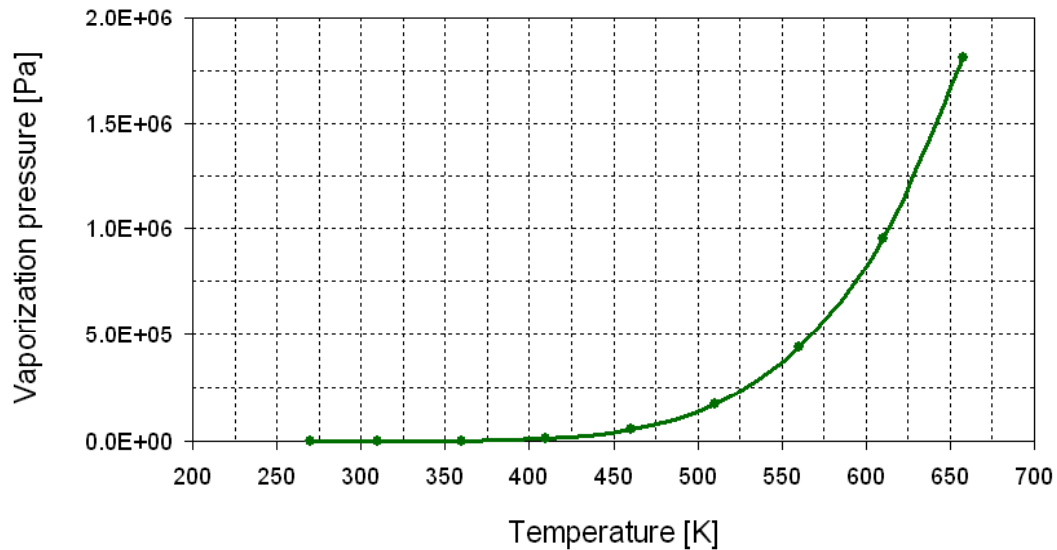
Figure 4.1: Vaporization pressure as a function of temperature for n-Dodecane.

Another assumption is that the temperature T is constant inside the nozzle, which means that no energy equation is calculated by the CFD solver. This hypothesis allows creating linear curves which correlate fuel density to pressure, as shown Figure 4.2, left. Each curve defines the physically acceptable fuel density range for variable load pressures and defined temperature. These curves change maximum density value and slope $k=M/(R_mT)$ according to temperature T, as shown in the right hand side of Figure 4.2.
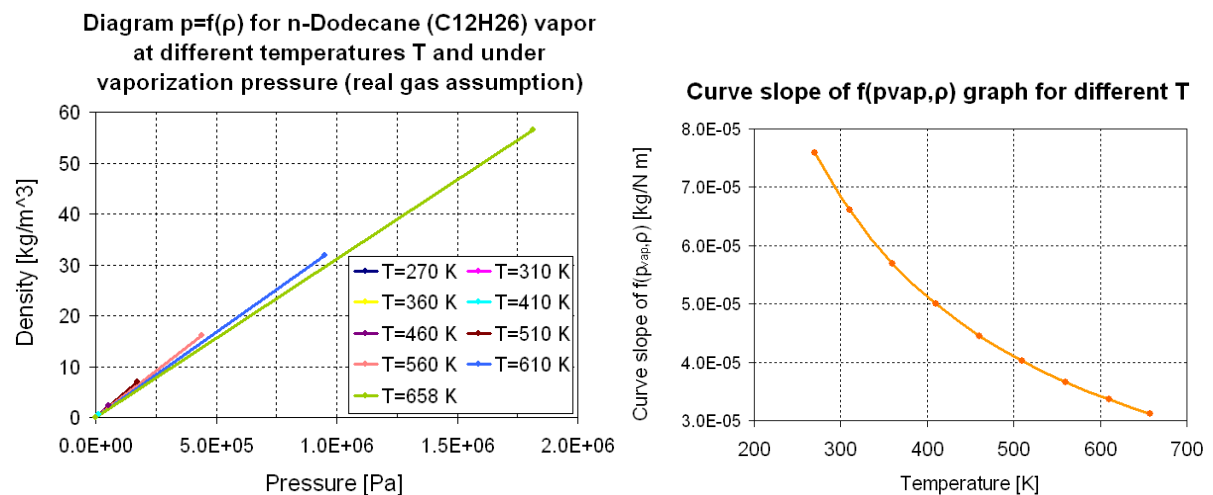
Figure 4.2: Vapour density dependence on pressure and temperature.

The maximum density of gaseous phase changes rapidly according to temperature, as can be seen in the logarithmic graph in Figure 4.3. For this reason it is difficult to identify the initial density value of vapour phase; moreover, it plays a determinant role in the multiphase CFD calculation, as for an incompressible flow it will be constant during all further simulations. The vapour density should therefore be chosen under the maximum value allowed by the surrounding temperature, considering as physical limit the graph in Figure 4.3.
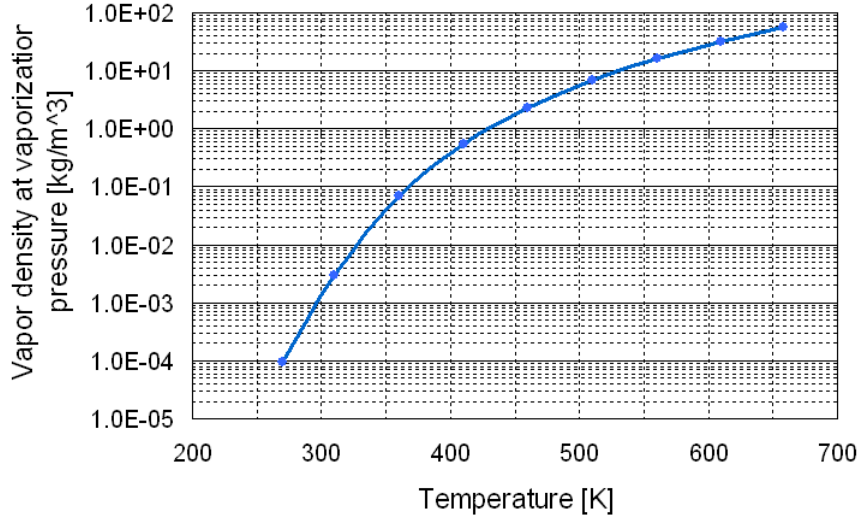
Figure 4.3: Vapour density in function of temperature for n-Dodecane.

4.1.2. Cavitation model

The multiphase solver for the nozzle flow simulation requires the definition of two interacting phases, namely the fuel in its liquid or gaseous state of aggregation. In the Fire v8 code the dispersed phase is modeled as a mixture of bubbles interacting with the fluid continuum by the exchange of mass and momentum source terms [7].
The basic concept of the cavitation model is that if the liquid flow undergoes the vaporization pressure new vapour bubbles are created in the computational cell. Vaporization pressure and vapour density mainly affect the mass exchange source term Γ_m between the phases, which is calculated by

$$\Gamma_m = \frac{3.85}{C_{CR}} sign(\Delta p) \frac{\rho_v}{\sqrt{\rho_l}} N_b^{\frac{1}{2}} \alpha_v^{\frac{2}{3}} |\Delta p|^{\frac{1}{2}}$$ (4.1.2)

where α_v denotes the volume fraction of the vapour phase, ρ_l and ρ_v are the liquid and vapour phase densities, N_b represents the bubbles number density and $\Delta p = p_{vap} - p$ is the effective pressure neglecting turbulent fluctuations. This relation could be written as:

$$\Gamma_m = C\ sign(p_{vap} - p)\rho_v |p_{vap} - p|^{\frac{1}{2}}$$ (4.1.3)

According to the previous assumptions (i.e. in Figure 4.3), if temperature increases, consequently also vapour density and vaporization pressure exponentially increases, leading to fast increasing cavitation source terms. Considering that vapour exists only under p_{vap}, it is possible to define a domain where the mass exchange source terms at a defined temperature T' are positive (see Figure 4.4).
In conclusion, the choice of liquid temperature strongly affects the cavitation phenomena. Aware of this fact, the simulations will be performed with a temperature of 293.15 K, with a corresponding vapour density of 0.1 kg/m^3 and vaporization pressure equal to 150 Pa. Momentum source terms for drag are then modeled according to round gas bubbles transported by the liquid flow [7].
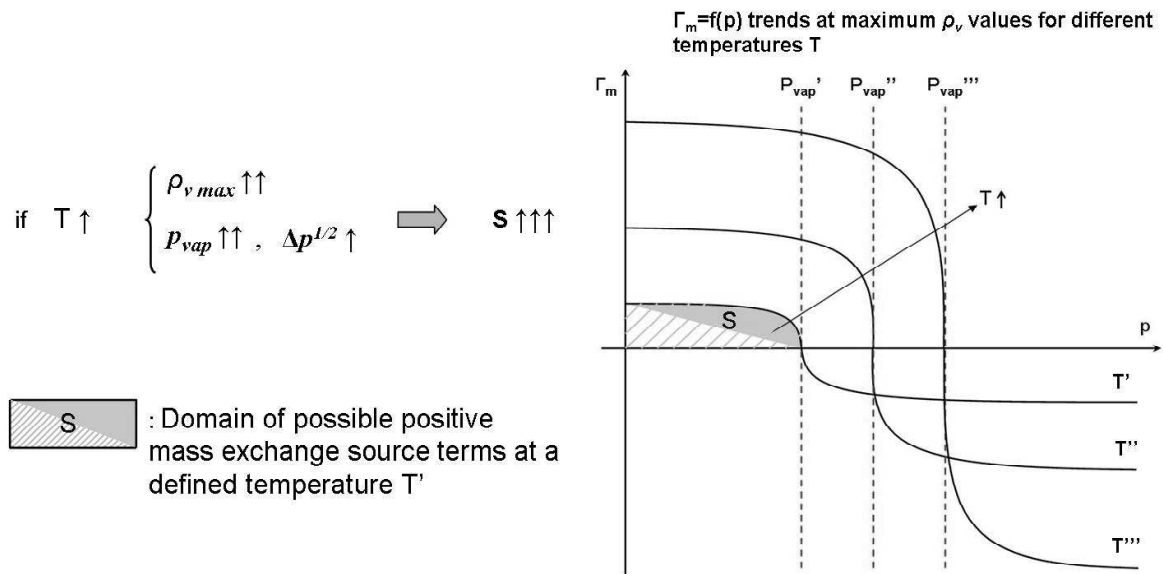
Figure 4.4: Trends of the maximum cavitation mass source term at different temperatures.

4.2. CFD Application

In order to perform a simulation of the injector internal flow many requirements have to be fulfilled. The generation of a computational mesh, the definition of boundary conditions and the reproduction of needle movement are some aspects which need particular care and will be therefore described in the current section. Afterwards an example of simulation results and of the geometrical effects on them will be presented. All the calculations are performed with Fire v8 multiphase solver.

4.2.1. Computational Mesh

The nozzle geometry usually presents a periodic holes distribution: this allows the generation of a sector mesh, assuming radial symmetry in the nozzle body and a vertical symmetry in the nozzle hole. In a 6-hole nozzle only a 30° sector mesh needs to be generated, due to the symmetry boundary condition on the lateral surfaces.
The general requirements for a good mesh quality can be summarized into the following points:

- The computational cells should be boundary connected and aligned to the flux.
- The mesh should be finer in proximity of critical zones for cavitation phenomena (i.e. near the needle closure site and the edge between injector body and nozzle).
- The aspect ratio should not overcome values of around 10.

The adopted meshing program is ICEM CFD; the meshes are generated with a top-down blocking process. At first a structure blocking is created in order to capture the geometry; with a top-down process the blocks are split and the unused ones are discarded. Later on the blocks are associated to the geometry through projections of edges on curves. The vertices and the surfaces are then moved onto the geometry. Mesh size is assigned through the definition of edge cells distributions and the generated mesh is then improved with the adoption of an O-

grid: a cells layer is created next to the solid surfaces. The nozzle meshes created with ICEM CFD appear fully boundary connected and aligned to the flux (see Figure 4.5). With these kind of computational grids it is possible to assure a solid base for further CFD simulations.

(a)   (b)
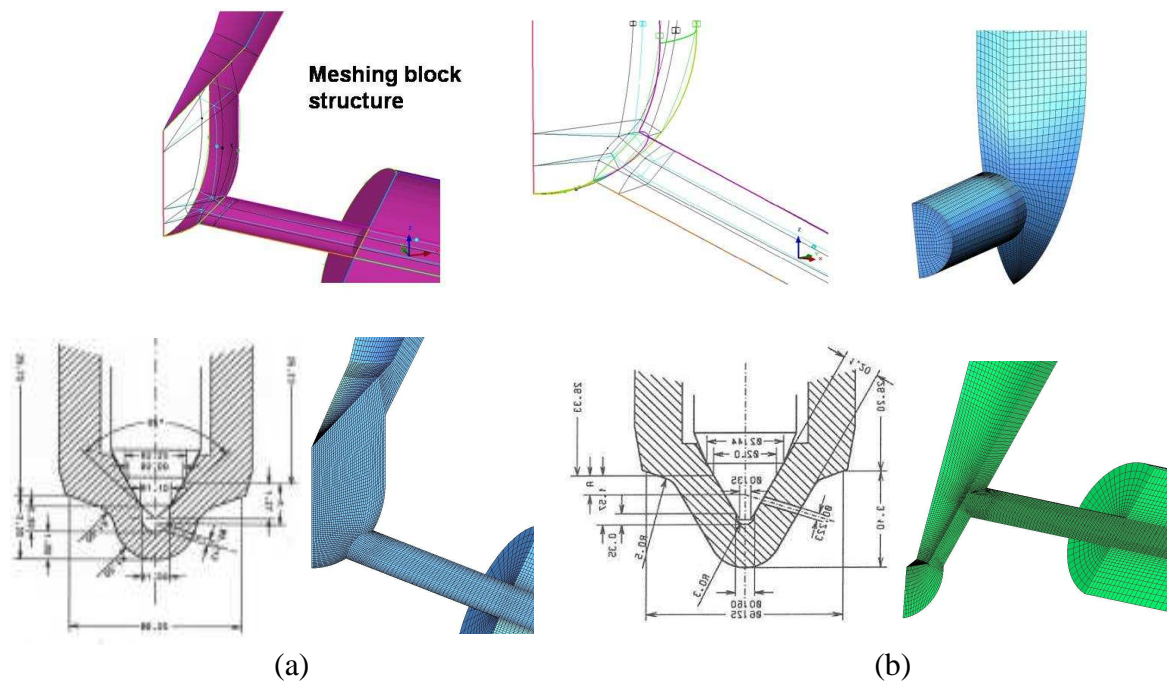
Figure 4.5: Mesh generation and topology for Sac Hole (a) and VCO (b) Nozzles.

4.2.2. Boundary conditions

The main boundary conditions are represented by the pressure inlet, corresponding to the rail pressure, the symmetry faces, the moving needle and the outlet, which should reflect the pressure value of the injection chamber (see Figure 4.6). The last two aspects are particularly important for the quality of the simulation results and will be therefore analyzed separately.
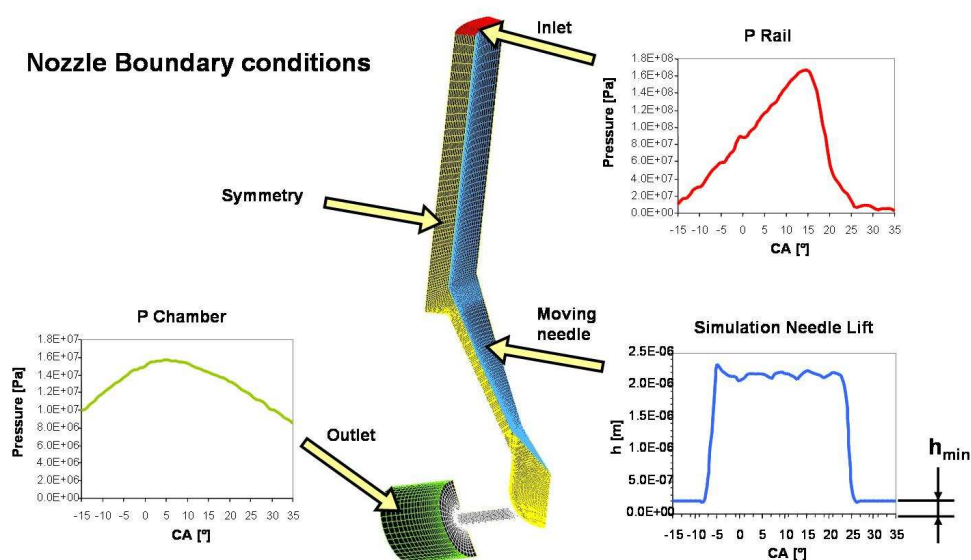
Figure 4.6: Boundary selections for the nozzle flow simulation.

• **Outlet boundary**

The outlet selection should assure the injection chamber conditions in terms of static pressure. In the case of a super-cavitating nozzle, i.e. with vapour phase reaching the nozzle outlet, a boundary condition could strongly affect the flow field. That is why it is better to define a volume just outside the nozzle hole, where the chamber conditions are recreated without affecting the outlet layer and the cavitation shape (see Figure 4.7). Of coarse this operation needs the definition of a third air phase in the simulation and an increase in the number of mesh cells. The computational time will definitely increase, nevertheless together with the accuracy of results.
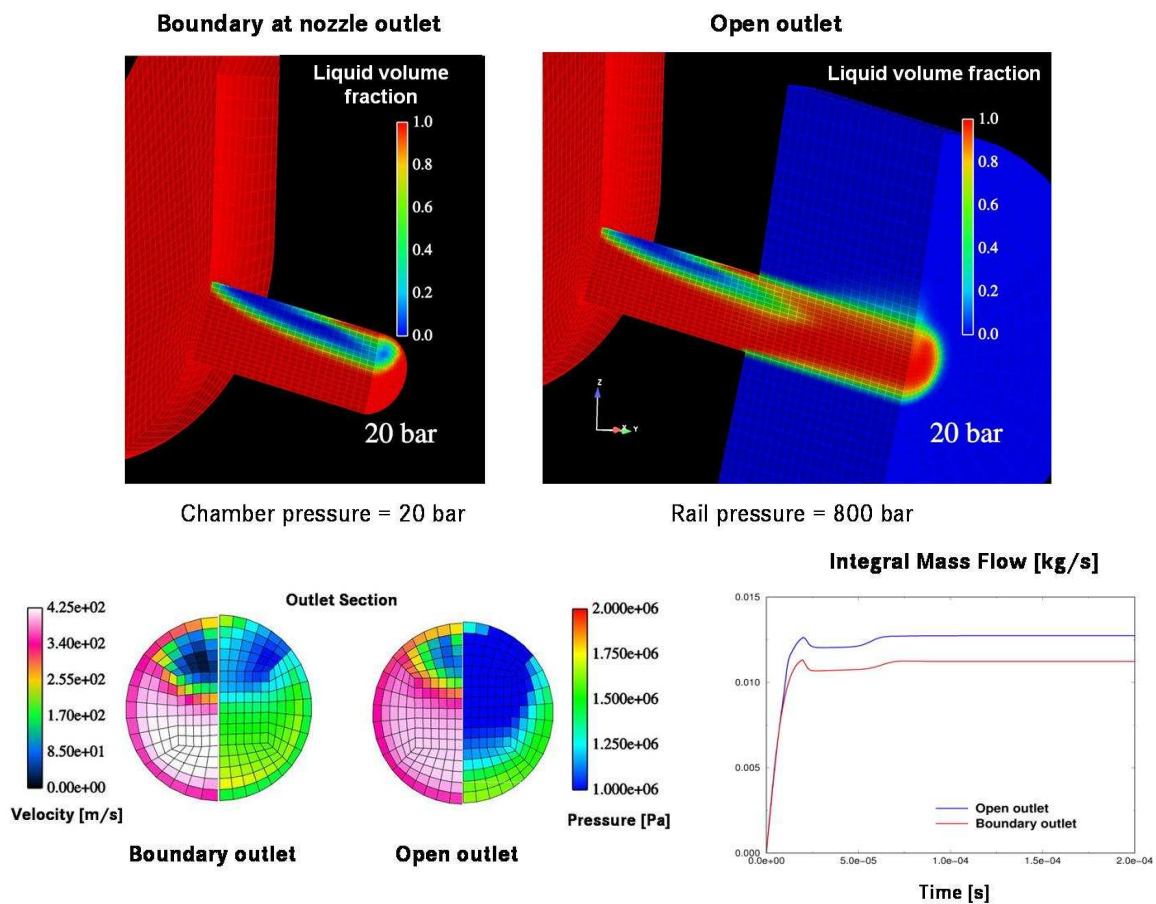
Figure 4.7: Effects of nozzle outlet boundary of flow and cavitation.

The effects of boundary selection directly at nozzle hole outlet or in an appended cylindrical chamber are consistent, as it is possible to see in Figure 4.7, where the cavitation region and the flow velocities appear strongly different for both cases. For this reason further meshes will be always created with a chamber volume outside the nozzle geometrical outlet.

• **Mesh movement**

The nozzle flow is a clear dynamic phenomenon, which is directly linked to the needle lift curve (i.e. in Figure 4.8). The most critical points for a simulation are the opening and the closing phases, when the movement of the needle surface induces strong changes in the mesh structure. Of course the completely closed nozzle is not possible to achieve, as the contact between the two surfaces would induce the cells to collapse into void volumes. A reasonable

value for the minimum lift h_{min} is at least 10% of the maximum value h_{max}. Considering that the needle lift could reach around 250 μm in trucks applications values, it is not possible to maintain the same number of cells at a minimum lift of i.e. 20 μm. Furthermore, the boundary displacement leads to unacceptable deformations of the cell layer beneath the needle: as shown in Figure 4.8 right, the mesh quality region A is definitely poor.
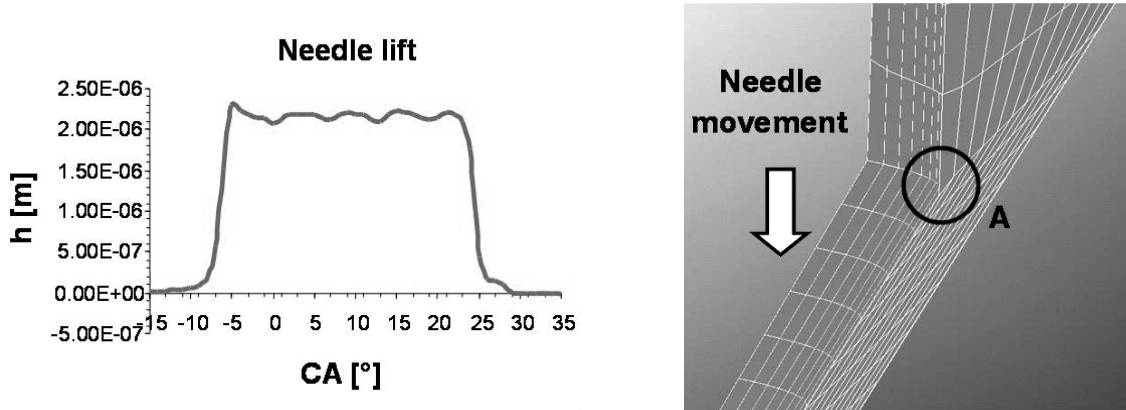
Figure 4.8: Needle lift movement trace and mesh deformation.

In order to avoid a deterioration of computational quality, new meshes need to be introduced by means of subsequent mapping procedures.
Another way to consider the mesh movement is to perform a linear interpolation between two meshes with the same number of cells. The node coordinates are interpolated in time between start and final position according to a chosen curve. Besides, quality criteria for a moving mesh needs to be defined, in order to assure the mesh quality also during the movement run (see figure 4.9 for symbols definition). These criterium are on cell deformation angle, aspect ratio and wall effects, as defined in the following sections.

- Angle criterion

The assumption is that the absolute value of the cell deformation angle β should never be greater than the needle angle α, as shown in Figure 4.9.

$$|\beta| \leq \alpha \tag{4.2.1}$$

Defining a nozzle geometry factor K as

$$K = \frac{tg\alpha \ (1 + \sin\alpha)}{tg\alpha + \cos\alpha} \tag{4.2.2}$$

and with simple algebraic steps it is possible to define the intermediate needle lifts h^n, at which a new interpolation mesh is needed.

$$h^n = h_{max}(1 - K)^{n-1} \geq h_{min} \tag{4.2.3}$$

Starting from the maximal needle lift h_{max} it is therefore possible to extract the required number of cells.
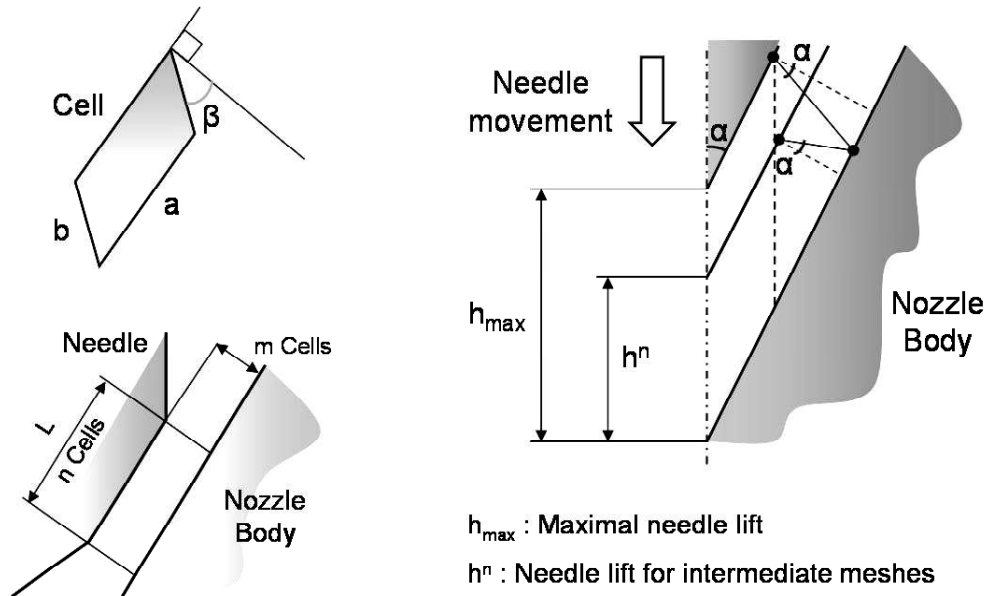
Figure 4.9: Needle movement and mesh effects.

- Aspect ratio criterion

The cell aspect ratios are defined as the fraction between the cell edges length. In order to avoid computational problems and too high numerical diffusion, a good practice is to contain this value under a certain rate.

$$\frac{a}{b} \leq 10 \qquad (4.2.4)$$

It is therefore possible to calculate a number of cell layers in the hollow space between needle and nozzle body, in order to guarantee the desired aspect ratio.

$$m \leq 10 \; n \frac{h^n \sin \alpha}{L} \qquad (4.2.5)$$

- Wall effect criterion

Another good practice is to generate a wall layer that could ensure a reliable y_1+ value, usually between 30 and 100 should be outside the transition layer of the turbulence wall function. In this case the Δy_p value represents the cell edge length b in Figure 4.9.

$$y_1^+ = \frac{\Delta y_P}{\gamma} \sqrt{\frac{|\tau_W|}{\rho}} = \frac{h^n}{m} \frac{1}{\gamma} \sqrt{\frac{|\tau_W|}{\rho}} \qquad (4.2.6)$$

If the $y+$ range is not satisfied, the number of cells in the closing region needs to be enlarged in order to fit the turbulence models requirements.

4.2.3. Simulation results and industrial applications relevance

Some examples of simulation results are shown in Figure 4.10. The cavitation phenomenon usually occurs at the upper edge between nozzle sac and orifice, as the strong flux deviation with consequent flow detachment lead to a region of pressure drop. Also the lower edge could generate cavitation, mostly during the nozzle-opening phase. The presence of flow vortices due to the injector sac geometry [52] or the fluctuations of the rail load pressure are also some reasons of cavitation events.

The vapour bubbles are then transported along the hole until they reach regions where the pressure is greater than the liquid vaporization pressure. The injection in the combustion chamber leads to a pressure environment that locally precludes the presence of vapour phase. Nevertheless, the cavitation region could disappear or be reduced before the arrival to the orifice outlet by adopting different injector and hole geometries. For example in Figure 4.10 three different injectors lead to complete different cavitation shapes at the outflow section. The adoption of converging conical holes usually reduces the intensity of cavitation, as the static pressure along the orifice increases under the effect of the reducing flow section.

These asymmetries at the nozzle outlet definitely affect the subsequent spray formation process. This is of coarse the key-reason for the development of a coupling method between nozzle flow and spray simulation.
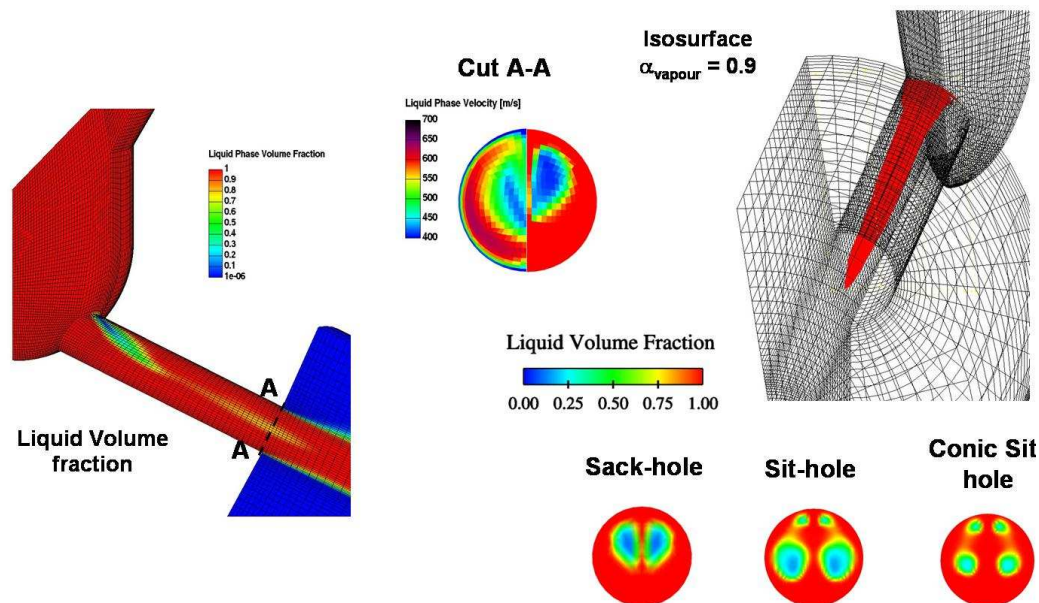
Figure 4.10: Example of simulation results in different nozzle geometries.

The nozzle flow simulation could also provide important results in the development of nozzle geometry. In many operative cases the mechanical parts of the injector could be subject to erosion and decay, leading to a bad performance of the whole system.

The cavitation bubbles implode as soon as the thermodynamical conditions do not allow the existence of vapour. This process is highly dangerous for the nozzle cavity, as seen in Figure 4.11 (a): if the cavitation region develops itself up to the nozzle exit, after a certain amount of engine cycles the orifice form appears highly corrupted. Also the interior of the nozzle hole appears damaged from the cavitation, as shown in figures (b) and (c). The 3D simulation results proposed in figure (d) shows the presence of vapour bubbles exactly at the outlet section of the nozzle orifice, showing a possible method to predict critical geometries with the previous adoption of computational models.
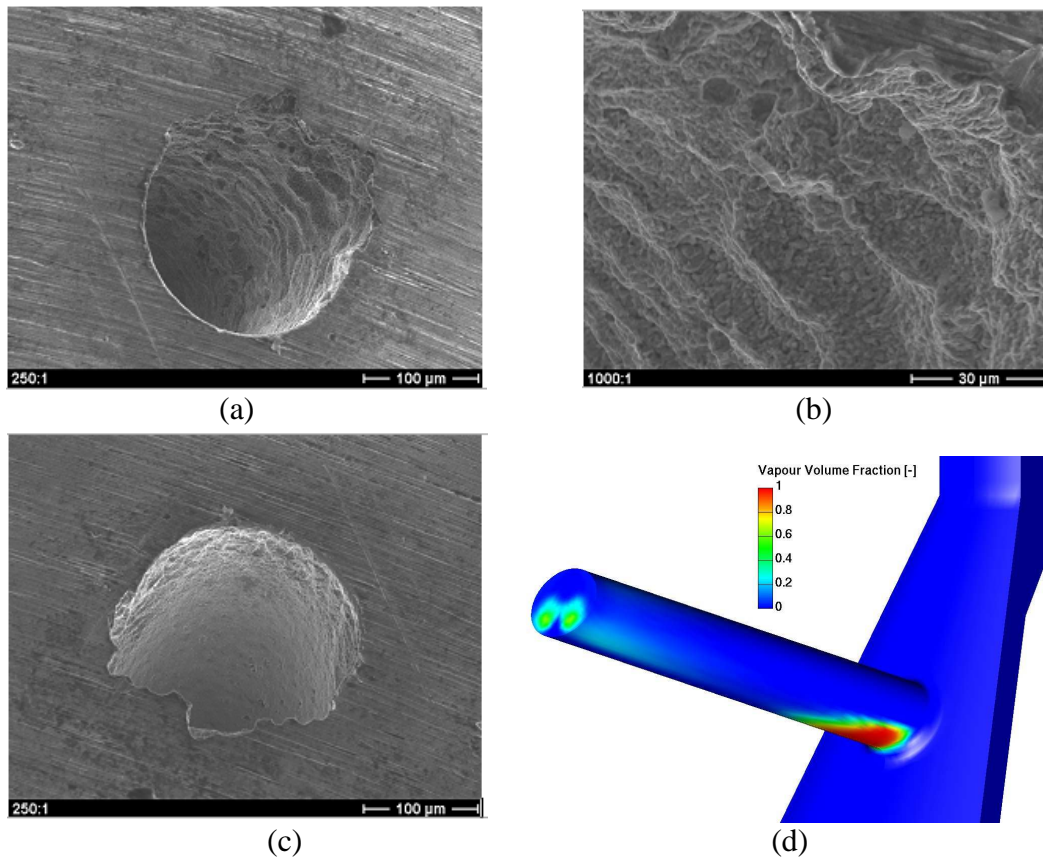
Figure 4.11: Experimental microscope images of nozzle outlet corrosion after 250.000 km due to cavitation (a and b with different magnification); reverse image (c) and simulation (d).

Another interesting aspect is the back flow inside the nozzle body after the end of injection. The presence of sulfur on the exhaust gases could lead to chemical reactions, which grind down the metal inside the injector cavity. This erosion process continues until the needle can no longer close and the nozzle operability is compromised. Through CFD simulation it is possible to reproduce the gas flow inside the injector after the valve closure, to define if the suction of gas could cause a transport of them up to the needle. For example in Figure 4.12 a swirl takes place inside the nozzle, leading to a continuous interaction of exhaust gases with the injector body: in this case the chemical corrosion could be assumed as probable, as stated also by experimental achievements.
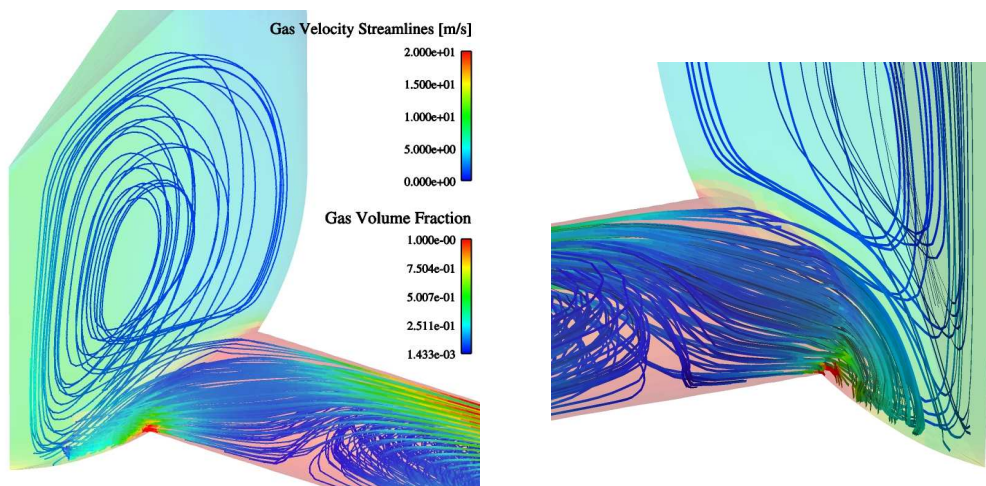
Figure 4.12: Gas back-flow inside the nozzle at needle closure.

4.3.   Coupling of Nozzle Flow to Spray

Spray properties and mixture formation strongly depend on nozzle flow characteristics. The presence of cavitation leads to asymmetrical spray in terms of shape and droplet size distribution. Primary break-up models could be therefore directly linked to liquid velocity as well as to turbulence level in the orifice. The idea is to link the multiphase nozzle flow to spray initialization, first with the ICAS model and a library concept, and afterwards with a direct mapping to the Eulerian 3D approach.

4.3.1. Database concept for 1D-ICAS Spray model

This part will describe the coupling of the diesel nozzle flow with the spray simulations. The aim is to obtain a tool, which is sensible for advanced injection strategies. The flow field values at nozzle outlet will be linked to the inlet boundary conditions of the ICAS multiphase spray model. The inhomogeneous flow inside the nozzle hole due to cavitation will be linked to the break up process of the flow entering the combustion chamber. The methodology will be applied to the injector of the BR4000 MTU Engine. Nozzle flow simulation will be performed with FIRE v8.3, while the adopted combustion code will be Star-CD v3.15, in which the ICAS model is already built in.

Spray will be simulated with the ICAS multiphase 1D model: the liquid phase is divided into a number n_{class} of droplets classes, each one with a characteristic velocity and diameter. The usual initialization is made through a droplets diameter distribution around a chosen SMR (Sauter Mean Diameter) value and an injection velocity equal for each class. Instead the anisotropy at nozzle outlet could lead to a velocity distribution like the one shown in figure 4.13.
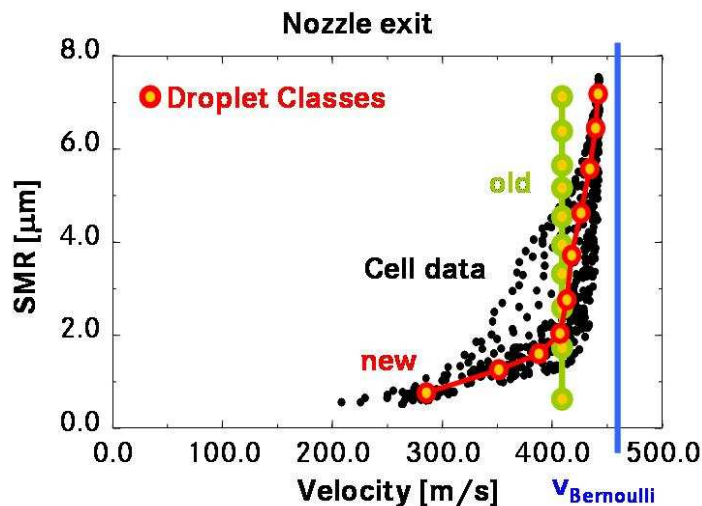
Figure 4.13: Velocities and diameters at nozzle outlet: connection to spray droplet classes.

Each class gets a different velocity and diameter according to turbulent and dynamic conditions at outlet cells, as described later. The idea is to perform in advance 3D nozzle flow simulations at different values of needle lift h_{lift} and rail pressure p_{rail} and to save the results on a matrix database. The main hypothesis is that the flow velocity inside the nozzle is much higher than the needle velocity, so that it could be assumed that the liquid stream interacts with a non-moving geometry. In this way the outlet conditions at injector orifice could be extracted from quasi-stationary simulations of the cavitating nozzle flow.

The sequence of operation is shown in Figure 4.14. One dimensional measurements or simulations provide p_{rail} and h_{lift} values for each crank angle; according to current simulation steps (i.e. points 1 to 5 in Figure 4.14) the initial conditions on droplets velocity $v_{droplets}$ and diameter $d_{droplets}$ are extracted and interpolated from the matrix database. The Eulerian spray boundary conditions will characterize at every time step the flow conditions out of the nozzle hole.
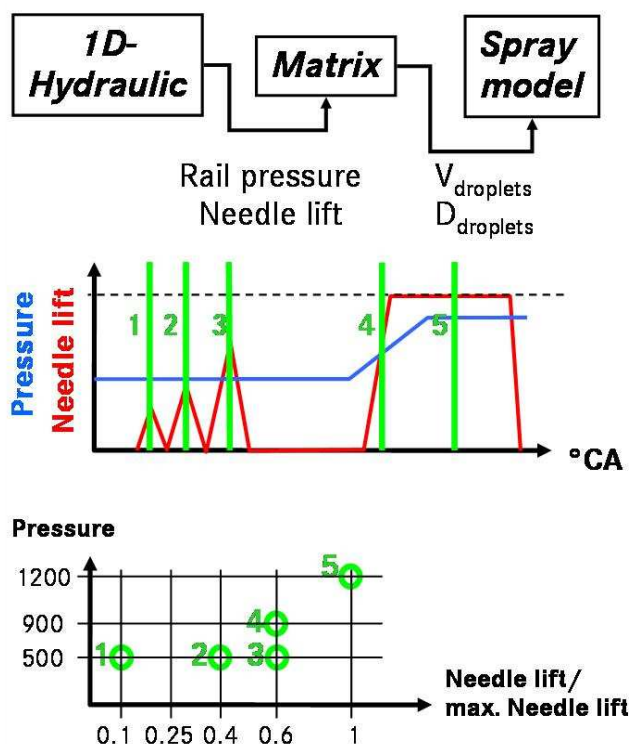

Figure 4.14: Concept of link between 1D and 3D simulations via Matrix.

Transient simulations will be then compared to stationary ones, in order to validate the reliability of the methodology. Afterwards 3D engine calculations with and without the database will be performed, with the purpose of detecting the influence of the coupling on mixture formation process.

- **Database creation**

The nozzle flow simulations are obtained with the FIRE multiphase solver. The number of chosen phases is three: fuel liquid, fuel vapour and air. The third phase is present everywhere, but only initialized to 1 in the cylindrical volume attached to the nozzle outlet (see Figure 4.15). The reason for this volume is that a pressure boundary just at the nozzle outlet forces the flow to be wrong and of unphysical behaviour.

Local values at nozzle outlet have subsequently to be extracted, in order to characterize the out-flowing stream: the most relevant dynamic and turbulent values could be identified to be the velocity v, the turbulent kinetic energy κ and the turbulent dissipation rate ε. The transition from nozzle flow to multiphase droplets is modelled with the primary break up assumptions defined in section 3.3.4. According to equation (3.3.45), the droplets dimension is taken proportional to the turbulent length scale l_t, with the constants C_1 and C_μ equal to 2 and 0.09. Each outlet cell determines a pair of (v,d) data, as shown in Figure 4.15. Therefore, for each time step a distribution of diameters and velocities is created from the nozzle orifice faces.
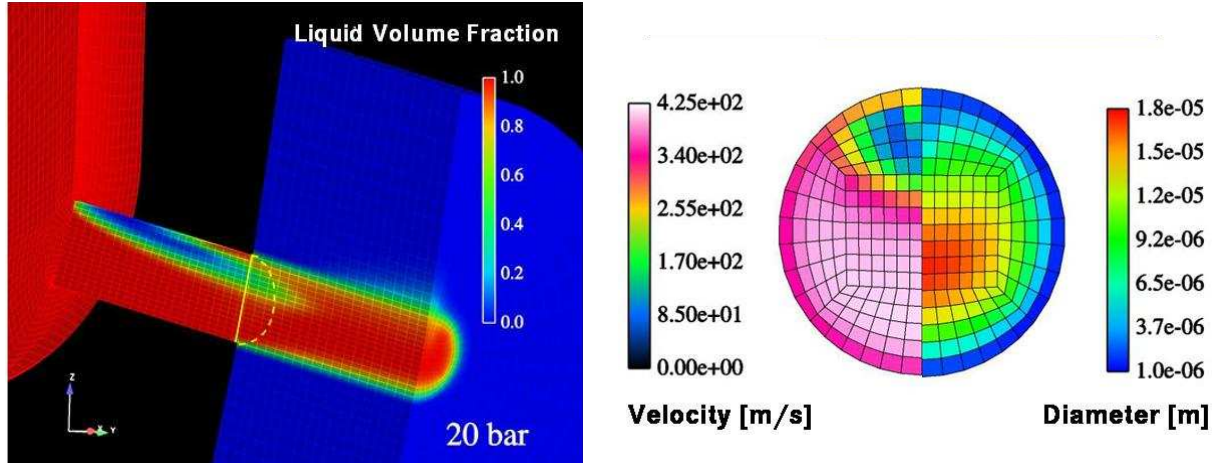
Figure 4.15: Nozzle flow simulations and outlet cells velocity and droplet diameters.

The nozzle outlet (v,d) cell values are then saved in an output file, in order to be post processed afterwards. The (v,d) distributions appear like the one in Figure 4.16. The ICAS multiphase spray model needs a number n_{class} of (v_k,d_k) values for each droplet class k, with $k=\{1,\ldots, n_{class}\}$; these points are obtained through a mass averaging procedure on the (v,d) distributions, as shown in the next paragraph. Finally the (v_k,d_k) ICAS input parameters will be saved in the database.
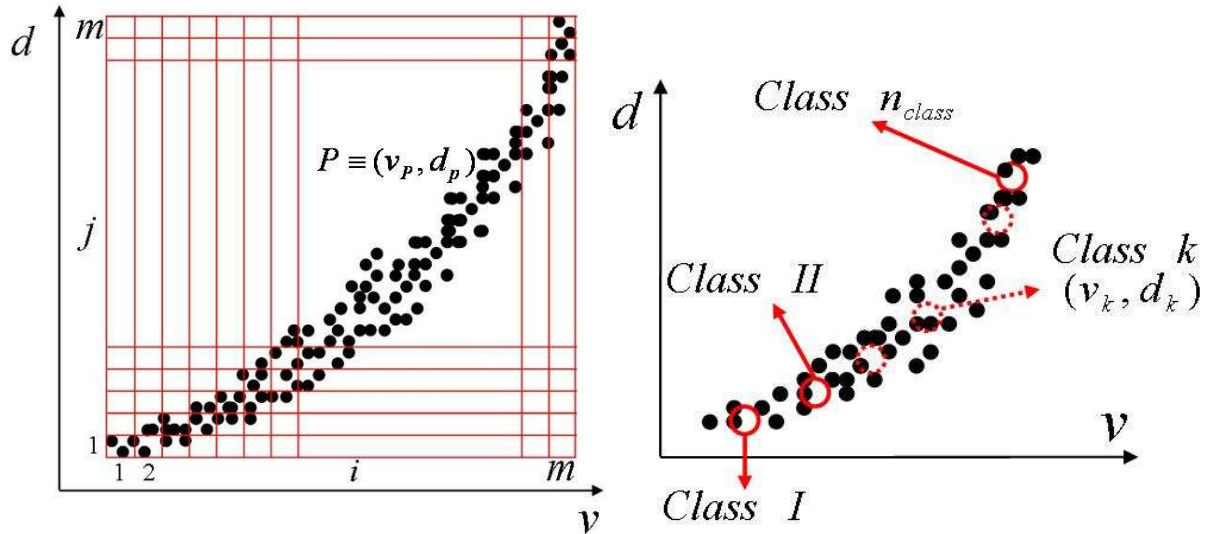
Figure 4.16: Velocity and diameter values at nozzle outlet cells (l.) and ICAS classes averaging procedure (r.).

The main assumption of the averaging procedure on (v,d) points is that each ICAS class has the same mass flow. Firstly a discretization procedure on outlet points P should be performed. An mxm sub-grid (i,j) is created in order to bound the diagram points (see figure 4.16). Afterwards a mass flow value is calculated in each (i,j) cell, according to the amount p of points P present in the corresponding box, which are defined by a local index l.

$$\dot{m}_{i,j} = \sum_{l=1}^{p} \dot{m}_{P,l} \ , for \ \ \forall P \in (i,j) \ \ with \ \ \dot{m}_{P,l} = \rho \, v_{P,l} \, \pi \, d_{P,l} \qquad (4.3.1)$$

Then the total mass flow of outlet cells is calculated and, depending on the amount n of ICAS droplets classes, each class k will be calculated according to a fraction $1/n$ of the total mass flow.

$$\dot{m}_{TOT} = \sum_{i,j=1}^{m} \dot{m}_{i,j} \qquad (4.3.2)$$

$$\dot{m}_k = \frac{\dot{m}_{TOT}}{n} \qquad (4.3.3)$$

A summation should then be performed: the chosen method is to sweep the 2D domain along the horizontal axis and mark the cells in order to convey the mass flow $\dot{m}_k$ value into each class. This method is carried out as follows: starting from the cell ($1,1$), the mass flow $\dot{m}_{1,1}$ is assigned to the first class and the cell is marked; then the cell ($1,2$) is analysed, the corresponding mass flow value $\dot{m}_{1,2}$ is summed into the class 1 and again the cell is marked. This procedure continues along the grid lines, until the stored $\dot{m}$ overcomes the target value $\dot{m}_k$. After this the integration goes on for the following droplet class, until the total mass flow $\dot{m}_{TOT}$ is covered. Every time that the swapping procedure reaches the end of a line j, the integration starts again from the cell ($1,j+1$). The method could be summarized in the following mathematical way:

$$if \quad \sum_{j=1}^{t^I} \sum_{i=1}^{s^I} \dot{m}_{i,j} \leq \dot{m}_k \Rightarrow marked \quad cells \quad in \quad class \quad 1$$

$$\sum_{j=t^I}^{t^{II}} \sum_{i=s^I}^{s^{II}} \dot{m}_{i,j} \leq 2 \; \dot{m}_k \Rightarrow marked \quad cells \quad in \quad class \quad 2$$

$$\quad (4.3.4)$$

$$\ldots$$

$$\sum_{j=t^{N-1}}^{t^N} \sum_{i=s^{N-1}}^{s^N} \dot{m}_{i,j} \leq n_{class} \; \dot{m}_k \Rightarrow marked \quad cells \quad in \quad class \quad n_{class}$$

At the end of the summation each cell of the domain and the corresponding points P are assigned to a defined class k. In other words, an amount q_k of the starting points P is assigned to each droplets class k. The final values of (v_k,d_k) are then obtained through an averaging procedure based on the cumulative mass flow of each spray phase k.

$$v_k = \frac{\sum_{l=1}^{q_k} \dot{m}_{P,l} \; v_{P,l}}{\sum_{l=1}^{q_k} \dot{m}_{P,l}} \quad , \quad d_k = \frac{\sum_{l=1}^{q_k} \dot{m}_{P,l} \; d_{P,l}}{\sum_{l=1}^{q_k} \dot{m}_{P,l}} \qquad for \quad \forall P \in k \qquad (4.3.5)$$

These (v_k,d_k) points are then saved in the library, so that they could be extracted during the CFD simulations. The described procedure releases spray initialization for a defined injector

operating condition: in order to be adopted in an engine simulation, the database has to cover a realistic range of needle lift h and rail pressure p values; afterwards, an interpolation procedure will be carried on. The overall process is shown in Figure 4.17.

During the CFD calculation the actual values of h and p are read from an input file, directly coming from 1D simulation or measurements. The database is then called in order to extract the (v_k,d_k) distribution. A bilinear interpolation at the current h and p values is carried out using the nearest maximum and minimum values h_0 and h_1 for needle lift and p_0 and p_1 for rail pressure. Finally the ICAS model inputs parameters v_k and d_k are ready to be transferred to the spray boundary conditions.
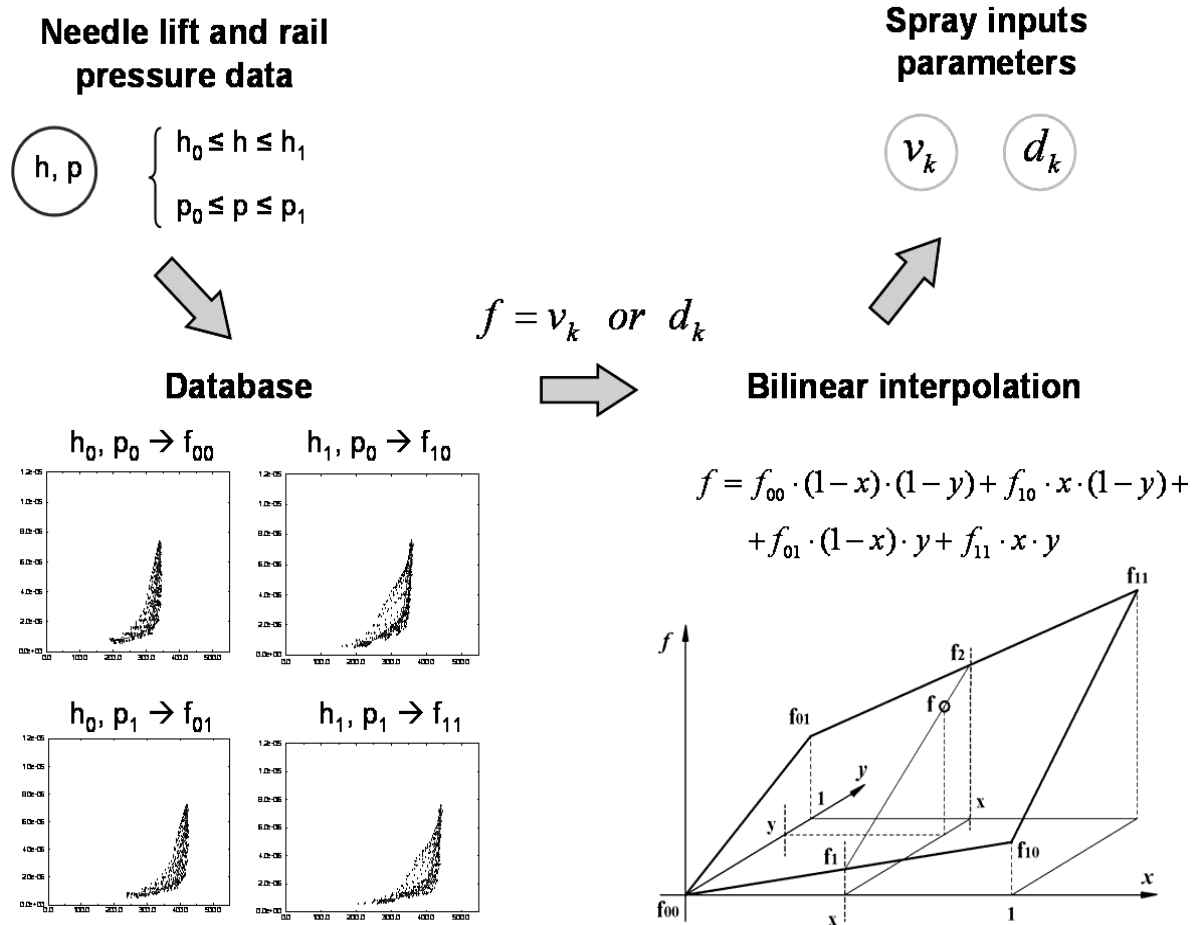
Figure 4.17: Overall process of link between database and CFD simulation

• **Application to a real motor**

In this section the creation of a library will be exemplified, showing the results on (v_k,d_k) distributions for different needle lift and rail pressure. The $(v_k,d_k)=f(h,p)$ database will be created for the BR4000 engine from MTU, whose specifications are shown in Figure 4.18. This model of diesel engine is in different heavy-duty applications, i.e. commercial vessels and yachts, naval and governmental vessels, rail vehicles, electric power generation, construction equipment and mining, industrial applications, agricultural machines.

Engine model		4000			
No. of cylinders		8V	12V	16V	20V
Cylinder arrangement		90°V			
Bore/stroke	mm	165/190			165/210
Max. output	kW	1100	2040	2720	3010
Max. speed	rpm	1860	2100	2100	1800

Figure 4.18: BR4000 engine characteristics (from MTU internet site: http://www.mtu-friedrichshafen.com/).

Experimental results are available for the different load points: bp5, bp6 and bp7, whose corresponding needle lift and rail pressure traces are shown in Figure 4.19, together with the geometry of the mounted injector L'Orange.
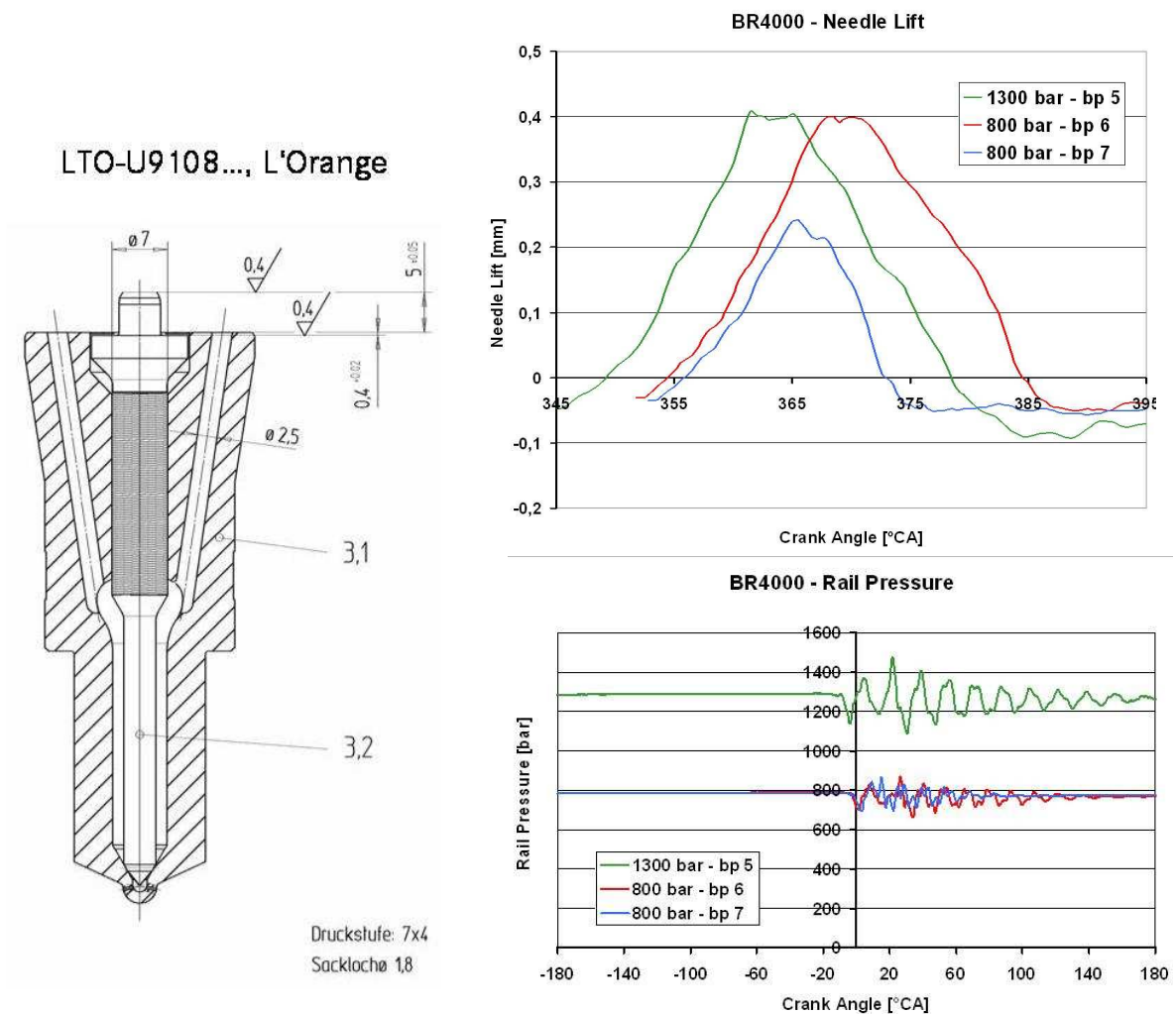
Figure 4.19: L'Orange injector: geometry and operative conditions (bp 5, 6, 7).

The library has to cover all the operation conditions of the BR4000 injector, in order to provide a reliable initialization of the spray. According to the experimental diagrams the range of rail pressures will be from 600 to 1500 bar and the needle lift from 50 to 400 µm.

Before proceeding with the generation of the library, a simulation with different mesh refinement is performed. The aim is to prove the reliability of the computational grid and prevent the use of a coarse mesh that could lead to low quality results. Two meshes are tested: a rough and a fine one, respectively with 137 and 572 cells at nozzle outlet. The simulations are made at 800 bar of rail pressure and 400 µm of needle lift. The results on outlet mass flow and droplets diameter are shown in Figure 4.20. It appears evident that the mesh refinement does not play a great role in this comparison: this means that the coarse grid is sufficiently detailed to get good simulations of the nozzle cavitating flow. The following calculations and the database creation will then be carried on with the rough mesh.
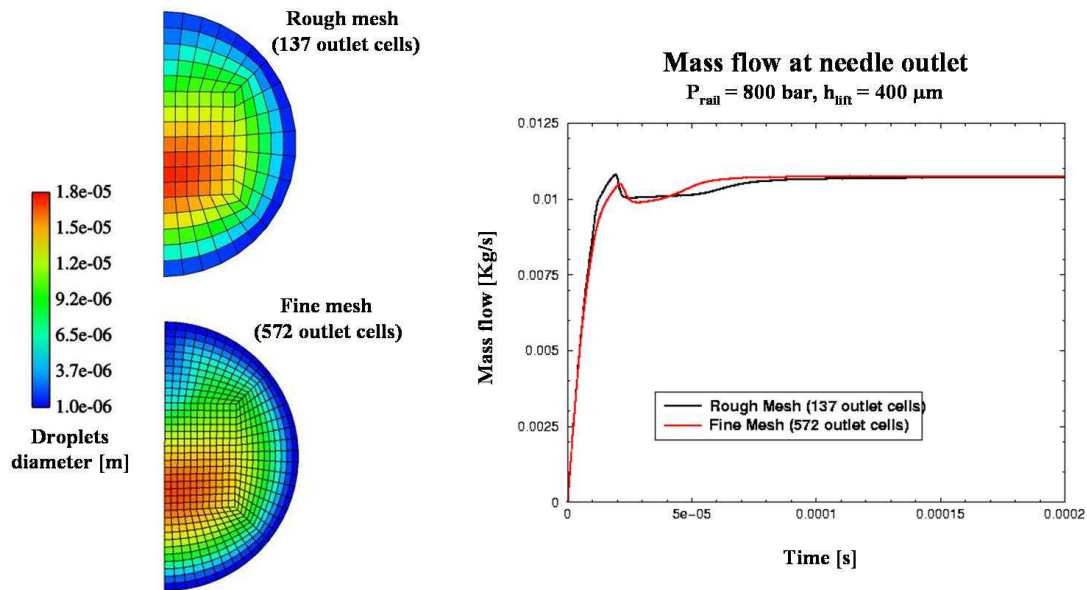
Figure 4.20: Mesh dependency on nozzle flow simulation.

Each nozzle flow simulation should characterize a specific (h,p) point in order to save the corresponding (v,d) couple. The idea is to perform for each chosen rail pressure a "stair" simulation: in other words a real opening $h=f(t)$ trace is followed, but the needle lift h is blocked at chosen values until a stationary state is reached (see Figure 4.21). Afterwards the (v,d) points are saved in an output file and the simulation runs on until the next database h value.

Rail Pressure [bar]	Needle Lift [µm]
600	50
800	100
1000	150
1300	200
1500	300
	400
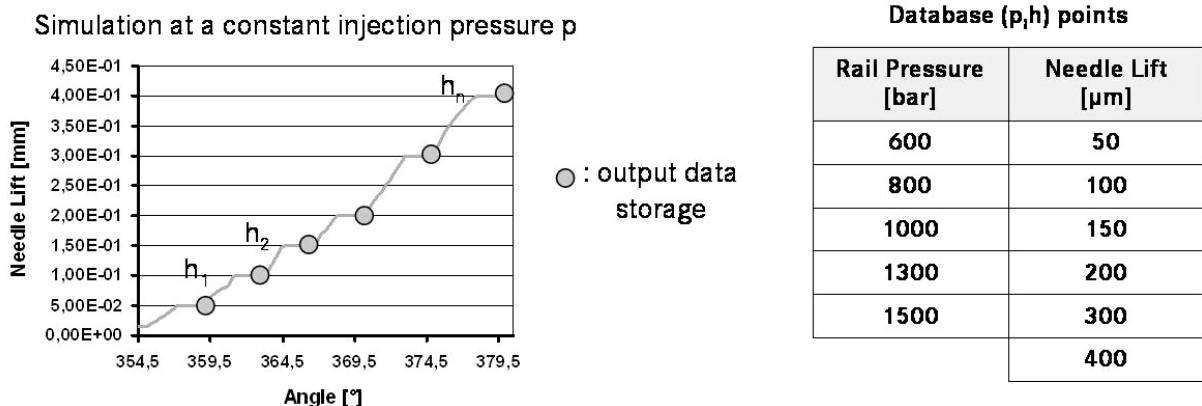
Figure 4.21: BR4000 injector: geometry and operative conditions (bp 5, 6, 7).

The coordinates *(p,h)* of the chosen database points are shown in Figure 4.21: this range could cover the totality of the previously illustrated working points. Simulations are performed with Fire v8.3 multiphase solver and lead to the storage of outlet *(v_k,d_k)* values for each *(p,h)* point. Afterwards the data is integrated and the overall library is obtained. The chosen number of ICAS classes is equal to 20, as it could provide a more detailed representation of the spray. A detailed graphical illustration of the library is shown in Appendix A. In order to obtain a more compact graphical representation of the library, the velocities were normalized on load pressure p_{inj}, as shown in Figure 4.22.
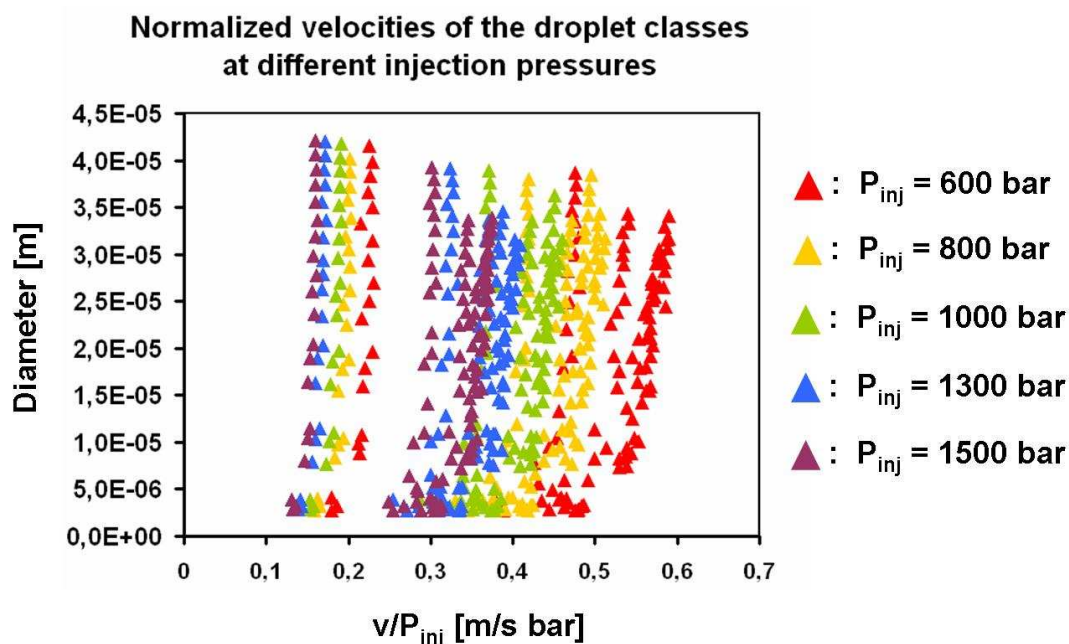
Figure 4.22: Pressure-normalized representation of the whole library data points for the BR4000 engine with L'Orange injector.

The diagrams show how the distributions tend to become very similar at bigger needle lifts, while there is a big jump in class velocities at the lowest values of *h*. However the *(v_k,d_k)* trends appear similar at different injection pressures.

As shown in the outlet section of Figure 4.20, the cells near the orifice wall are characterised by smaller velocities and diameters: this fact leads to the "half moon" shape of the *(v_k,d_k)* distributions. The gap on classes velocity appears stronger at higher injection pressures, as the flow field near the wall is more affected from the interaction with the solid boundary cells. Nevertheless, the y_I+ values are always between 30 and 100, assuring a good representation of the wall effects.

• **Comparison with transient simulation**

In this section a real transient simulation of the needle lift is carried out in order to compare the *(v_k,d_k)* distributions obtainable on stationary and transient calculation. The calculation is performed with the needle lift diagram of the BR4000 bp6 working point.

The transient simulation is made for the 800 bar rail pressure and the *(v_k,d_k)* distributions are saved both in the opening and closing runs. This allows testing the consistency of all work hypotheses, as defined in section 4.3.1. The overall results with the comparison diagrams are shown in Appendix A.
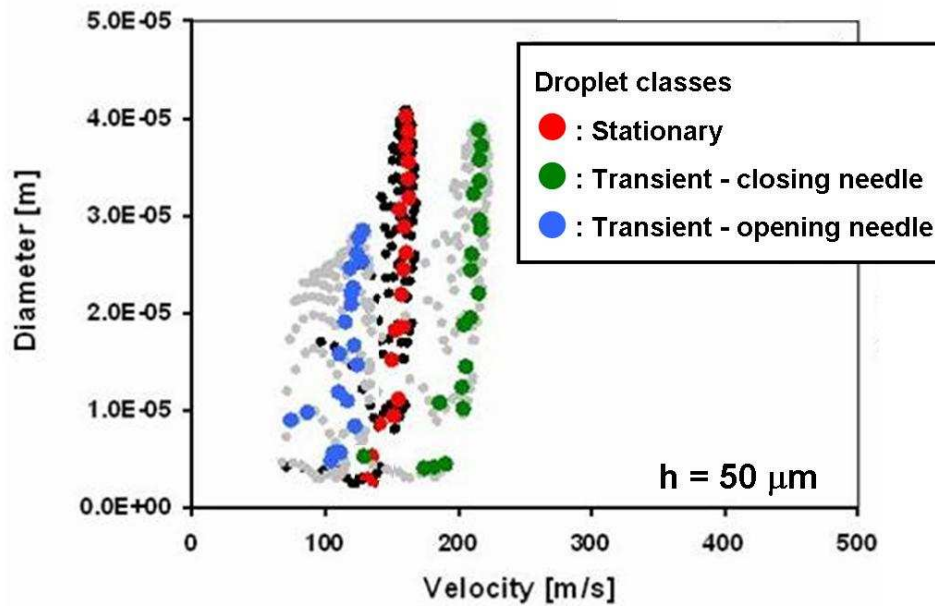
Figure 4.23: Comparison of the library data points between the nozzle opening and closing phase at *h*=50 µm and *p*=800 bar.

The transient and stationary simulations appear very similar for needle lifts bigger than 100 µm, but the distributions at *h*=50 µm are strongly affected from the history of the flow field, as shown in Figure 4.23: the opening needle simulation provides velocities and diameters smaller than the stationary calculation, vice versa for the closing one. These results are aligned with the preliminary assumptions, as at smaller *h* values the needle velocity is much closer to the flow one. An explanation could perhaps be found through an analysis of the local flow in the nozzle body, even if all the transient effects could be considered only by a direct coupling of the nozzle flow to the spray, as it will be shown in the following section 4.3.2.
In the considered test case the needle lift run appears very slow in each working point (see Figure 4.19) and this could strongly affect the spray initialization. Nevertheless the database methodology is developed to study the effects of modulation on rail pressure and needle lift diagrams, for example in the case of pre-, post- and pilot-injection strategies with increasing rail pressure: in this condition the nozzle flow library concept could provide a better basis for CFD spray initialization.

• **Engine simulation**

The engine simulations will be performed with the Star-CD v3.15 code, with the standard user routines of Daimler research group. The ICAS spray model is already built in and the combustion is described with the timescale PDF model. The adopted engine mesh is a 45° sector with adaptive grid in spray region. The operating conditions are taken from the load point 6, characterized by an engine speed of 1500 rpm, mean pressure of 20.8 bar, rail pressure of 800 bar and injected mass equal to 0,524 g/asp. The corresponding needle lift and rail pressure traces are shown in Figure 4.19.
The diameters of the spray classes are directly extracted from the previous calculated database, which is addressed as PMOD for the current injection system. The velocities need to be corrected in order to fit the experimental injection profile and the injected mass. The adjustment of droplets injection velocities is done according to the velocity v_{inj} calculated by the measured injection rate and the nozzle orifice area.

$$v_k^{\,c}(i) = v_k(i) \cdot \frac{v_{inj}}{\displaystyle\sum_{i=1}^{nclass} v_k(i) / n_{class}} \qquad (4.3.6)$$

The term n_{class} is the number of ICAS droplets classes and $v_k(i)$ defines the velocity of the class i extracted by the nozzle library. The corrected injection velocities $v_k^{\,c}(i)$ are the real input values for the ICAS spray classes, so that the total injected mass is preserved. In the standard simulations without the library the term v_{inj} represents exactly the velocity of each ICAS class.

The simulations are performed with the implemented correction factor for the injection velocities. The ICAS model in the standard case is initialized in droplets classes with equal velocities and diameter mean value of 15 µm, which is approximately equal to 1/10 of the nozzle diameter [44]. First of all the integral behaviour will be analysed according to the pressure traces, then the local flow values will be addressed through the distributions of temperature T and mixture fraction z_{mean}, which is here defined as the ratio between fuel (F) and oxidizer (O) in the considered cell.

$$z_{mean} = \frac{Y_F}{Y_O} \qquad (4.3.7)$$

A definition for more complex fuel/oxidizer systems could be found in [80]. Observing the pressure traces in Figure 4.24, the combustion process just after the top dead centre (TDC = 360 °CA) appears faster and stronger for the library-based simulation, as a higher pressure peak is reached. After 372 °CA both calculations show a weaker combustion process than reality, even if here the standard simulation provides higher values for in-cylinder pressure.
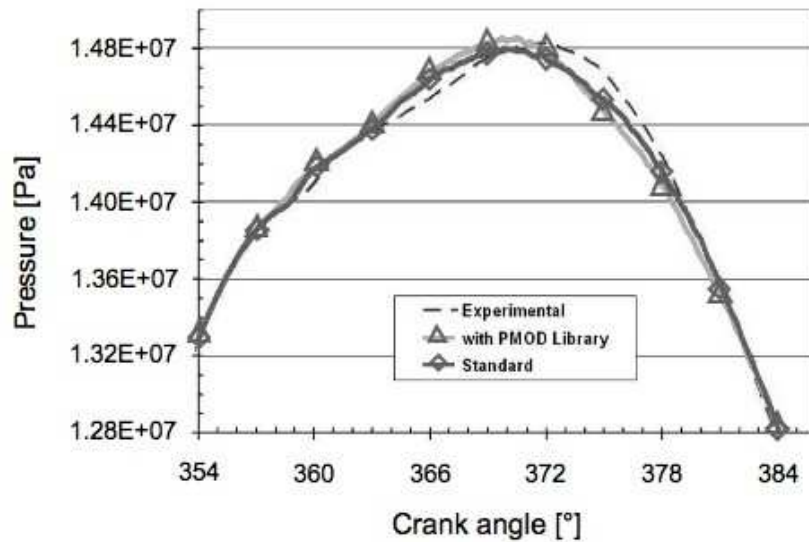
Figure 4.24: Pressure traces for the BR4000 bp6 case.

A reason for the different behaviours could be found in the local properties of the in-cylinder flow, as shown in Figure 4.25 and 4.26. For example, at about CA=358° the values of temperature T and mixture fraction z_{mean} in the spray region appear strongly bigger in the library based calculation, leading therefore to an earlier ignition. This behaviour could be

linked to the different velocity initialization of the droplets classes, which could lead to dissimilar interaction with the surrounding gas phase and influence the evaporation process. Also the 3D temperature field appear a little different in both cases, for instance near the cylinder head, as only in the standard case a temperature of 2400 K is reached at the upper wall. In the picture about z_{mean} at CA=365° it is also possible to see that with the library the spray presents discontinuities near the injector: this could be due to the oscillations in input rail pressure, leading to variations in the input (v_k, d_k) distributions.
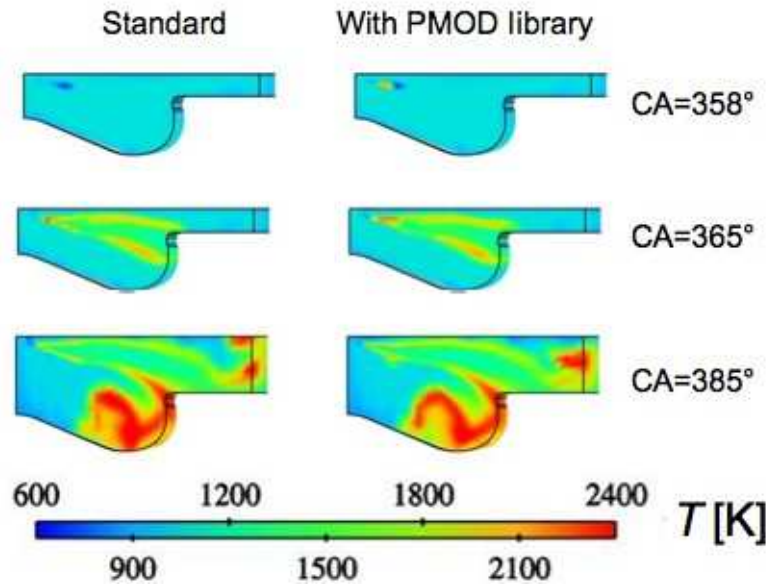
Figure 4.25: Temperature distributions for the BR4000 bp6 case.
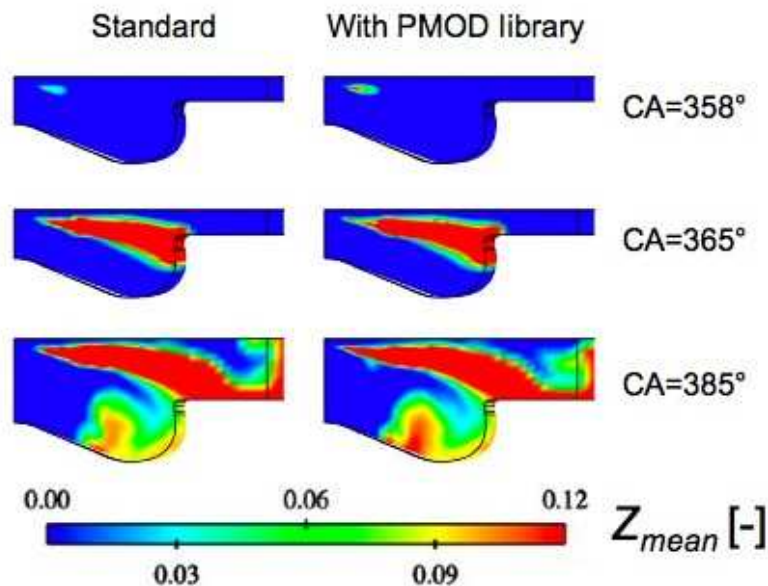
Figure 4.26: Mixture fraction distributions for the BR4000 bp6 case.

The total mass of fuel vapour in Figure 4.27 shows how the evaporation process runs unlikely in both cases: for the library simulation the n-Dodecane vapour is consumed faster in the pre-combustion phase, until circa 10°CA ATDC, then the standard calculation shows a stronger fuel consumption that is also confirmed by the higher pressure values after 372 °CA (see

Figure 4.24). The total injected fuel mass is equal in both simulations, as it is injected according to the input velocity profile: nevertheless the transition from liquid to gas phase is different, affecting therefore combustion and fuel consumption processes.
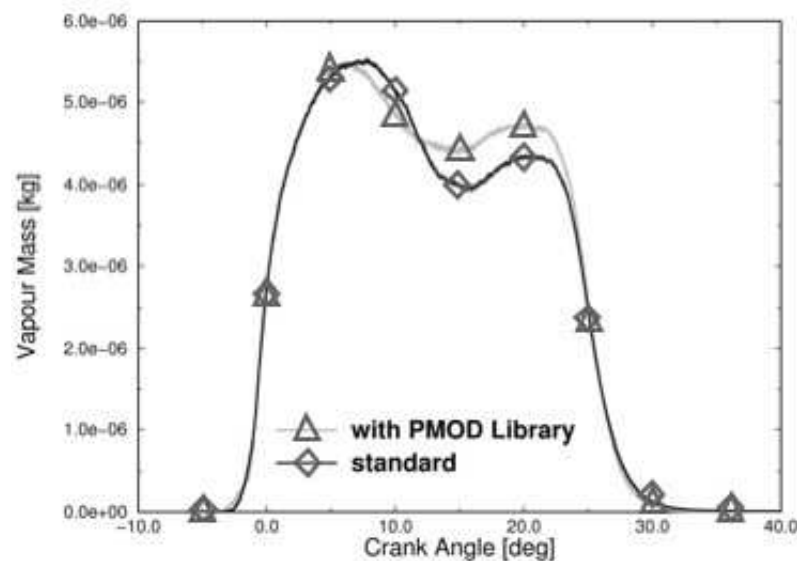
Figure 4.27: Evolution of in-cylinder fuel vapour mass for the BR4000 bp6 case.

- **Conclusions**

The library approach allows transferring important information from the nozzle flow to the spray. In the presented method the flow data from nozzle orifice are first conveyed into a library, whose matrix-structure is ruled by needle lift and rail pressure values. According to a predefined number of ICAS spray phases, the database data is processed afterwards to obtain the values of droplets diameter and velocity.

The testing of the database on a real engine case shows encouraging results in terms of pressure trace prediction. The combustion appears different between the standard case and the library one, due to the different evaporation behaviour of the injected droplets. Nevertheless the transient effects at the opening and closing needle run are difficult to be described by such an approach.

The database methodology could provide advantages if the rail pressure and the needle lift change during the engine run. For example with pre-, post- and pilot-injection strategies and increasing rail pressure the nozzle flow library concept would supply a transient initialization of spray droplets based on detailed nozzle flow simulations.

The presented work suggests that the methodology directly influences the spray behaviour and the consequent mixture formation process. The method could be then applied on further topologies of injector systems, leading to libraries for a chosen set of diesel engines.

4.3.2. Direct mapping to 3D-Euler Spray

In this approach a transient nozzle flow simulation is held and output data is written to a file with a predefined temporal resolution. Geometrical, temporal and flow data allow the mapping of nozzle orifice field to spray inlet, adopting a primary break-up model to initialize the Eulerian droplet phases. An example of the coupling method is shown in Figure 4.28, where the local velocity and TKE fields are mapped from the nozzle outlet to the spray.
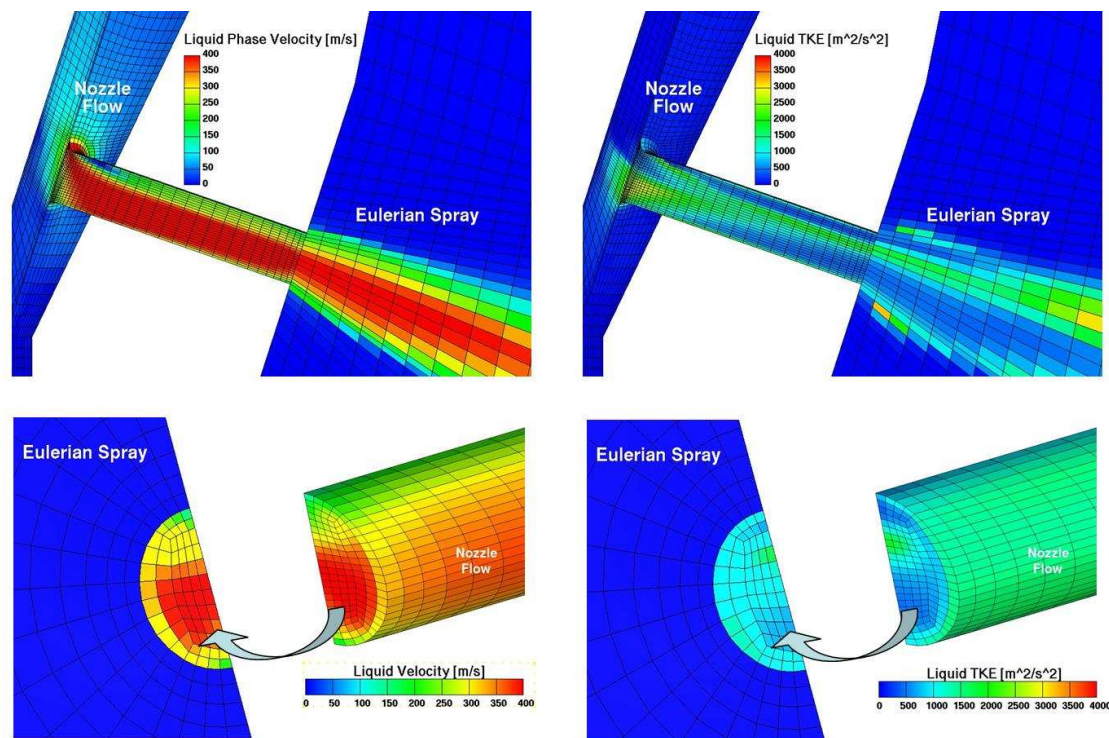
Figure 4.26: Nozzle flow mapping to 3D Eulerian spray.

This type of method can account for the local conditions at nozzle orifice during the transient injection process. It is therefore preferred to the stationary link to ICAS in terms of quality of results. Instabilities, asymmetries, turbulent and dynamics effects due to nozzle geometry and needle motion are locally transferred to the Eulerian spray, whose orifice resolved grid could lead to a better prediction of the complex phenomena involved in spray formation. Examples of the coupling are shown in Figures 4.29 and 4.30.
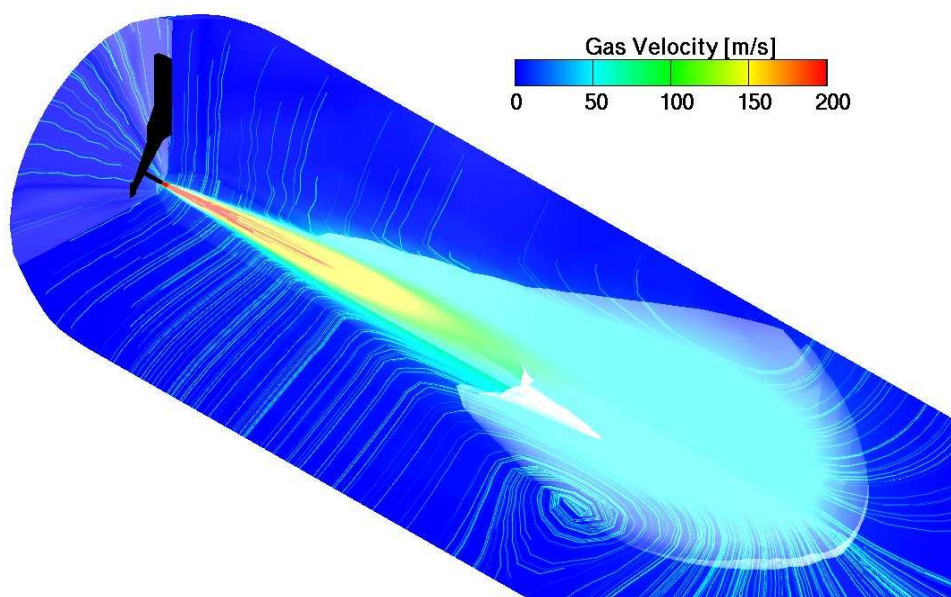
Figure 4.29: Eulerian spray coupled with nozzle flow simulation: contours of gas velocity and flow streamlines.

Nozzle

Isosurfaces (95%) of liquid and vapour phases

T = 985 K
p = 105 bar
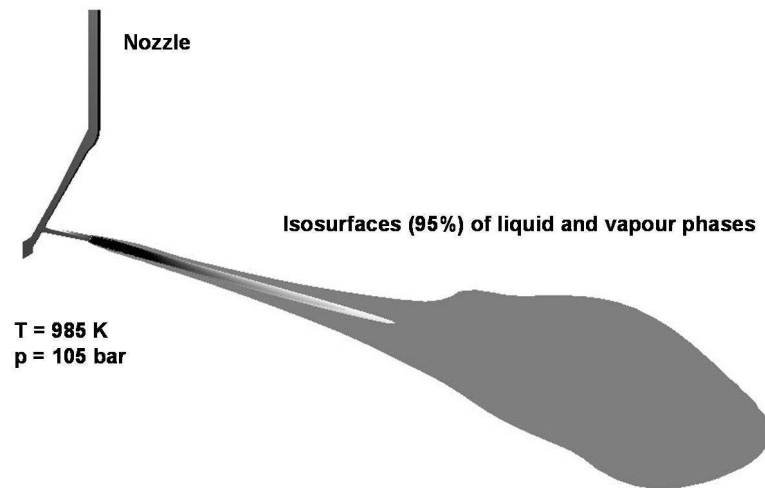
Figure 4.28: Example of evaporating Eulerian spray coupled with nozzle flow simulation: isosurfaces of liquid and vapour phases.

Even if the spray formation appears strongly affected by the previous nozzle flow, its simulation implicates more work and time consumption. On the other hand the accuracy of results could improve the prediction of mixture formation. An application of the procedure will be shown in chapter 6, where the spray on a real engine case will be directly coupled to the internal nozzle flow.

5. Code Coupling

5.1. Concept

In the previous chapter nozzle flow, spray and engine simulation principles were addressed. As mentioned, Eulerian spray models could provide better physical and statistical results in the dense spray region just outside the nozzle. Nevertheless, a single-phase solver with different species transport and chemical reactions libraries is sufficient to describe the in-cylinder combustion process. The basic idea of the presented coupling is thus to use both the Eulerian spray and the single-phase combustion solver in a synchronized simulation run. The conceptual workflow of the method is shown in Figure 5.1. The Eulerian spray model is used in the dense spray region (B) on a separate finer mesh, whereas the DDM approach is switched on in the thin spray/combustion region (C). Additional coupling to the nozzle flow simulation (A) could be then achieved, as explained in the next chapter.
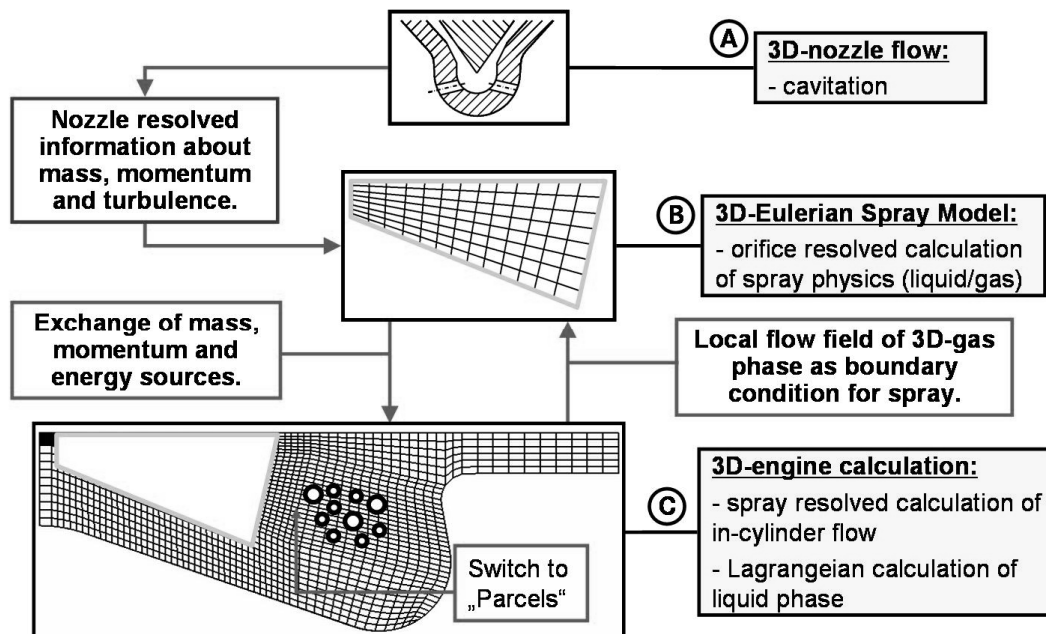
Figure 5.1: Coupling workflow.

The problem is that the gas phase in the engine solver needs to feel the interaction with the injected fuel, vice versa the Eulerian spray needs to get the evolution of the environment in combustion chamber: pressure, temperature and turbulence are directly affected by the piston movement, as well as by the occurrence of ignition and combustion processes. For this reason the thermodynamical conditions in both codes needs to be real-time interlinked and mirrored.

5.2.   Coupling interface

In order to couple the engine and spray domains, a data exchange procedure needs to be developed. In this case the AST Code Coupling Interface (ACCI), a Fire embedded tool which allows the transfer of data between two or more codes via TCP/IP protocols will be used. In this specific case the ACCI was modified in order to permit the connection with the external code StarCD v3.26 and the interaction between two fluid dynamics computational domains.

First, the basic concept of ACCI will be explained. As flow and sources data need to be redistributed from one mesh to another, the spatial mapping procedure will be clarified afterwards.

5.2.1. Data transfer

The ACCI interface executes two central tasks: the data exchange between an arbitrary number of simulation processes and the conversion of flow-field values between the different domains. The meshes used by the coupled codes need to overlap on a defined region and the information transfer is real-time completed. Field values and exchange spaces are respectively called attributes and interfaces. The description of which attributes need to be exchanged at defined interfaces is performed through an input file.

The exchange interface is implemented with a server-client model: a server program is responsible for data transfer between an arbitrary number of clients, where the simulation processes run. Communication is based on the TCP/IP-protocol, which allows a connection of more workstations in the same network. The procedure is schematically shown in Figure 5.2.
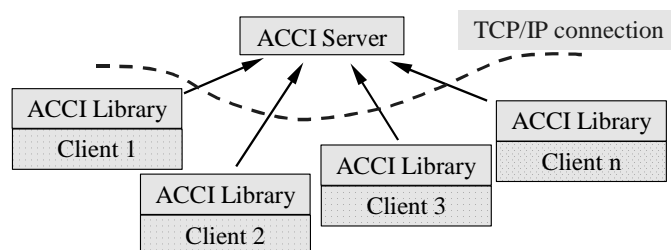
Figure 5.2: Coupling server-client interface model [8].

If MPI is running, each parallel sub-process is handled as a different client. The exchange is defined through "sets" and "gets" statements that identify which kind of attribute ("attribute_id") needs to be extracted or initialized on a defined interface ("interface_id") by a specific client ("client_id"). The general form of the input file is therefore defined as follows:

client_id set/get attribute_id at interface_id

The "gets" command is a request statement and "sets" a supply one: they equally imply that the client will wait until the exchange data is provided. The fluid dynamics attributes and meshes selection interfaces need to be addressed via user coding. If two interfaces have the same name, the ACCI automatically performs the mapping between both computational domains, both surfaces and volumes. For instance, calling pressure "p", velocity "v" and momentum sources "s_mom", a simple example of configuration file could be:

engine sets p at spray_boundary
engine sets v at spray_boundary
spray gets p at spray_boundary
spray gets v at spray_boundary
engine gets s_mom at spray_volume
spray sets s_mom at spray_volume

In this case the engine client will provide 3D pressure values, which will be mapped on the 2D spray boundary selection. Furthermore, the momentum sources generated in the spray mesh volume are mapped onto the three-dimensional engine domain.

Generally, attributes could have the form of scalars or vectors, as the interfaces could be one, two or three-dimensional. The mapping procedure between spaces with different dimensions and topologies will be described in the following section.

5.2.2. Spatial mapping

The Fire-ACCI mapping algorithm computes the intersection S_{ij} of volume or area or length (depending on the topological dimension of the cells) between the cells of two different meshes. A schematic view is shown in Figure 5.3, where two cells A and B are geometrically intersected: the terms S_i and S_j represent the sizes of both cells i and j, while S_{ij} is the size of the shared geometrical space.
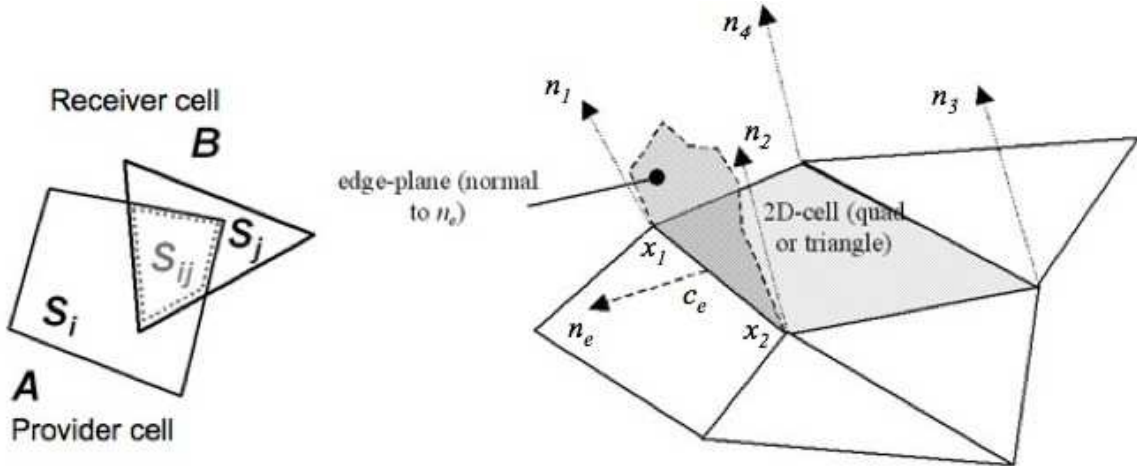
Figure 5.3: Spatial intersection between cells (l.) and geometrical representation of the projection geometry (r.) [8].

For a three-dimensional cell, the space contained is the intersection of the half-spaces defined by all cell-faces of the cell. The half-space defined by a face is the space below the plane through the face-center and normal to the face, with the normal pointing out of the cell. The face-center c_f and the normal $\overrightarrow{n_f}$ are computed by

$$\overrightarrow{c_f} = \frac{1}{n_v} \sum_1^{n_v} \overrightarrow{x_i}$$

$$\overrightarrow{n_f} = \sum_{i=3}^{n_v} (\overrightarrow{x_{i-1}} - \overrightarrow{x_1}) \times (\overrightarrow{x_i} - \overrightarrow{x_1})$$

(5.2.1)

where x_i is the position vector of the i-th vertex of the face and n_v is the number of vertices of the face. This definition implies that the space contained in a three-dimensional cell is assumed to be convex.

For a two-dimensional cell (e.g. a triangle or a quadrilateral), the space it contains is defined as the intersection of the half-spaces defined by all edges of the cell. The half-space defined by an edge is the space below the plane through the edge-center $\vec{c_e}$ and normal to the edge-normal $\vec{n_e}$.

$$\vec{c_e} = \frac{1}{2}(\vec{x_1} + \vec{x_2})$$
$$\vec{n_e} = (\vec{x_2} - \vec{x_1}) \times (\vec{n_1} + \vec{n_2})$$

$$(5.2.2)$$

where x_1 and x_2 are the position-vectors of the edge start- and end-vertices, and n_1 and n_2 are the surface-normals at the edge-vertices. The surface-normals at the edge-vertices are determined by adding up the normal vectors of all faces containing the respective vertex.

An attribute value b_j for a receiver-cell j is obtained from a weighted sum of the values a_i over all provider-cells i.

$$b_j = \sum_i w_{ij} a_i$$

$$(5.2.3)$$

The weighting factor w_{ij} is computed from the intersection volumes (or areas) S_{ij}, depending on whether the attribute is extensive or not. The values of w_{ij} for extensive attributes, e.g. mass sources in [kg/s] or forces in [N], are proportional to the cell size S_i of the source cell i:

$$w_{ij} = \frac{S_{ij}}{S_i}$$

$$(5.2.4)$$

On the other hand, for non-extensive attributes as pressure, velocity, temperature and mass fraction, which do not depend on the size of the cell, the weighting factor is related only to the area S_j of the target cell j:

$$w_{ij} = \frac{S_{ij}}{S_j}$$

$$(5.2.5)$$

An example of intersection volumes between a cylindrical volume-mesh embedded in a Cartesian volume-mesh is shown in Figure 5.4.

The 3D to 2D mapping appears really important in the case of coupling the multiphase spray to a real engine on compression run. In fact, the swirl gas motion in the cylinder chamber has to influence also the region near the nozzle hole in the computational domain of the Eulerian spray. This transfer of information needs to be done with the mapping of the 3D engine field to the 2D spray boundaries.
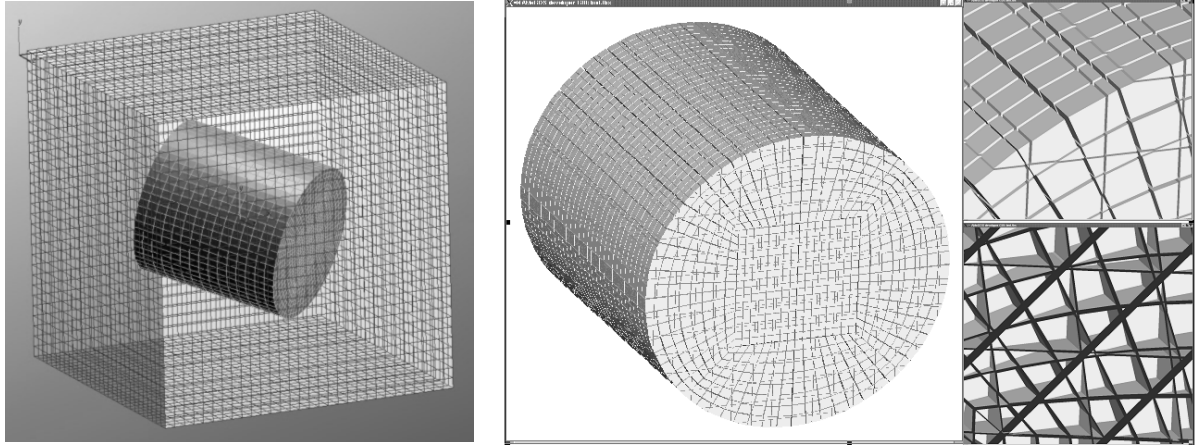
Figure 5.4: Example of 3D mesh intersection.

In many preliminary tests on simple gas flow coupling it appeared that the total pressure boundaries were unable to transfer the correct velocity field from the source to the target mesh, in this case from engine to spray. Moreover the adoption of velocity boundaries appeared insufficient, since the resulting velocity field was correct, but on the contrary the pressure field was poorly represented in the spray mesh. The definition of a new boundary was therefore necessary.

5.2.3. Advanced source boundary

For the development of the new boundary a simple test with the 2D square meshes in Figure 5.5 was assumed. The 2D flow field on the engine mesh needs to be transferred to the spray domain through appropriate mapping on the 1D boundary. The engine mesh presents a velocity inlet of 10 m/s and an outlet, chosen in order to give a rotational stream to the gas phase. The injected air presents a C_8H_{18} mass fraction equal to 0.025.
The Engine transfers to the spray the value of the C_8H_{18} scalar and mass fraction (Φ, α) and the velocity of the gas phase v_{target}, mapping them on the 1D boundary.

- The values Φ and α are directly imposed on the spray boundaries, together with pressure p, temperature T, turbulence κ and ε $\rightarrow$ Standard pressure boundaries are mapped.
- The velocity v_{target} represents the target value which should be reached in the spray mesh in the cells next to the boundaries. To obtain this a momentum source $S_{BND\text{-}Layer}$ is introduced in the cell layer adjacent to the boundary: the source will act on the gas phase until the target velocity v_{target} is reached.

$$S_{BND-Layer} = SU - SP \cdot v_{Spray}$$

$$\begin{cases} SU = A \cdot v_{target} \\ SP = A \text{ , (with } A = i.e. \ 1.000.000) \end{cases}$$

$$if \ \ v_{Spray} = v_{target} \ \ \Rightarrow \ \ S_{BND-Layer} = 0$$

(5.2.6)

This procedure is done only where the flow enters the receiver-mesh. The results on pressure, velocity and scalar concentration after 0.05 s are shown in Figure 5.6.

Velocity field

Pressure field   C8H18 field
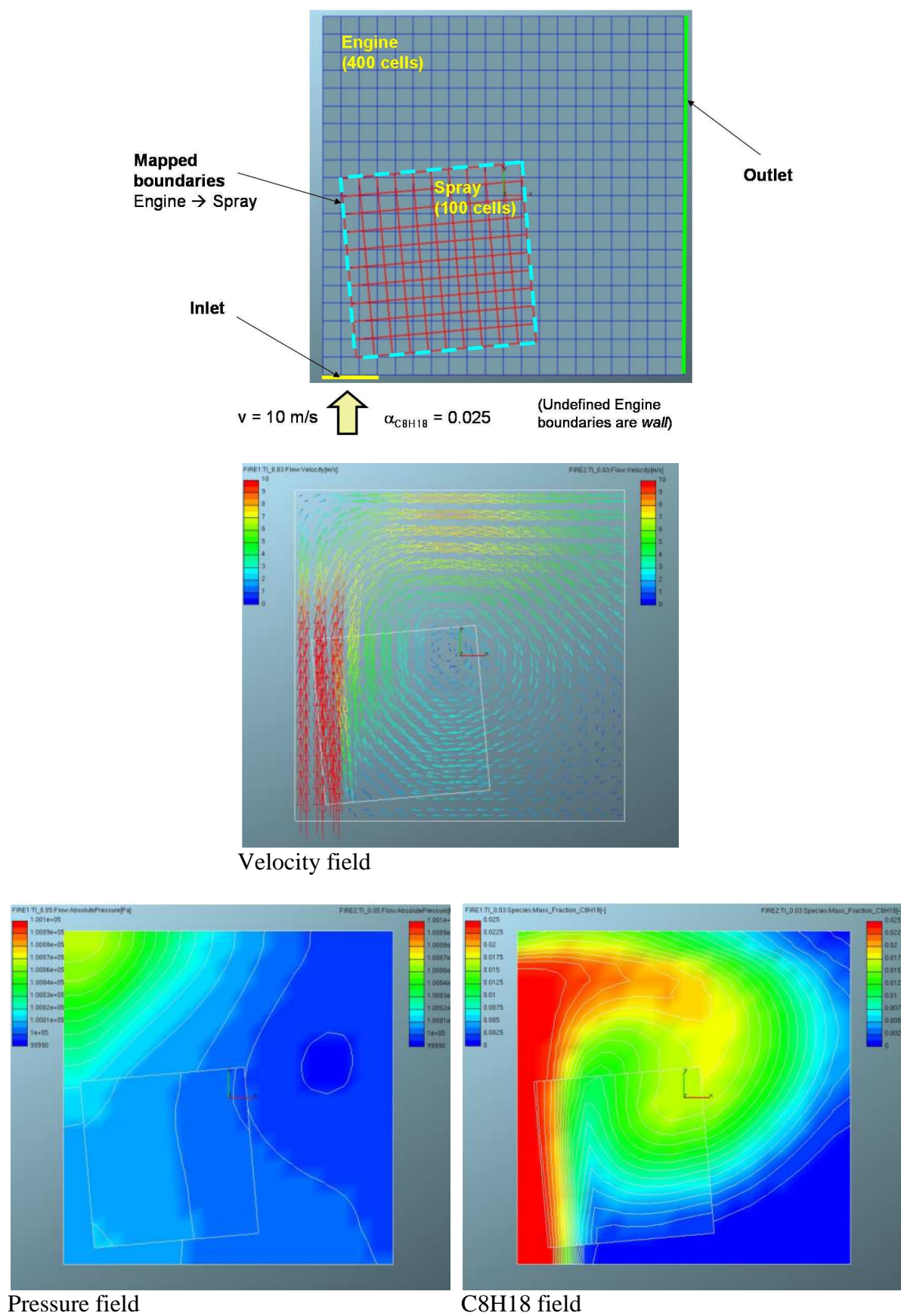
Figure 5.5: Coupling test with new source boundaries at t = 0.05 s.

This new boundary allows a better coupling between thermodynamic fields to be obtained; consequently it will be used in further tests. A more complex coupling example can be seen in Figure 5.6, where a 3D moving engine sector is coupled with a non-moving spray domain. The two images represent a vertical cut of both meshes near the end of the compression run, at 20° before top dead center. The resulting pressure and velocity fields appear very good transferred through the boundaries of the spray mesh.
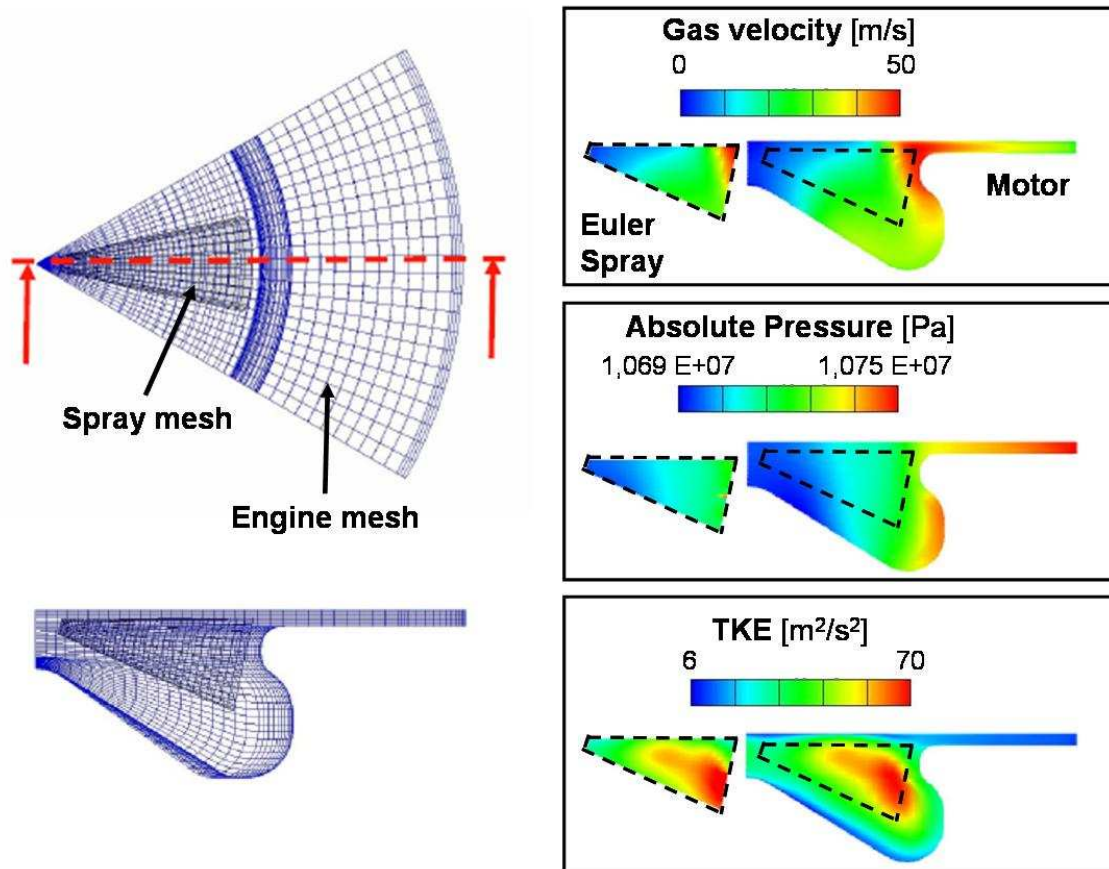
Figure 5.6: Gas flow coupling on moving engine mesh: results at Top Dead Centre (TDC).

5.3. Coupling of Lagrangian and Eulerian Spray

As shown in the previous sections, the coupling interface can compute the spatial mapping between two computational domains and transfer the flow information between them. In order to simulate the coupling of the Eulerian spray embedded into an engine mesh, further source terms for momentum, energy and mass need to be transferred.
The final aim is definitely to obtain an acceptable physical analogy between the flow fields in both codes: in order to get this, the correct data needs to be transferred at the right moment. The information flux has to be ruled through adequate interfaces, as shown in the following paragraph.

5.3.1. Interfaces

The coupling process needs interfaces through which data is exchanged between the two codes, which are schematically represented in Figure 5.7.

1. *Initialization*

At the beginning of the simulation the engine solver transfers the thermodynamic conditions (i.e. density, temperature, pressure, turbulent viscosity, turbulent kinetic energy, turbulent dissipation rate, …). and the fluid properties of the gas mixture phase (i.e. dynamic viscosity, thermal conductivity, thermal capacity, …) to the spray solver.
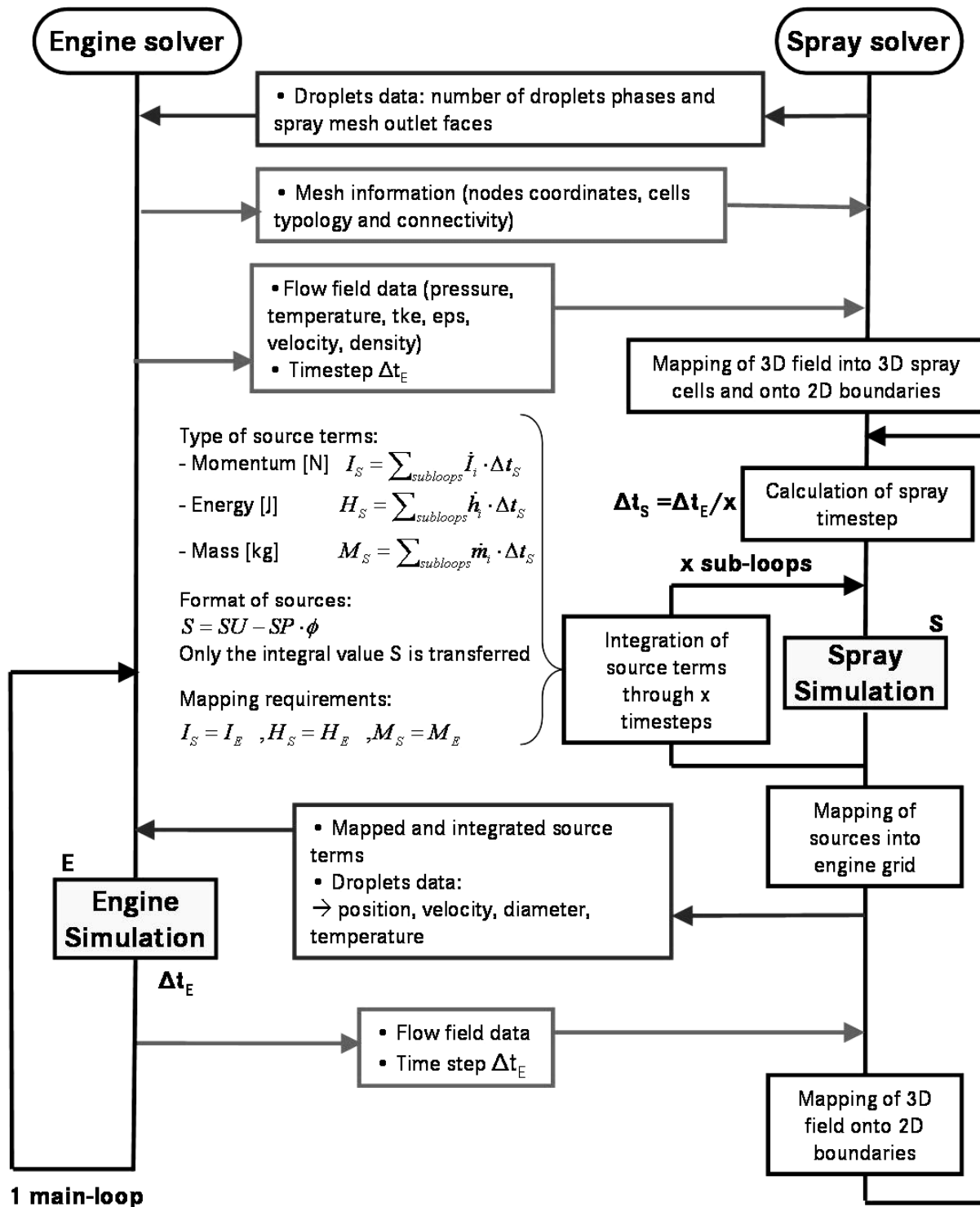

Figure 5.7: Detailed coupling flow chart.

2.   Definition of time-step

The time-step in the spray solver is usually smaller than in the engine solver, as the cell dimension and the dynamic conditions are different in both codes. The time step has therefore to be adapted in the spray simulation as a fraction of the engine one.

3.   Spray inlet

The initialization of spray inlet could be realized through a database of previous nozzle flow simulations, which provides the boundary conditions for each droplet and gas phase.

4.   Source terms

The source terms for momentum, energy, mass and scalars have to be transferred and mapped from the spray solver to the engine grid. The sources could be represented by a scalar value or by a vector.

5.   Droplets

The statistical DDM parcels have to be introduced inside the engine grid according to user defined criteria on parcel number, mass and distribution on the outlet boundary of the spray mesh.

6.   Updating physical properties

During the spray simulation the physical properties of the gas and liquid phases have to be updated according to environmental conditions on i.e temperature and pressure. The values are extracted from a species database.

7.   Spray Boundaries

At the end of the engine time-step the thermodynamic conditions in the engine mesh have to be mapped on the spray boundary. The transferred values are: pressure, turbulent viscosity, temperature, turbulent kinetic energy, turbulent dissipation rate, volume fraction, boundary flux.

5.3.2. Sources

The interaction between droplets and air is described by the production of source terms ϕ_j acting on the gas phase:

- *Momentum*: the drag effects between droplets and air lead to a force which accelerates the gas phase;

- *Energy*: the energy used by the droplets to evaporate has to be subtracted from the gas phase;

- *Mass*: the vapour mass has to be added to the gas phase;

- *Scalar*: the scalar of vapour fraction needs to be transported and updated according to the evaporated droplets.
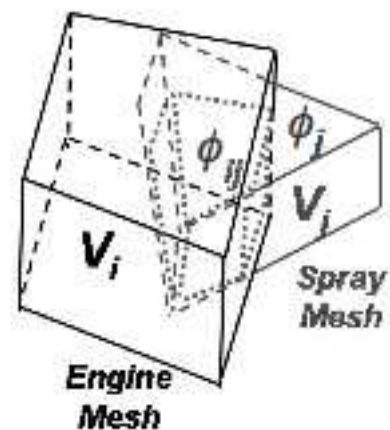

Figure 5.8: Volume Mapping of the source term ϕ_j.

The source terms ϕ_j have to be transferred to the engine mesh through a mapping procedure. For the involved cells the engine solver receives a value ϕ_{ij} which is added to the solver equations of momentum, energy, scalar and mass respectively. The volume ratio between source and target cells ($r=\phi_i/\phi_j$) is assumed as weighting factor (see Figure 5.8) to calculate the transferred value ϕ_{ij}. In the case of different time steps between spray and engine codes, the mapped sources are integrated and then transferred at the chosen exchange points. The mathematical description of sources was presented in section 3.3.2.

The geometrical scheme of the coupling process is shown in Figure 5.9. The boundary topologies in the spray mesh are wall, velocity inlet and outlet pressure; in the engine grid the boundaries are wall and outlet pressure, or eventually moving wall for the simulation of an engine compression run

The source terms are transferred from the whole spray mesh volume to the overlapping region in the engine grid, while the DDM parcels are injected at spray outlet boundary II (see Figure 5.9). The boundary conditions for pressure are mapped from the engine to the spray code over the surfaces I and II. As mentioned before, the spray grid must be finer than the engine grid in order to resolve the physics of the injection process.
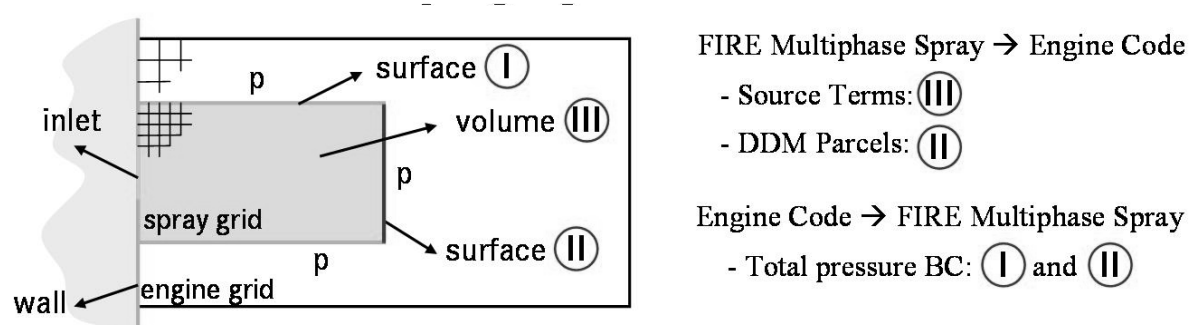
Figure 5.9: Boundary and coupling regions schematic representation.

5.3.3. Coupling Fire-Fire

The coupling method was initially applied on simple non-moving geometries, in order to test the reliability of the procedure. The ACCI interface is run between two Fire solvers, the multiphase spray and the single-phase engine.

The grids adopted in the first test are shown in Figure 5.10: the spray mesh (8400 cells) is adaptive, with a length of 15 mm and the nozzle inlet has a diameter of 205 μm. The engine grid (27000 cells) is also adaptive and has a length of 80 mm. Momentum, mass, scalar and energy source terms are transferred according to the scheme of the previous paragraphs.

The Eulerian spray is simulated with the model developed by AVL. The chosen number of phases is six, one for gas and five for droplets with fixed diameters of 5, 10, 20, 40 and 205 μm. The activated models are evaporation (Abramzon-Sirignano), primary break-up, secondary break-up, drag and turbulent dispersion.

The engine calculation is done for a single phase with standard species transport. The simulation is performed in a hot environment of 900 K and with pressure of 20 bar, in order to achieve conditions similar to a real engine. The injection velocity profile is extracted from I/D-Level experimental data on a 1-hole injector, where also measured spray penetration lengths are available. In this case a simulation of the internal nozzle flow was not performed.
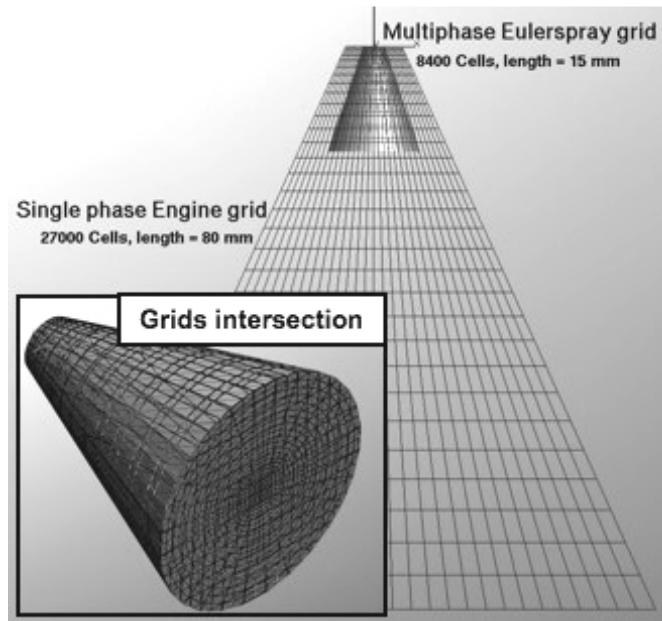
Figure 5.10: Fire-Fire coupled meshes.

The coupling results in terms of velocity are shown in Figure 5.11. The overall gas flow appears similar in shape and magnitude for both meshes. Moreover, in the engine case no discontinuities could be observed at the DDM-parcels initialization surface. Near the spray inlet the differences in coupled cell volumes lead to an expected underestimation of engine gas velocities, as the coarser engine cells cannot intrinsically reproduce the velocity profiles in the region just outside the nozzle orifice. Nevertheless, the lack of engine grid resolution was one of the reasons for the embracing of an orifice resolved Eulerian spray model.
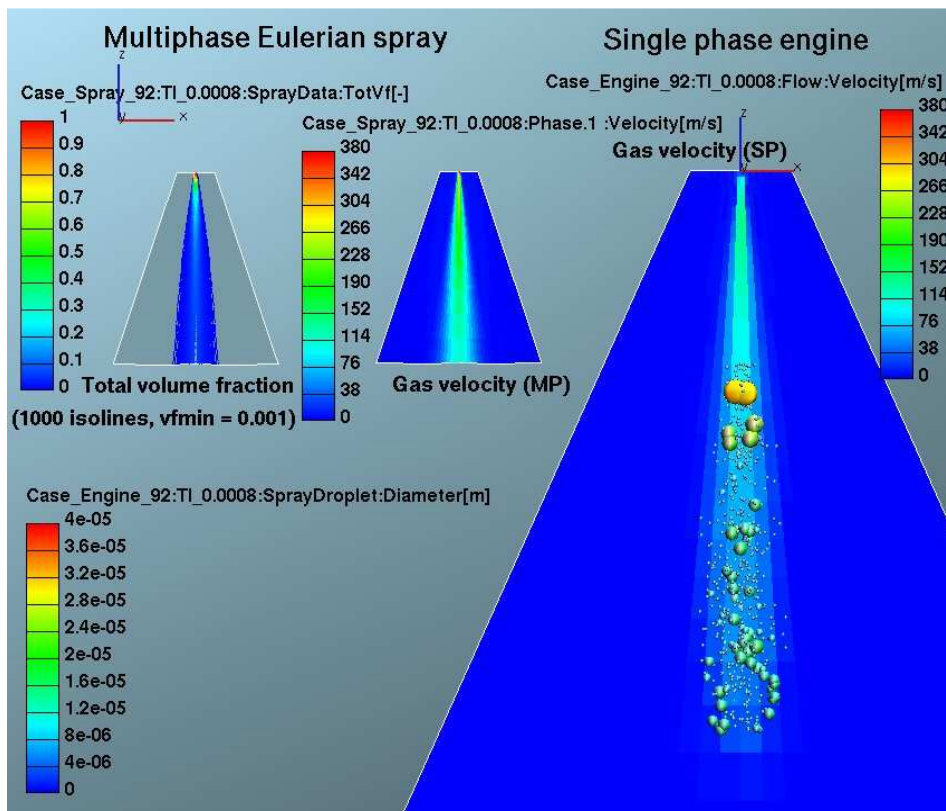
Figure 5.11: Fire-Fire Eulerian Spray coupling in hot chamber: velocity prifiles [24].
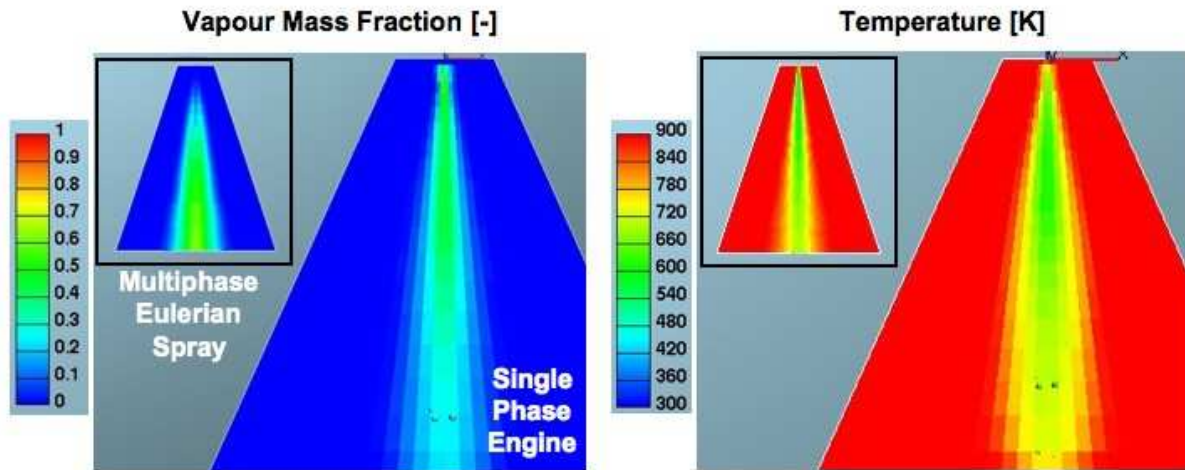
Figure 5.12: Fire-Fire Eulerian Spray coupling in hot chamber: vapour and temperature profiles.

The same consideration is done for temperature and vapour scalar fields, as shown in Figure 5.12. They look comparable in both codes, which means that energy, mass and scalar sources are correctly mapped between the grids. The only differences can be found in the region near the injector, with the same estimated reasons as for the momentum sources.

The spray liquid and vapour penetration curves are shown in Figure 5.13. The dashed line represents the transition between the Eulerian and the Lagragian domains. The liquid trend appears properly built, whereas the vapour phase is underestimated, mostly in the region far away from the injector. A reason for this behavior can be found in the coarse engine grid resolution and in the absence of spray initialization via previous nozzle flow simulation, which could strongly affect the spray entrainment, as shown for example in [11].
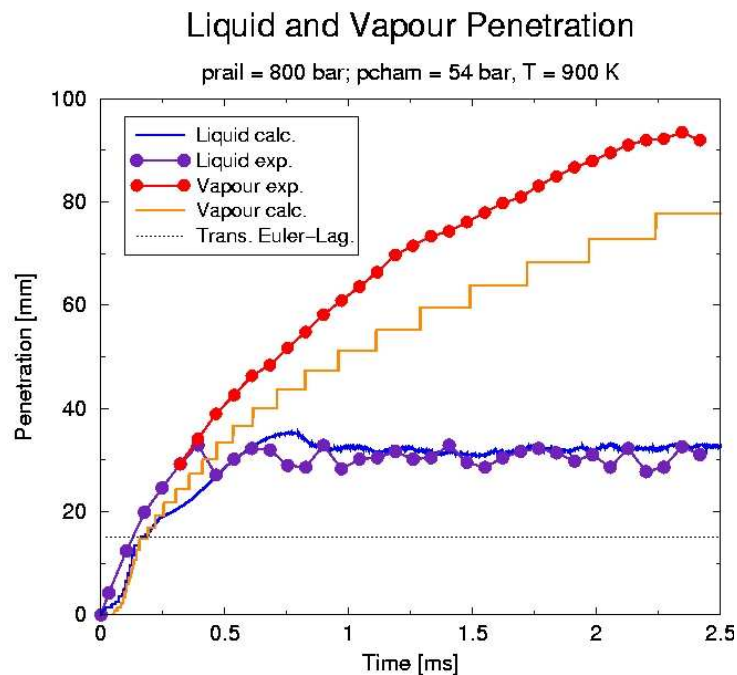
Figure 5.13: Fire-Fire coupling in a hot chamber: vapour and liquid penetration curves.

In a real engine the swirl motion of the in-cylinder flow plays a relevant role in the mixture formation process. For this reason the coupling method has also to allow the constant transfer

of cross flow through the boundaries of the spray mesh. In order to test the coupling capabilities, a 5 m/s velocity is imposed on the engine domain. The cross flow effects can be seen in Fig. 5.14 in terms of liquid volume fraction: the Eulerian spray appears affected by the flow conditions in the engine mesh, leading to a spray deflection from the main injection axis.
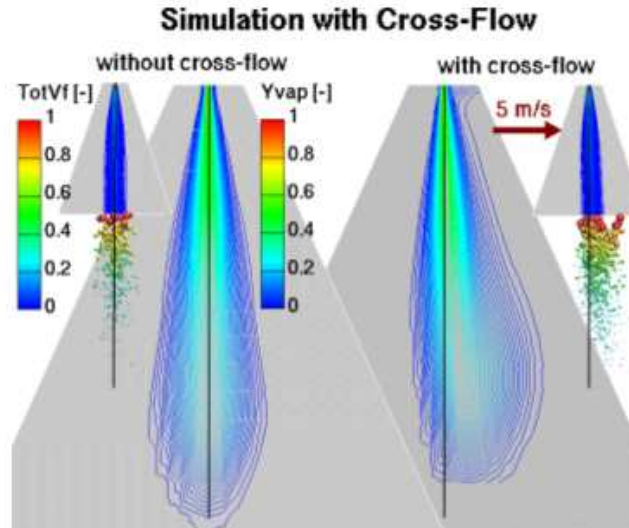

Figure 5.14: Cross-flow effects on the coupled Eulerian spray.

5.3.4. Coupling StarCD-Fire

The above discussed Fire-Fire coupling concept is afterwards applied between two different CFD commercial codes: Fire for the multiphase spray and StarCD for the single-phase engine. The code StarCD has to be compiled with the ACCI libraries, so that the coupling syntax and the common arrays are available in both solvers. Exchange points and transferred terms have therefore to be defined via user routines.

The first test is performed between a truncated cone spray mesh and a cylindrical engine box, as presented in Figure 5.15. The results show that the coupling method could be adapted in order to allow the interconnection between different CFD tools. As previously emphasized, the flow in the region near the injector cannot be precisely reproduced in the engine solver. The transition to DDM parcels appears furthermore correctly mapped.
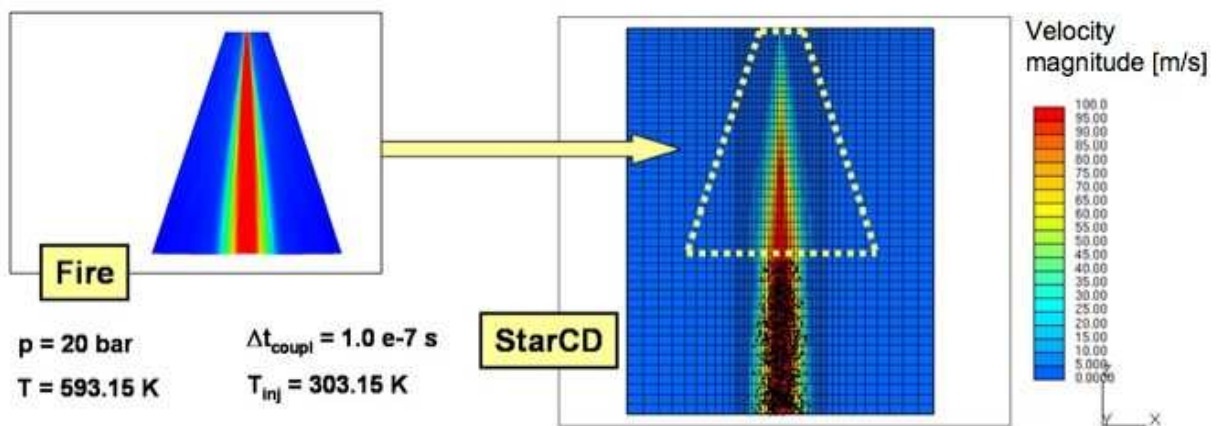

Figure 5.15: First coupling between different codes: Fire and StarCD.

Due to time requirements in industrial applications the computational grids cannot be arbitrarily refined. For this reason the second case is generated with a standard cell distribution of a 3D engine sector mesh. The aim of this test is to evaluate if the coupling method could allow a correct reproduction of the gas velocity in both domains. The cylinder motion is hence avoided and the flow field is barely produced by the transferred momentum source terms. Further effects of swirl and cylinder flow will be considered in the following chapter, where a complete simulation of the engine run will be presented. The results of this test case are shown in Figure 5.16. Gas velocity profiles along the lines A-A and B-B on the coupling domain show good agreement between spray and engine solutions. As previously observed for the coupling Fire-Fire, the engine gas velocities are underestimated near the spray inlet location, as shown along the line A-A. This behavior could be justified by two aspects: first, the bigger cells of the engine mesh, second, the high volume fraction of the liquid phase in the spray mesh near the nozzle orifice. According to this, the target cells in the engine mesh, which are bigger and filled only by the gas phase, receive momentum sources that accelerate the gas mass less than in the smaller and liquid-saturated cells of the spray case. Nevertheless, this behavior provides a further reason for the adoption of the Eulerian concept in the near-orifice cylinder region, as the exchange processes between the gas and the liquid phases could be only described in a sufficiently refined mesh and by the statistical quality of the Eulerian approach in the thick spray region. Far away from the injector the spray dilution and the comparable cell size lead then to a good agreement between both gas flows. At the droplets entrainment location the gas flow is comparable with both solver: this condition represents an essential requirement for the quality of the coupling method.
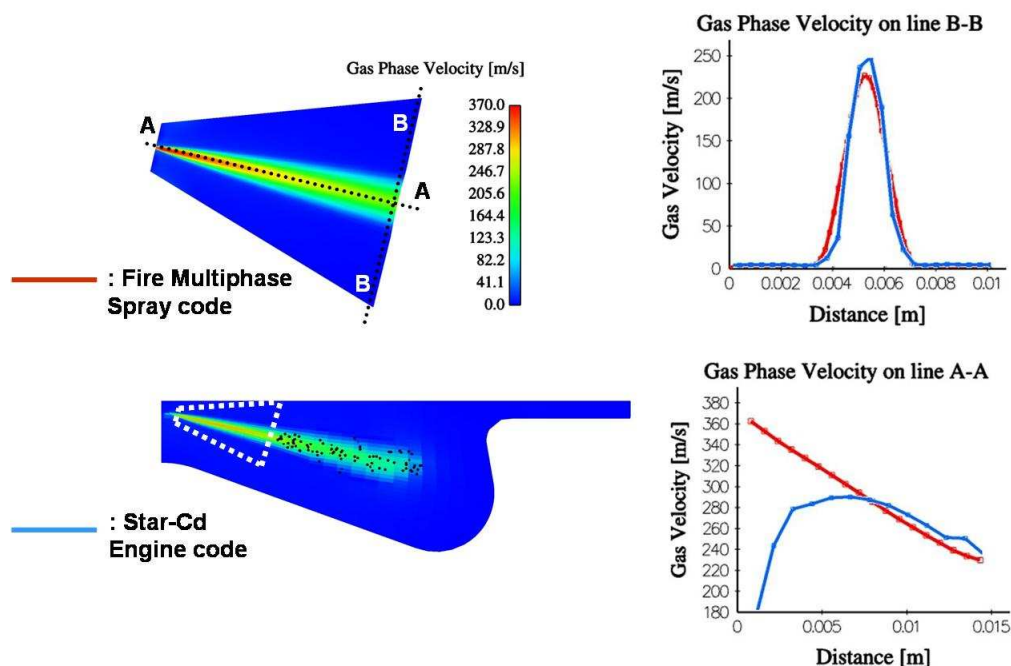

Figure 5.16: Second coupling between Fire and StarCD: gas velocity through momentum source terms.

As shown in these last applications, the coupling method allows the integration of the multiphase Eulerian model with a generic engine code. The advantages of an orifice-resolved spray simulation could be therefore transferred to a standard engine case, with the aim of predicting more realistic spray formation and consequent effects on combustion and emissions formation.

6. Application on engine case

This chapter will describe the application of the coupling technique in the simulation of an operative DI diesel engine case, in order to address the advantages that the concept could provide to the engine design process. The new method offers a better description of the spray near the injector, as it accounts for a deeper physical and statistical description of the exchange processes and the interactions between the liquid and the gas phases.

Before the present work the standard spray model was the DDM, insensitive to spray "history": the initialization of droplets is axis symmetrical, dispersion angle and droplets diameters come from previous assumptions. Currently the Eulerian spray model could account for different nozzle geometries, instabilities and multiple injection strategies, which directly affect the mixture formation.

The Eulerian spray could be initialized through a direct coupling with the nozzle flow, so that flow asymmetries, turbulence and cavitation are taken into account. Primary break-up modelling and local mapping of the flow field provide thus an enhanced initialization of the spray. Furthermore, the high grid resolution in the region just outside the nozzle orifice allows a more accurate description of the physics and turbulence exchange processes.

The goal of the procedure is to predict combustion and emission formation processes with different nozzle geometries. The simulation results are finally compared to experimental results, both integrally and locally.

6.1. Load point description

The advantages of the method will be proven on a truck engine from Mercedes-Benz. The experimental measurements include data on pressure curves, integral emissions level and transparent engine images. Previous results for the same engine can also be seen in [43]. A bore of 106 mm and a stroke of 136 mm characterize the cylinder geometry. The load basis point presents a speed of 1750 rpm, 26 % EGR and mean equivalent ratio equal to 1.5.

The first test was performed on the above mentioned basis point without the coupling with the nozzle flow simulation, in order to test the reliability of the coupling method in comparison with the standard spray models (see Figure 6.1).

The local values of mixture fraction and temperature show that the results with the validated ICAS 1D Eulerian model and the coupled 3D Eulerian spray are comparable: this suggests that the method could reproduce a standard combustion case and that the implemented interfaces are capable to interlink appropriately Fire Multiphase and StarCD codes. The simulation with the standard DDM model illustrates a discontinuous evaporation process in the region near the nozzle, as the gas-liquid exchange processes results underestimated.
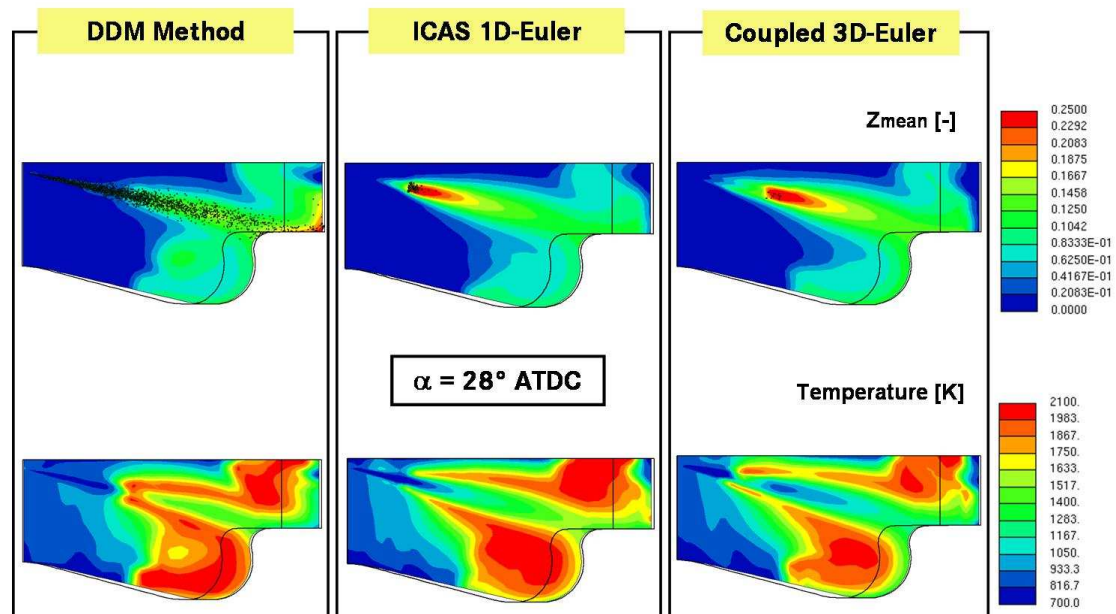
Figure 6.1: Simulation results on a cylinder section with different spray models.

Having stated the reliability of the coupled Eulerian approach, the aim is now to define the nozzle flow effects on spray and combustion. Test bench measurements on this engine show that different nozzles (Sac hole, VCO) with the same injected fuel mass strongly affect the emission formation. This behavior is predominant on soot formation, as shown in Figure 6.2: particularly for a late injection point (i.e. the number 2) the differences appear strong. In the current work the effects of nozzle shape on combustion will be analyzed for the load point 3 with a load of 80 %: in this case the differences in soot formation are still evident, even if not so drastic as in the late injection case 2. Nevertheless, those kind of configurations are furthermore of evident interest for standard combustion processes.

| Load point | Start of signal ATDC | |
	883 Sac Hole	915 VCO
2	6.0	6.0
3	0.0	0.0
4	-6.0	-6.0
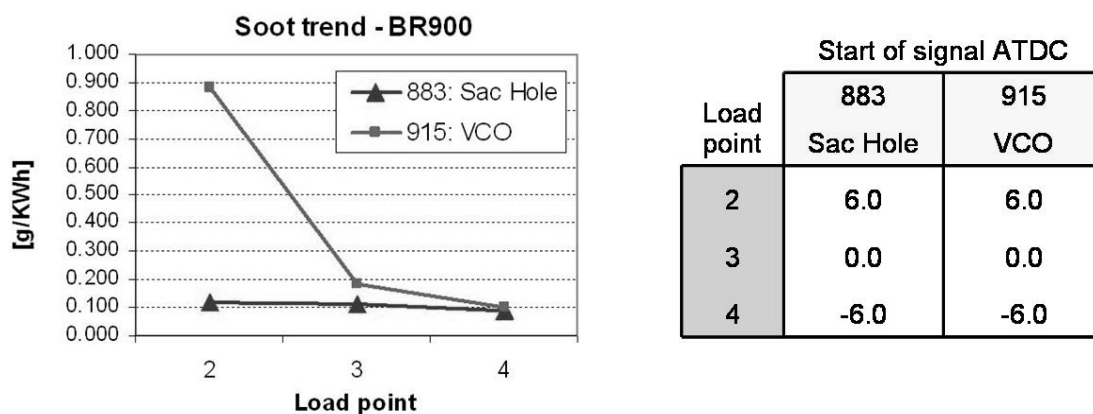
Figure 6.2: Effects of nozzle geometry on soot formation for different load points.

6.2. Nozzle flow simulation

In the two cases the injectors are mounted with a sac hole (SaLo) and a sac less – VCO (SiLo) nozzle. Both configurations have the same specifications in term of mass flow (HD 1100) and maximum rail pressure (p_{max} = 2000 bar).

First, the nozzle flow will be simulated and the outlet mass flow compared with the 1D hydraulic simulation, which fits the test bench injected mass. Afterwards, the nozzle outflow field will be directly transferred via a primary break up model to the Eulerian spray.

The first step in the nozzle flow simulation is the achievement of boundary conditions: by using a 1D hydraulic simulation the curves for needle lifts and rail pressures are obtained. The transient simulations of the internal nozzle flow are then performed with the experimental cylinder pressure as an outlet condition.
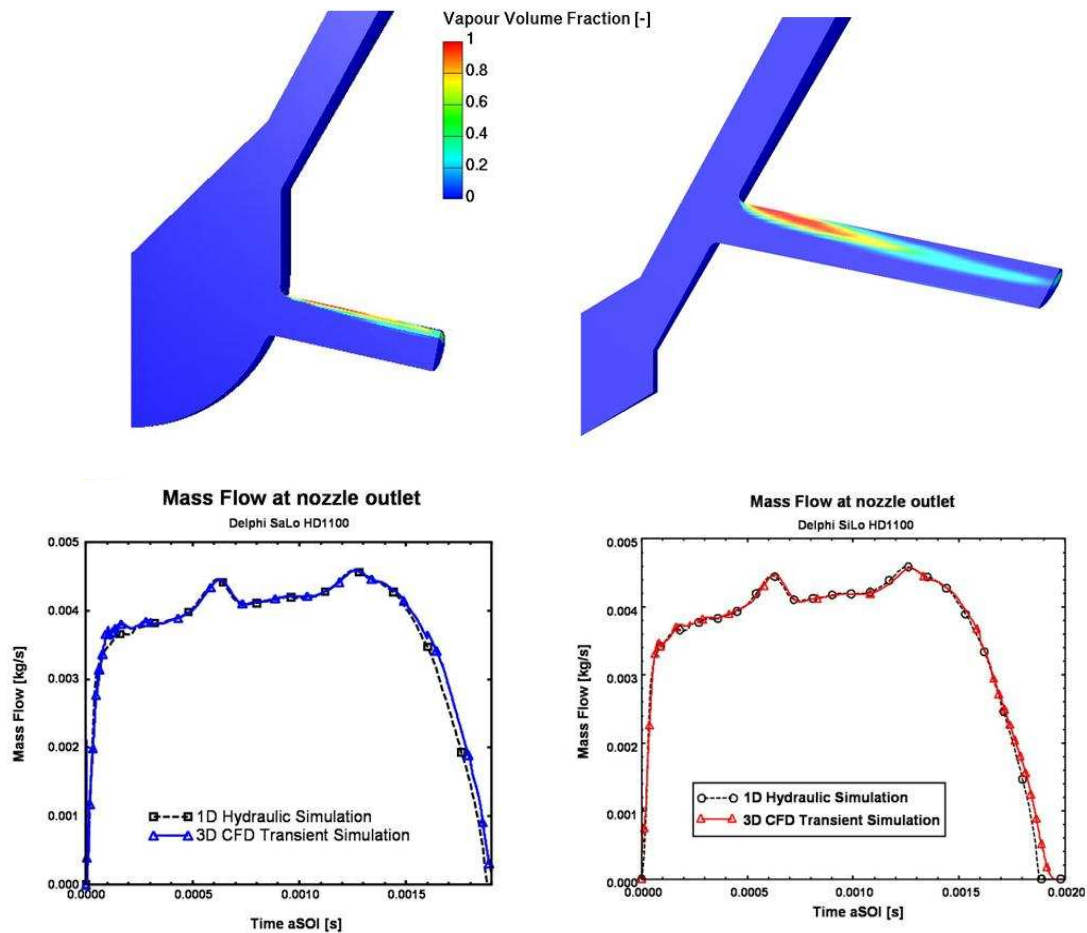
Figure 6.3: 3D-CFD nozzle flow simulations at t=1 ms and comparison 3D-1D integral mass flux for Sac Hole (l.) and VCO (r.) nozzles.

Figure 6.3 shows an example of the 3D results in terms of vapour volume fraction. The cavitation region reaches the nozzle outlet in both cases, even if more consistently for the VCO configuration. The nozzle section allows also the geometrical differences to be noticed between sac hole and VCO nozzles: in the first case the needle closes onto the nozzle body, while in the sac-less configuration the injection hole is directly closed by the needle itself.

The calculated 3D mass flow at nozzle orifice provides a high satisfactory agreement with the 1D hydraulic simulation. Only in the closing needle phase the 3D mass flux is a little overestimated: this could be due to the fact that the CFD model does not allow instantaneously closing of the needle, permitting a small fuel blow-by in the hole. Moreover, in the needle opening the sac hole nozzle presented strong instabilities in the orifice flow field, mainly due to a migration of the cavitation cloud from the bottom to the top of the injection hole [51]. Afterwards, when the needle is completely opened, the flow field for the VCO nozzle appeared more affected by cavitation, as shown in Figure 6.3. The good

agreement on 3D nozzle mass flow is obtained simply by setting measured pressures at inlet and outlet boundaries. A parameter that plays a key role in the nozzle flow is the connecting radius between hole and body. This value is usually unknown, as the hole rounding is obtained in the production with an erosion process running until the achievement of the characteristic mass flow. For this reason the CFD mesh connecting-radius was increased until the target 1D mass flow was reached. In this case the hole rounding was enlarged up to values of respectively 30 and 20 μm for VCO and sac hole nozzle.
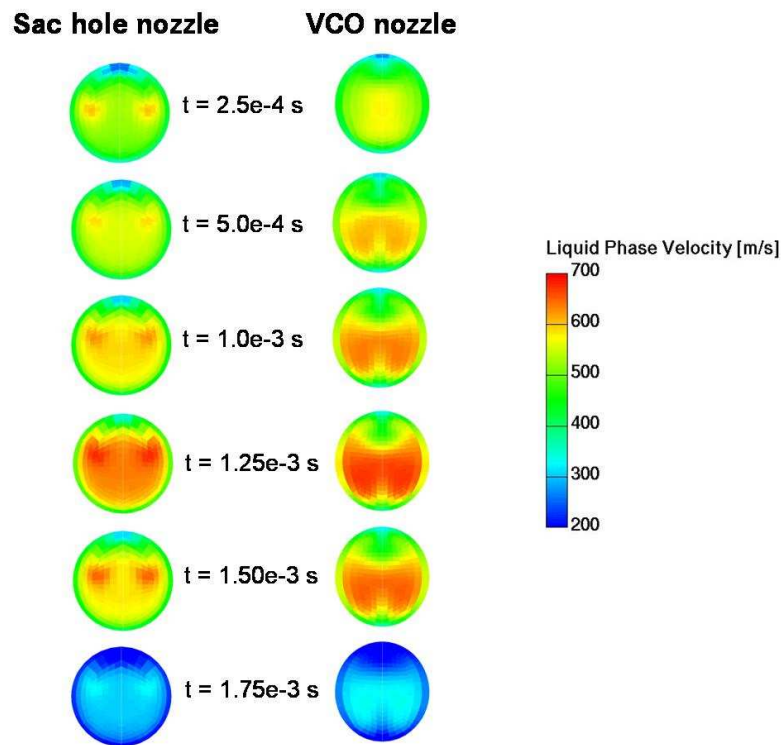
Figure 6.4: Nozzle orifice section for Sac Hole (l.) and VCO (r.) nozzles at different time steps: liquid phase velocity.

The local flow field at the nozzle orifice is shown in Figure 6.4 at different time steps. The turbulence level and velocity distribution in the sac hole nozzle appears more homogeneous than in the VCO configuration. Nevertheless, the comparison in Figure 6.5 shows how the turbulent length scale at nozzle orifice is more asymmetrical for the sac hole configuration. This should lead to a stronger turbulent mixing process in the region near the nozzle hole, with noticeable effects on spray formation.
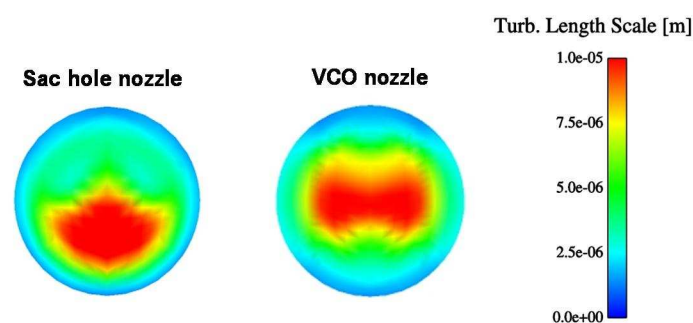

Figure 6.5: Nozzle orifice section for Sac Hole (l.) and VCO (r.) nozzles at t=1ms: liquid phase turbulent length scale.

The next step was to transfer the velocity and turbulence field at the nozzle orifice to the Eulerian spray, adopting primary break-up assumptions for the droplets class initialization [23]. In order to ensure that the coupling to spray could provide reliable results, comparisons with a cold chamber test case will be performed.

6.3.   Eulerian spray validation

Spray validation will be shown with experimental results for an optically accessible high pressure cold chamber. The maximum ambient pressure is equal to 40 bar, corresponding to a gas density of 47.1 kg/m³. Injectors are mounted on an adapter on the backside of the chamber, which is equipped with three optical accessible windows.
A flash light source produces a wide light sheet that is directed through the two lateral windows. A CMOS high speed camera is positioned before the window in front of the injector tip and it is responsible for capturing the scattered light reflected from spray droplets (see Figure 6.6, left).
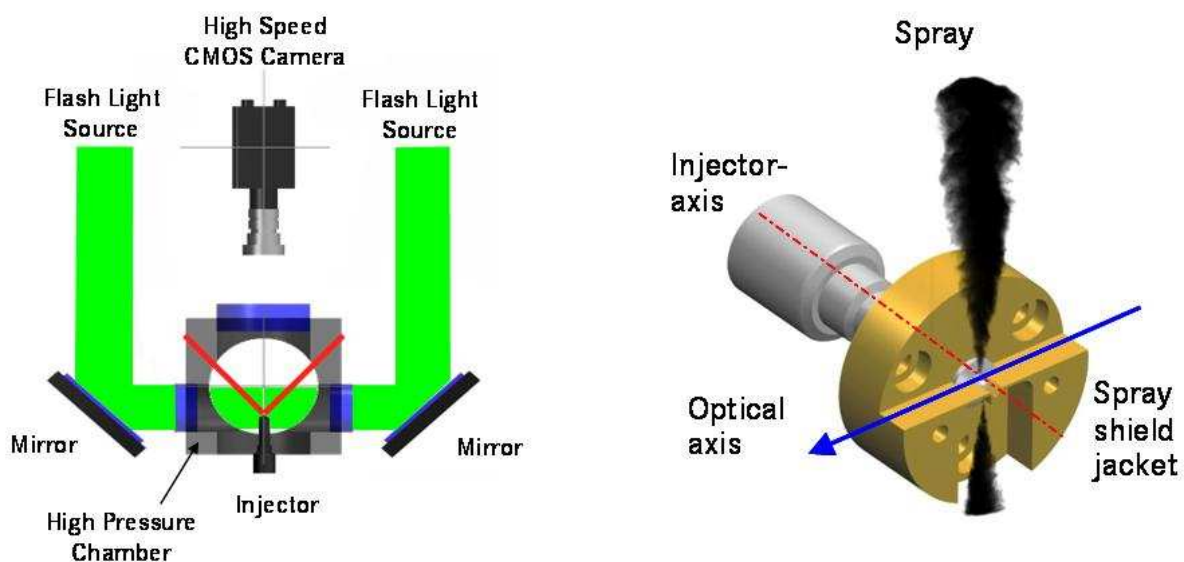

Figure 6.6: Cold spray chamber test rig with MIE–scattered light imaging technique (l.) and Spray shield jacket for side view investigations of the spray (r.) [14].

A shadow imaging technique is used for the side view investigations, as shown in Figure 6.6, right. A frosted plate-glass is positioned on a lateral window and it is illuminated by a flash light in order to create an homogeneous background illumination. In this configuration only one nozzle hole could be observed, therefore the other orifice axis needs to be directed downwards or they should cover the optical axis of the set up. The other sprays are directed downwards to a spray shield jacket. According to the different tip contours, both sac hole and VCO type nozzles need a separate shield jacket.
The Eulerian spray was simulated afterwards on a cylindrical test mesh of 50000 cells and extended for 50 mm. The grid was boundary adapted in order to fit the nozzle body and the orifice as inlet (see Figure 6.7). The initialization of velocities and droplets classes is obtained with a primary break-up model, according to a chosen number of 6 droplet phases.
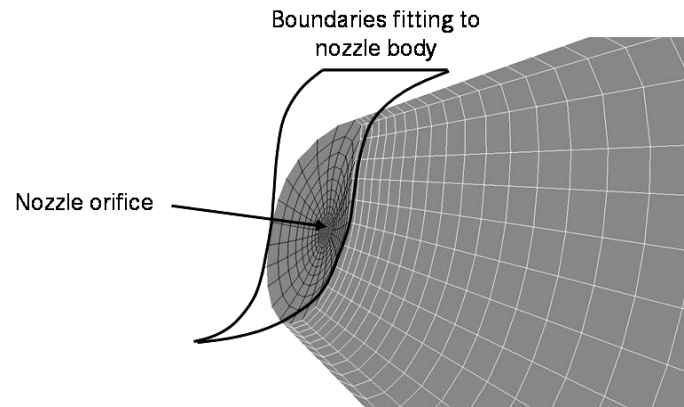
Figure 6.7: Mesh for Eulerian spray computation.

Comparisons between simulated spray shapes and experimental images are shown in Figures 6.8 and 6.9. The VCO nozzle generates smaller spray angles, mostly in the region near the orifice (near view). The simulated sprays show good agreement with experimental images, also in the reproduction of spray asymmetries.
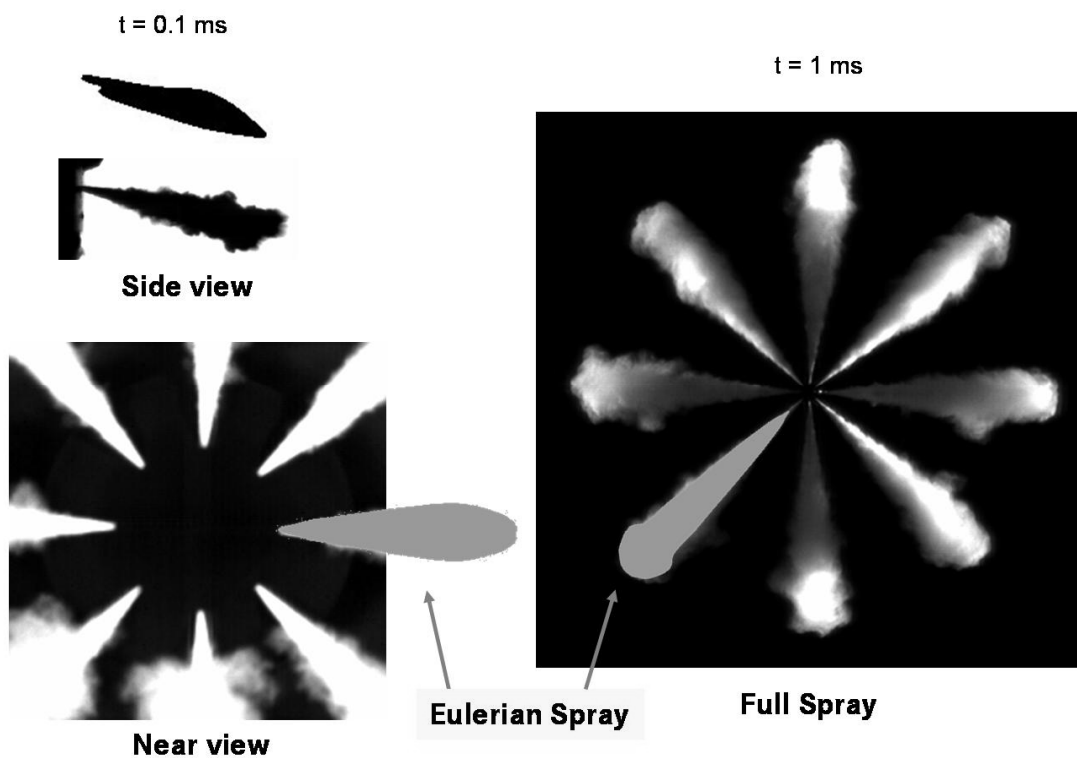

Figure 6.8: Coupled spray for VCO nozzle: simulation (isosurface 0.01 of total liquid phase) in comparison with experiments.

The strong spray atomization in the bottom spray plumes of the near view in Figure 6.8 is due to the effects of needle displacement at the beginning of the injection. As in VCO nozzles the needle opens directly on the holes, fluctuations lead directly to orifices obstruction and therefore strong effects on spray formation. The simulation of this kind of phenomenon would require a complete 360° nozzle mesh and the needle displacement not only in vertical direction, but also in the remaining two directions. Nevertheless, this kind of analysis does not match the engineering purposes of this work.
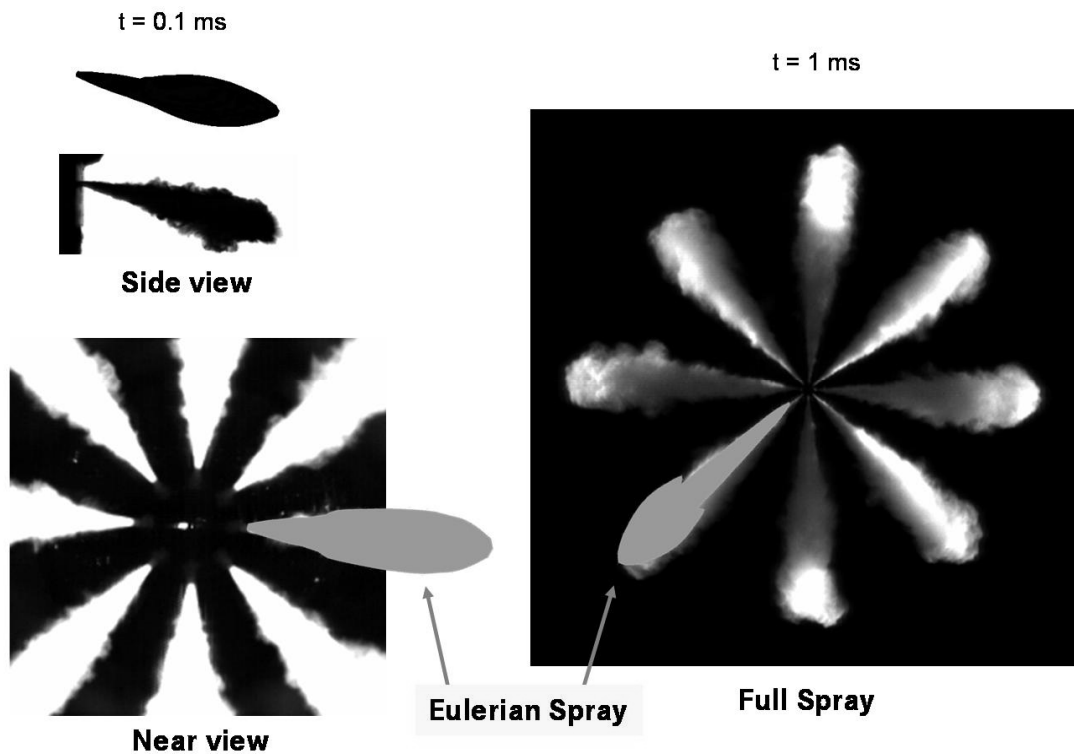
Figure 6.9: Coupled spray for Sac Hole nozzle: simulation (isosurface 0.01 of total liquid phase) in comparison with experiments.

The spray tip penetration for the sac hole appears slightly higher than for the VCO nozzle, as shown in Figure 6.10.
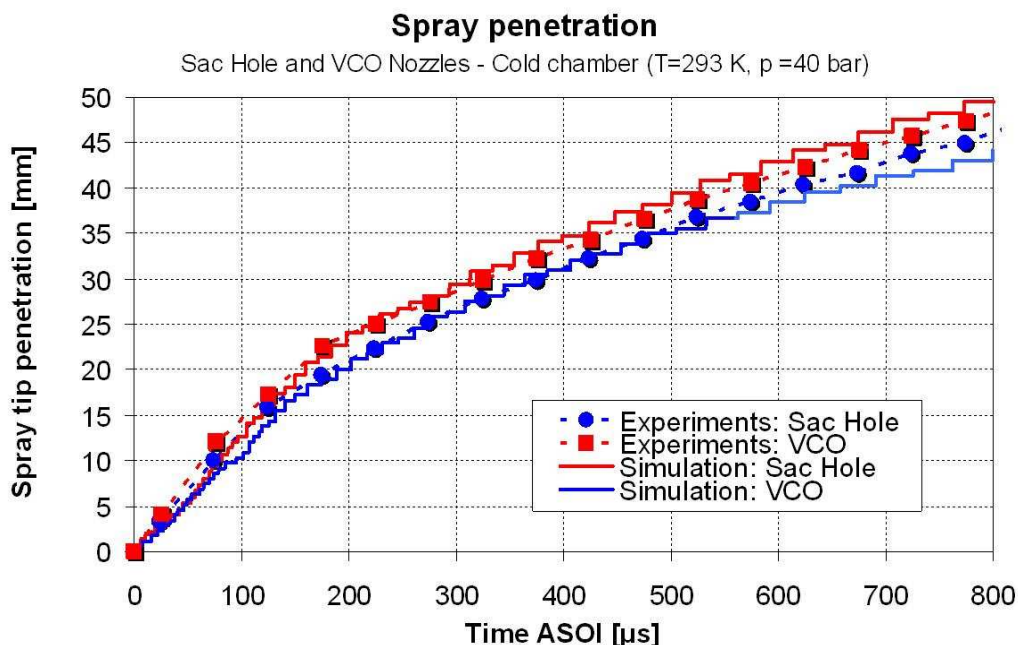

Figure 6.10: Experimental and simulated penetration curves for Sac Hole and VCO nozzles.

The coupling simulation method between nozzle and Eulerian spray produces satisfactory results on spray formation process; therefore, it enables the transfer of nozzle information to the mixture formation process in the combustion chamber.

6.4.   Engine simulation

For the validation of the introduced coupling concept, CFD simulations for the above mentioned heavy-duty truck engine were compared to measurements of a single cylinder engine and optical diagnostics. According to symmetry assumptions, only cylinder sector meshes were modeled, allowing a considerable reduction of the computational effort. For the coupling of the Eulerian spray and the engine code the geometry is shown in Figure 6.11.
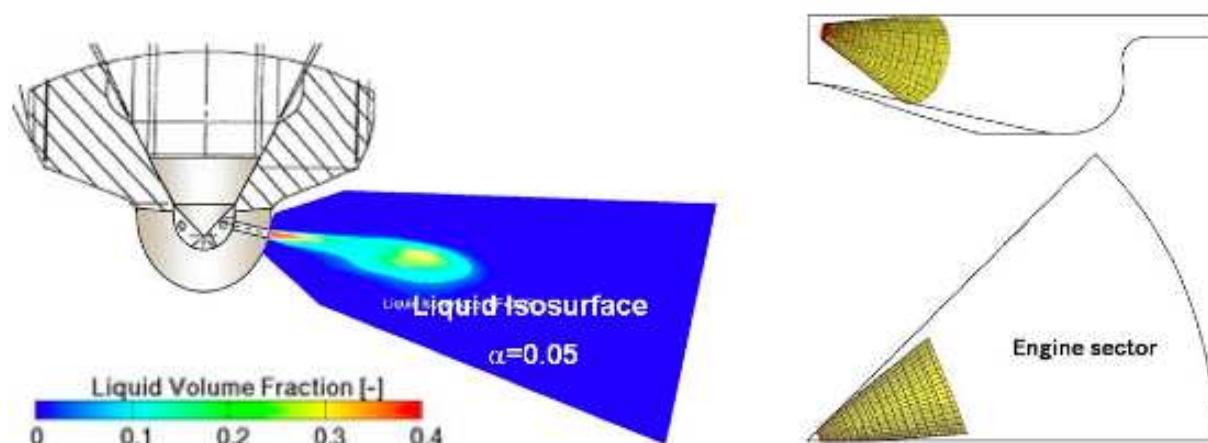

Figure 6.11: Mesh for Eulerian spray simulation.

The measured cylinder pressures are obtained with single-cylinder engines, while the heat release curves result from zero-dimensional pressure trace analysis based on data from simulations and measurements. Moreover, the spatial characterization of combustion and soot formation is obtained through an optical accessible single cylinder engine.
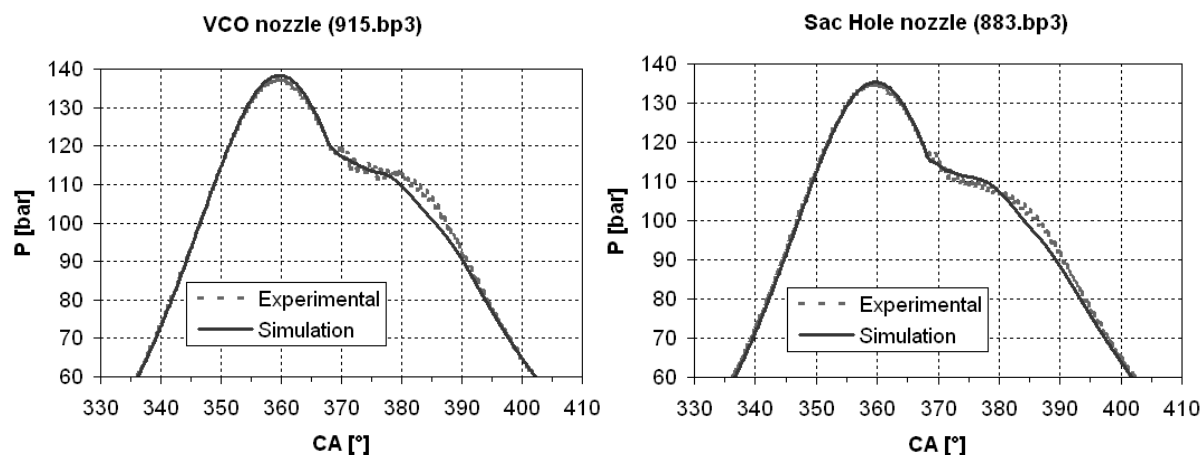

Figure 6.12: Pressure traces for the Eulerian spray coupled simulation: VCO nozzle (l.) and Sac Hole Nozzle (r.).

The considered load point presents a large injected mass and an intense combustion process after the occurrence of ignition. Nevertheless, the results in Figures 6.12 show an overall acceptable agreement in terms of pressure traces, both for VCO and sac hole configurations. Nevertheless, in the cylinder expansion run pressure values appear underestimated; this is probably due to the lack of confidence with the Eulerian spray model initialization. Further

analysis on evaporation, dispersion and breakup processes in the hot environment are therefore required.
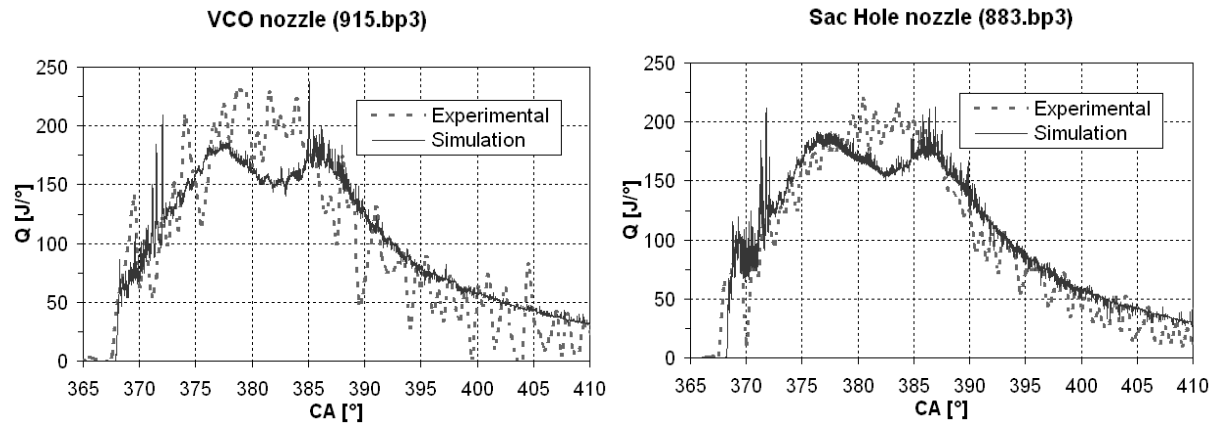
Figure 6.13: Heat release rate for the Eulerian spray coupled simulation: VCO nozzle (l.) and Sac Hole Nozzle (r.).

The heat release rate diagrams in Figure 6.13 confirm that the ignition time matches well with experiments for both simulations, even if the diffusion combustion peak appears underestimated and afterwards energy is slowly released during the expansion stroke.

In terms of simulated soot emissions, the adopted chemical model is still unable to provide quantitative predictions, as explained in [94]. Soot values are therefore underestimated, even if the trend is correctly captured, as shown in figure 6.14.
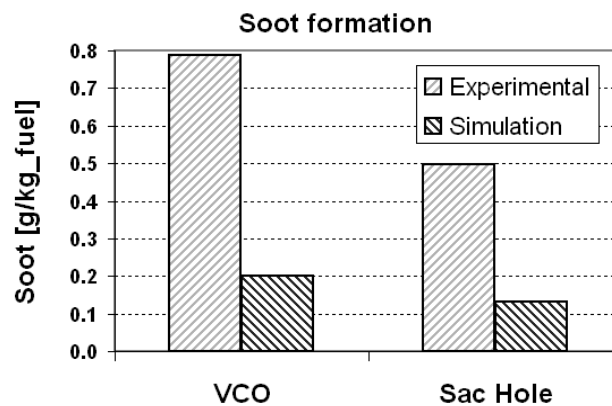

Figure 6.14: Experimental and simulated soot integral value for Sac Hole and VCO nozzles.

The measured pressure and the resulting heat release traces do not show large differences, at least enough to justify the different behavior in soot formation. To understand the reasons which lead to different emission values, local flow field distributions have to be taken into account.

Figure 6.15 shows a radial section of the cylinder, which depicts the distribution of soot mass fraction at different crank angles after the top dead center (ATDC). The engine mounted with the VCO nozzle tends to generate more soot and then to collect it in the lower part of the bowl, while in the sac hole configuration the soot particles catch the bowl edge and deviate more onto the squish region, where the high temperatures favor further oxidation. This could be an explanation of the different levels in soot emissions. Furthermore, at 15° and 25° ATDC the VCO nozzle case presents higher soot concentration along the spray axis, which could be addressed to the different mixture formation process at needle opening and closure.
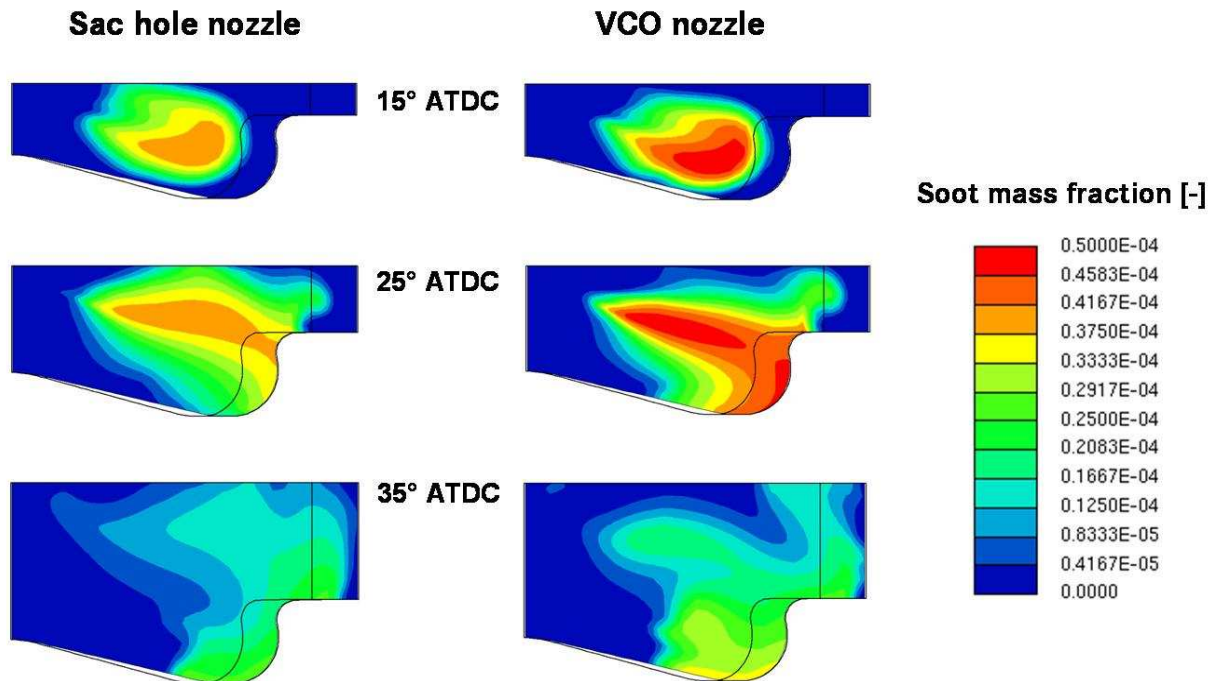
Figure 6.15: Soot mass fraction field in a cylinder section for sac hole and VCO nozzle.

The different soot formation behavior could be also seen in the soot traces of Figure 6.16, where the soot formation process in the first phases of the expansion run is stronger in the VCO configuration.
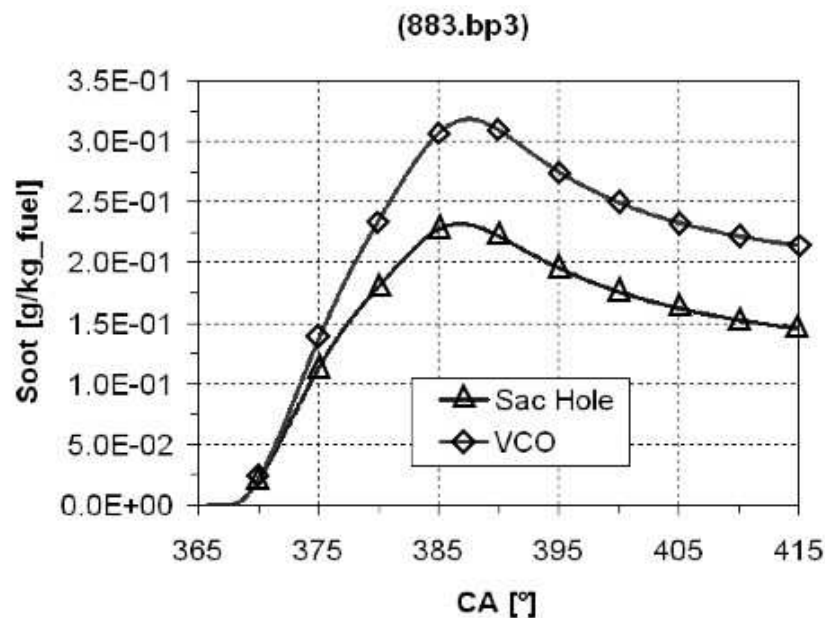

Figure 6.16: Soot traces at the beginning of the expansion run for sac hole and VCO nozzle.

Figure 6.17 shows the differences in temperature, soot and mixture fraction distributions at a late crank angle. As previously discussed, the VCO nozzle tends to collect a greater fraction of fuel mixture on the bowl, leading to fat zones there where more soot is produced. On the other hand, the smoother spray direction of the sac hole manages to collect part of the mixture cloud to the cylinder wall and to prevent stronger soot formation.
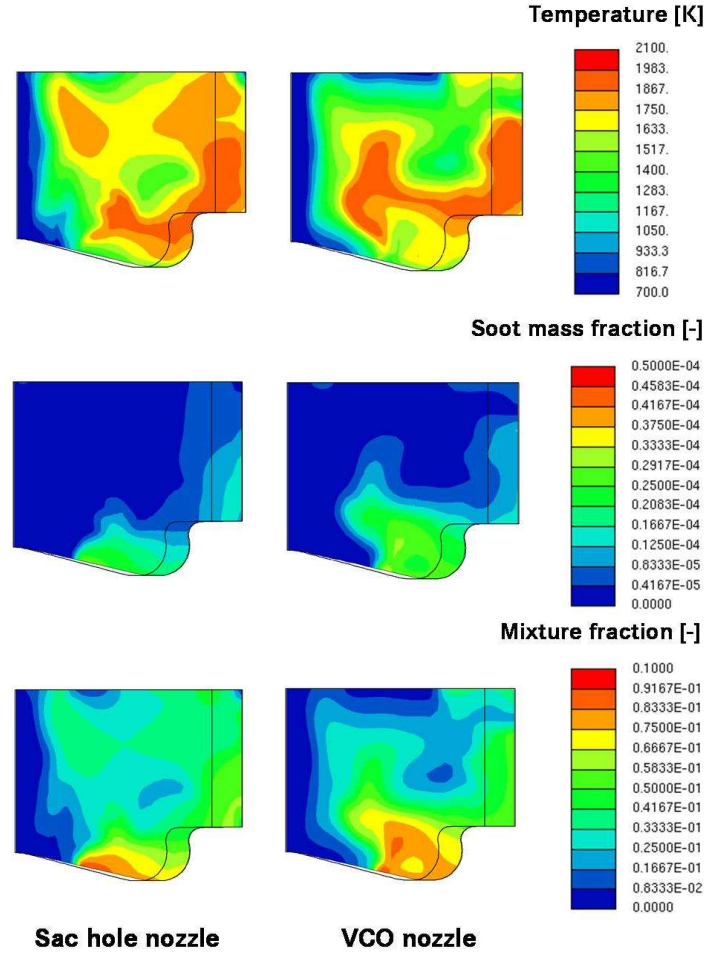
Figure 6.17: Temperature, soot mass fraction and mixture fraction fields in a cylinder section for sac hole and VCO nozzle at 50° ATDC.

6.4.1. Comparison with diagnostics

In order to analyze and understand the soot formation inside the combustion chamber, an optically accessible bowl was machined. Engine relevant features are identical to a modern single cylinder test facility [77]. A special elongated transparent piston containing a quartz window allows the optical access from the bottom of the bowl, which is also machined into a quartz piston. The pictures luminescence could be associated with the soot radiation [78], according to the detailed description in [94].

A comparison between diagnostic and local simulation results can be seen in Figure 6.18 and 6.19. The luminosity M_S is calculated by using the Stefan-Boltzmann law for grey bodies:

$$M_s = \varepsilon_s \sigma T_s^{\,4} \tag{6.4.1}$$

The terms σ and T_S are respectively the Stefan-Boltzmann constant and the temperature of soot particles. The emissivity ε_s is furthermore approximated with a correlation from [64]

$$\varepsilon_s = 1 - \left(1 + \frac{k}{C_2} f_v r_s T_s\right)^{-4} \tag{6.4.2}$$

where k is the extinction coefficient, f_v the soot volume fraction and r_S the radius of soot particles. Since equation 6.4.2 is valid for one parcel, it has to be multiplied by the number of particles in the considered volume. The computational results in Figures 6.18 and 6.19 are displayed with luminosity isosurfaces according to a characteristic value. The simulations for both injector types show a satisfactory agreement with diagnostics. The isosurfaces on the right hand side have to be considered mostly according to their shape, as the emissions of the under laying volume cannot be represented with this kind of post processing. Local characteristics of injection and combustion processes appear well predicted, even if the flame of the experiments shows a stronger radial diffusion. Simulated penetrations appear slightly under predicted, but the lower gas density in the transparent engine could explain this behavior: in fact, the piston has a higher elasticity than in simulation or single-cylinder measurements. Another reason could be found in the unavoidable distortion of the quartz piston window, which could influence the definition of geometrical boundaries in the experimental pictures.

According to the results on both injector geometries, the differences from a bottom view do not seem to be so relevant, at least according to the above discussed trends in emissions formation. In this case the local CFD results for a vertical cylinder section could provide a better understanding of the phenomenon, as previously discussed according to figure 6.17.
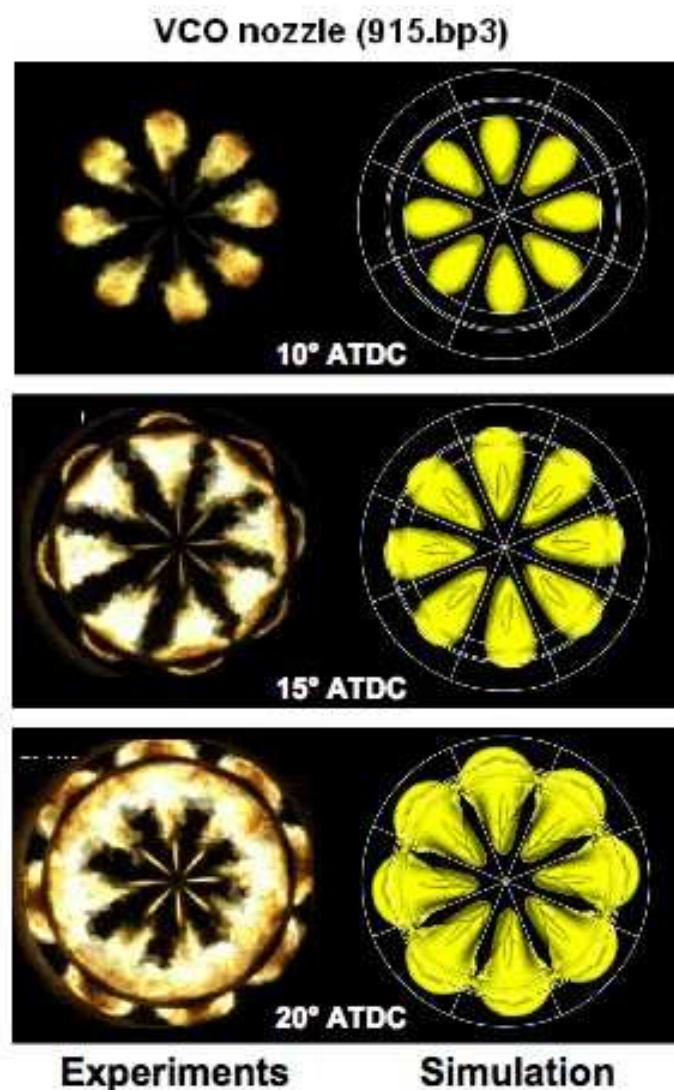

Figure 6.18: Comparison between simulation and diagnostic for heavy-duty truck engine with VCO nozzle (left: photographic sequence; right: calculated luminosity of soot).
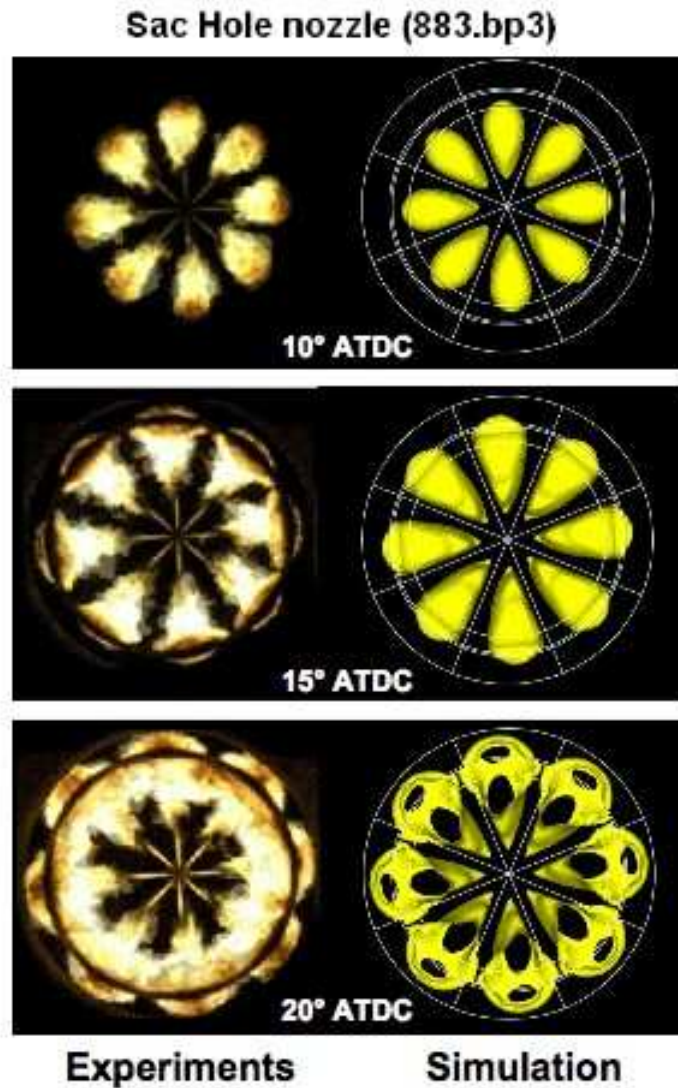
Figure 6.19: Comparison between simulation and diagnostic for heavy-duty truck engine with Sac Hole nozzle (left: photographic sequence; right: calculated luminosity of soot).

In the current analyzed case, the coupled simulation of nozzle flow, Eulerian spray and CFD combustion manages to supply more details than the transparent engine pictures. The soot emission from the bottom of the bowl could not reveal the concentration asymmetries in the vertical direction, leading to a more difficult interpretation of emission trends. Even if the simulated combustion itself appears still underpredicted in terms of the energy released, the local analysis of mixture and soot concentration in the combustion chamber leads to a deeper perception of thermodynamical phenomena.

7. Conclusions and outlook

The current work presents two approaches for the simulation of IC-diesel engines. The aim is to account for the effects of internal nozzle flow on combustion and emissions formation.

The first concept is founded on the creation of a library, which is based on previous nozzle flow simulations. Each point of the database is calculated according to different needle lifts and rail load pressures. Afterwards, the orifice flow data is converted to spray boundary conditions by means of primary break-up assumptions. During the engine simulations the droplets diameters and velocities are extracted from the library, providing a nozzle-flow-based initialization of the computational spray.

This second method represents an innovative concept for the real-time coupling of nozzle flow, Eulerian spray and engine simulations. The aim is achieved through the interconnection of different computational domains and CFD solvers. Starting from the two-phase simulation of the transient nozzle flow, the flow field at the orifice section was locally transferred to the Eulerian spray via primary break-up assumptions. The detailed prediction of spray dynamics proper of the Eulerian model was then successfully integrated in engine applications. In fact, the ACCI code-coupling interface permitted the temporal and spatial interconnection between two parallel-running CFD codes, namely the multiphase spray and the single-phase engine solvers. The method was finally applied on two identical engines mounted with different nozzles, which produces dissimilar behavior in emissions formation. The results were validated with experiments on a transparent spray chamber and two optically accessible engines. The simulations appeared promising in terms of prediction of mixture formation and combustion process. A correct trend in soot formation was reproduced and the analysis of the local flow field allowed understanding the effects of different nozzles on mixture formation. The comparison between soot luminosities revealed also a right prediction of the ignition and flame propagation behaviors between calculations and experiments. In order to obtain better agreements on integral values, the coupling method should be further tested with the future developments of soot formation and combustion models.

A step ahead in the enhancement of the method is the MPI-parallelization of the coupling routines, so that it could be effectively used in the industrial practice. The decrease in calculation time due to the cooperation of more computational domains could thus permit the simultaneous simulation of nozzle flow, Eulerian spray and engine without the adoption of a nozzle file.

The Eulerian spray could also be improved by the implementation of multi-component evaporation and species diffusion, as to improve the physical description of the standard and the upcoming bio fuels. Another step is also the development of variable droplets classes, in order to better describe the diameter decay from the nozzle orifice to the dilute spray region. An important issue could be as well the implementation of combustion processes in the Eulerian spray domain and eventually inside the injector body during the needle-closing run. The spreading of the combustion flame inside the nozzle orifice could help to understand the origin of carbon matters deposition and surface decay phenomena.

The presented coupling approach was developed and tested for common rail diesel engines. Nevertheless, the method could be easily adapted for DI gasoline engines, where the internal nozzle flow and the mixture formation process play an important role for the prediction of the combustion process.

Acknowledgments

My warmest thanks go to my supervisor Professor Bernhard Weigand for his guidance and encouragement during this study. With his vast knowledge, cordiality and manner of scientific thinking he always managed to make the right suggestions for an inestimable improvement of the work.

I extend my sincere thanks to my second supervisor Professor Dieter Munz. I were privileged to benefit from his comprehensive expertise in the field of numerical simulation.

This work was carried out at the "Group Research, Vehicle Powertrain – Emission Control" department of the Daimler AG in Stuttgart, Germany. I would like to thank all my colleagues for the great time I had in our group. I enjoyed the friendly atmosphere and the constant support. Especially I would like to thank Ulrich Michels for the priceless suggestions and the constant support in the development of this thesis. Special thanks also to Christian Krüger for his comprehensive expertise and his personable guidance. My thanks to Clemens Bauer for his previous works on database creation and to Rüdiger Steiner for his unbeatable good mood.

I would like to sincerely and personally thank Paul Wenzel and Markus Müller for sharing the PhD-student condition and the valuable discussions over a cup of coffee.

Special thanks to all the guys in AVL who helped me during the development of this thesis, above all Wilfried Edelbauer, Eberhard von Berg, Peter Sampl and Reinhard Tatschl. I express also my thanks to Audrey Cahill for revising the language of this thesis.

This work was supported by the European NICE project (New Integrated Combustion system for future passenger car Engines) under contract number TIP3-CT-2004-506201-NICE. Thanks to all the university and industry partners of the sub-project B.1 for the very fruitful discussions and the successful meetings.

Last but not least, I heartily thank my Kathi for bearing the three-years-long forced separation and the extenuating journeys between Graz and Stuttgart. One millions thanks would not be enough. Many thanks also to my sister Vale, my mother Nadia and my father Sergio for their support and for always encouraging me in everything I decide to do. A sincere thank to all my grand parents, Vinca, Maria and Tirsio: they make me proud of what I did. A final thanks to my grand father Peppino, who unfortunately won't hug me after the examination. I am thus sure you always see me from over there.

Appendix A
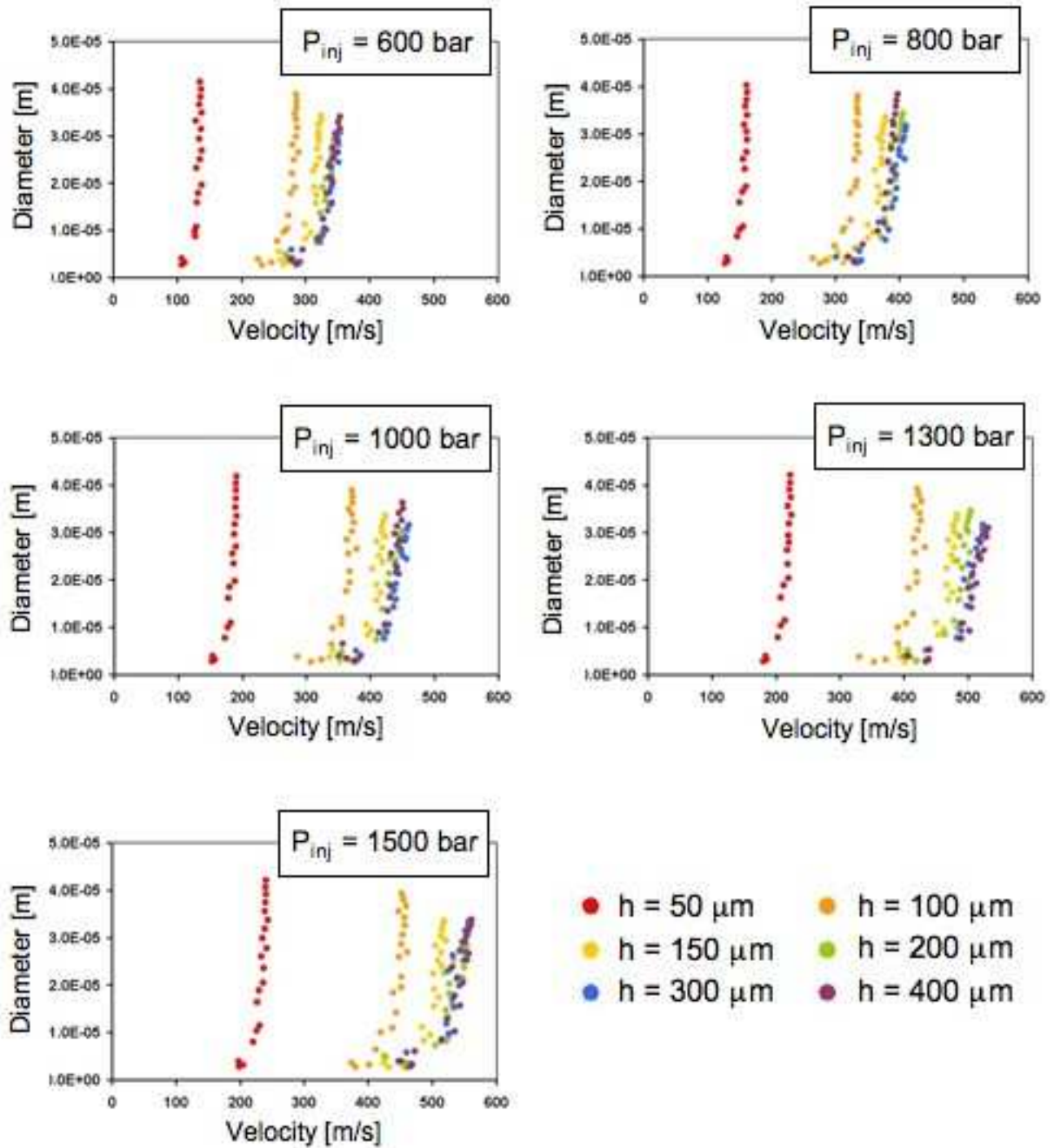
**Figure A.1:** Graphical representation of the Library for BR4000 engine with L'Orange injector.
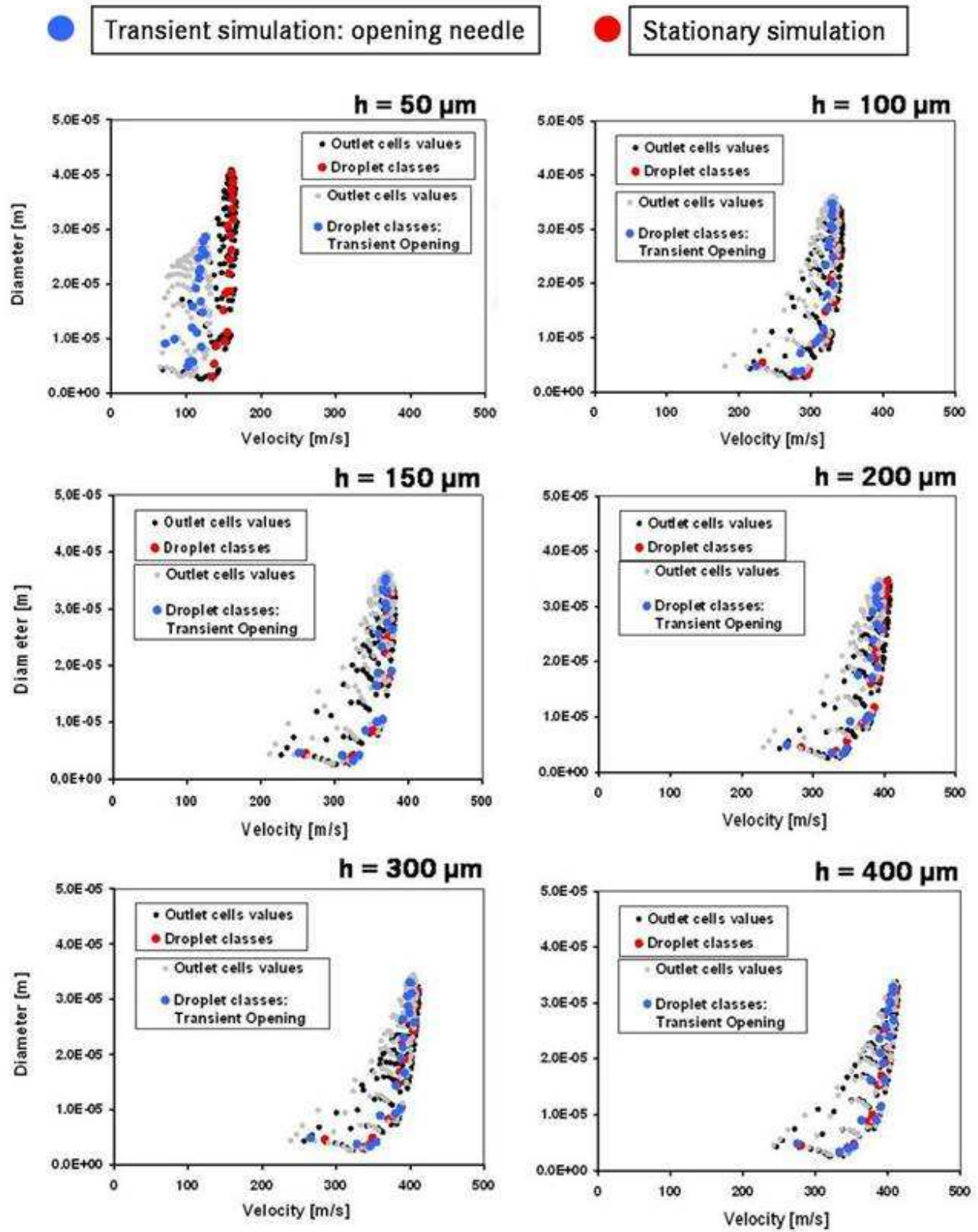
Figure A.2: Comparison between transient and stationary simulations for p_{inj}=800 bar at different needle lifts h: opening run.
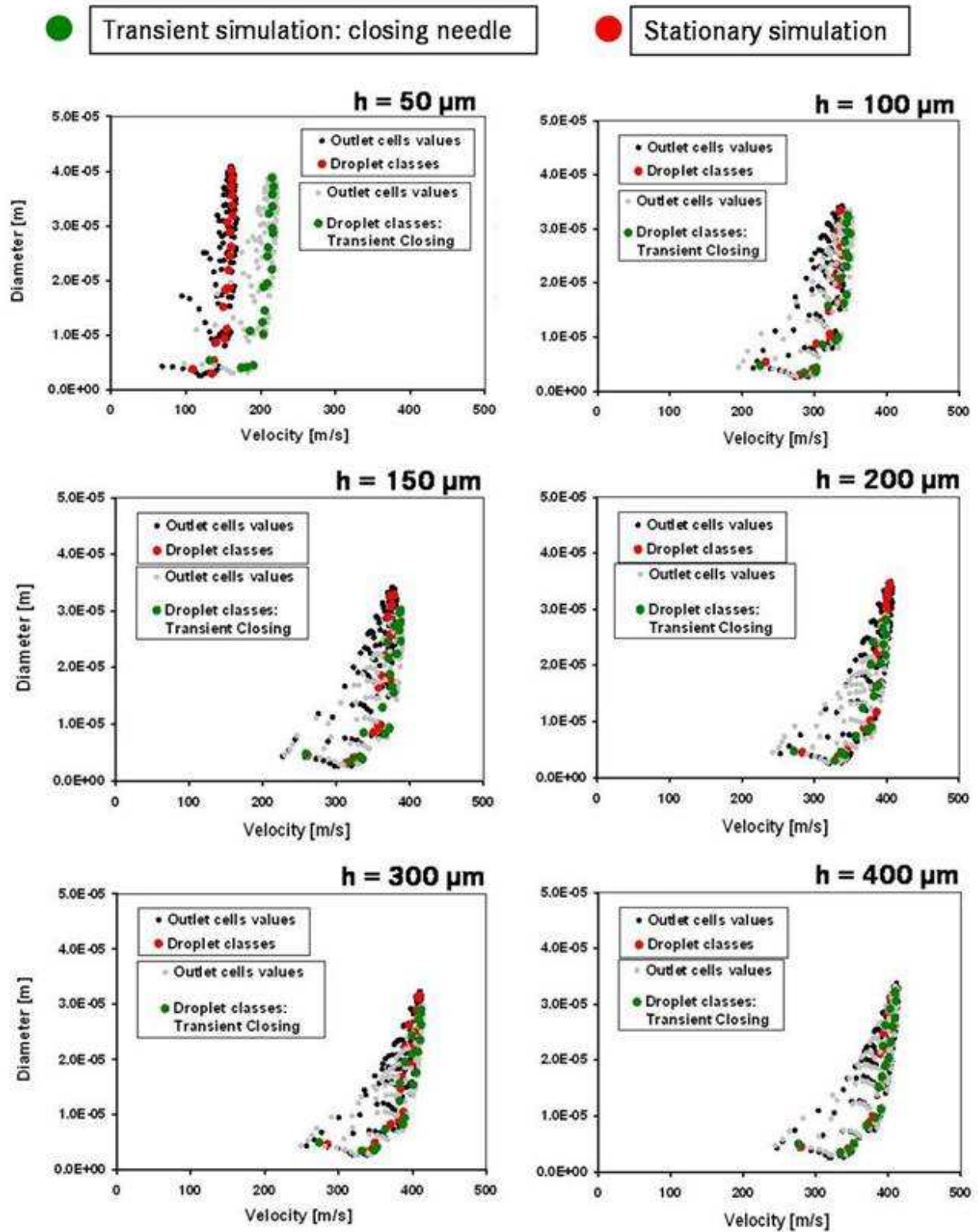
Figure A.3: Comparison between transient and stationary simulations for p_{inj}=800 bar at different needle lifts h: closing run.

References

[1]   Abramzon B., Sirignano W. A. (1988), "Droplet Vaporization Model for Spray Combustion Calculations", AIAA 26th Aerospace Sciences Meeting.

[2]   Alajbegovic A. (1999), "Three-dimensional cavitation calculations in nozzles", 2nd annual meeting institute for multifluid science and technology, Santa Barbara, California.

[3]   Alajbegovic A. (2001), "Large Eddy Simulation Formalism Applied to Multiphase Flows", FEDSM2001-18192, New Orleans, Louisiana.

[4]   Alajbegovic A., Drew D. A., Lahey R. T. (1999), "An Analysis of Phase Distribution and Turbulence in Dispersed Particle/Liquid Flows", Chem. Eng. Comm., 174 (1999) 85-133.

[5]   Alriksson M., Denbratt I. (2006), "Low Temperature Combustion in a Heavy Duty Diesel Engine Using High Levels of EGR", SAE-Paper 2006-01-0075.

[6]   Amsden A. A., O'Rourke P. J., Butler T. D. (1989), "KIVA-II – A Computer Program for Chemically Reactive Flows with Sprays", Los Alamos National Labs., LA-12560-MS.

[7]   AVL List GmbH (2002), "Multiphase Flow", FIRE Version 8 user manual, Graz, Austria.

[8]   AVL List GmbH (2005), "ACCI Coupling Interface", FIRE Version 8 user manual, Graz, Austria.

[9]   Bardina J., Ferziger J. H., Reynolds W. C. (1980), "Improved subgrid models for large eddy simulation", AIAA paper 80-1357.

[10]   Behzadi A., Issa R. I., Rusche H. (2001), "Effects of Turbulence on Inter-Phase Forces in Dispersed Flow", Proceedings of ICMF 2001, New Orleans.

[11]   Berg E. v., Edelbauer W., Tatschl R., Alajbegovic A., Volmajer M., Kegl B., Ganippa L. (2003), "Validation of a CFD model for coupled simulation of nozzle flow, primary fuel jet breakup and spray formation", Proceedings of ICES03 Conf., ASME ICE Division, Salzburg, Austria.

[12]   Berg, E. v., Alajbegovic A., Tatschl R., Krüger C., Michels U. (2001), "Multiphase modeling of Diesel sprays with the Eulerian/Eulerian approach", ILASS-Europe 2001, Zürich, Switzerland.

[13] Bianchi G. M., Pelloni P. (1999), "Modeling the Diesel Fuel Spray Break-up by Using a Hybrid Model", SAE Paper 1999-01-0226.

[14] Blessing M. (2004), "Untersuchung und Charakterisierung von Zerstäubung, Strahlausbreitung und Gemischbildung aktueller Dieseldirekteinspritzsysteme", Dissertation, UNI-Stuttgart.

[15] Brackbill U., Kothe D. B., Zemach C. (1992), "A Continuum Method for Modeling Surface Tension", J. Comput. Phys., 100:335-354.

[16] Brandstätter W., Landertshamer F., Pachler K. (1998), "Recent Findings Regarding High Pressure Diesel Spray Simulations", Proceedings of ILASS-Europe 1998, Manchester.

[17] Chan W. M., Gomez R. J., Rogers S. E., Buning, P. G. (2002), "Best Practices in Overset Grid Generation", AIAA Paper 2002-3191, 32nd AIAA Fluid Dynamics Conference, St. Louis, Missouri.

[18] Commission of the European Communities (2005), Directive 72/306/EEC and Directive ../../EC; MEMO/06/409 (2006).

[19] Crowe C. T., Sharma M. P., Stock D. E. (1977), "The Particle-Source-in-Cell Method for Gas Droplet Flow", ASME Journal of Fluids Engineering, Vol. 99, pp. 325-332.

[20] Drew D. A., Passman S. L. (1998), "Theory of Multicomponent Fluids", Springer, New York.

[21] Dukowicz J. K. (1979), "Quasi-Steady Droplet Phase Change in the Presence of Convection", Informal Report, LA 7997-MS, Los Alamos Scientific Laboratory.

[22] Dukowicz J. K. (1980), "A Particle Fluid Numerical Model for Liquid Sprays", Journal of Computational Physics, 35, pp. 229-253.

[23] Edelbauer W. (2003), "Coupled Simulation of Cavitating Nozzle Flow and Spray Formation", Diploma Thesis, TU Graz.

[24] Edelbauer W., Suzzi D., Sampl P., Tatschl R., Krueger C., Weigand B. (2006), "New Concept For on-line Coupling of 3D Eulerian and Lagrangian Spray Approaches in Engine Simulations ", ICLASS 06, Kyoto, Paper ID ICLASS06-234.

[25] Elghobashi S. (1991), "Particle-Laden Turbulent Flows: Direct Simulation and Closure Models", Applied Scientific Research, Band 48, pp. 301-314.

[26] Elliott L. (2005), "Making the Most of Boundaries - Fluid-Structural Interaction", Desktop Engineering, July 2005, Volume 10, Issue 11.

[27] Ferziger J. H., Peric M. (1999), "Computational Methods for Fluid Dynamics", 2nd Ed., Springer.

[28] Fluent Inc. (2006), "A Brief History of CFD", fluent.com web-homepage.

[29] Fraunhofer Institute for Algorithms and Scientific Computing SCAI (2005), "MpCCI Technical Reference", MpCCI Manual, Schloss Birlinghoven, Germany.

[30] Friedrich M., Weigand B. (2006), "Eulerian Multi-Fluid Simulation of Polydisperse Dense Liquid Sprays by the Direct Quadrature Method of Moments", ICLASS 06, Kyoto, Paper ID ICLASS06-121.

[31] Frössling N. (1938), "Evaporation of Falling Drops", Gerlands Beitr. Geophysik, Vol. 52, p. 170.

[32] Ganippa L. C., Bark G., Andersson S., Chomiak J. (2001), "The Structure of Cavitation and its Effect on the Spray Pattern in a Single-Hole Diesel Nozzle", SAE-Paper 2001-01-2008.

[33] Gupta H., Bracco S. V. (1978), "Numerical Computations of Two-Dimensional Unsteady Sprays for Application to Engines", AIAA Journal, Vol. 16, pp. 1053-1061.

[34] Hallmann M., Scheurlen M., Wittig S. (1995), "Computation of Turbulent Evaporating Sprays", Transaction of the ASME, 117.

[35] Hallmann, M., Scheurlen, M. and Wittig, S., Computation of Turbulent Evaporating Sprays, Transactions of the ASME, Vol.117, January 1995.

[36] Hermann A. (2008), "Modellbildung für die 3D-Simulation der Gemischbildung und Verbrennung in Ottomotoren mit Benzin-Direkteinspritzung", PhD Thesis, Karlsruhe.

[37] Heywood J. B. (1988), "Internal Combustion Engine Fundamentals", McGraw-Hill.

[38] Hirt C.W., Nichols, B.D. (1981), "Volume of Fluid (VOF) Method for the Dynamics of Free Boundaries", J. Comp. Phys. 39, pp. 201-225.

[39] Huh K.Y., Gosman, A.D. (1991), "A Phenomenological Model of Diesel Spray Atomisation", Proceedings of the International Conference on Multiphase Flows, Sept. 24-27, 1991, Tsukuba, Japan.

[40] Issa R., Oliveira P.J. (1995): "Numerical prediction of turbulent dispersion in two-phase jet flows. Two-Phase Flow Modelling and Experimentation".

[41] Janoske U., Lanfrit M. G., Dehning C., Habig R. (2005), "Gekoppelte Strömungs- und Strahlungsberechnung mit MpCCI", NAFEMS magazine, November 2005, p. 37.

[42] Kawaguti M. (1953), "Numerical Solution of the NS Equations for the Flow Around a Circular Cylinder at Reynolds Number 40", Journal of Phy. Soc. Japan, vol. 8, pp. 747-757.

[43] Koch T., König G., Wenzel P., Kemmner M., Jehle E. (2006), "Mechanisms of exhaust gas recirculation and other measures that can reduce the NOx emissions of commercial vehicle diesel engines". 7th International Symposium on Internal Combustion Diagnostics, Baden-Baden.

[44] Krüger C. (2001), "Validierung eines 1D-Spraymodells zur Simulation der Gemischbildung in direkteinspritzenden Dieselmotoren", Ph. D. Thesis, UNI Aachen.

[45] Kuan-yun Kuo K. (2005), "Principles of Combustion", Wiley-Interscience, 2. Edition.

[46] Lahey R. T. Jr., Drew D. A. (2000), "An Analysis of Two-Phase Flow and Heat Transfer Using a Multidimensional, Multi-Field, Two-Fluid Computational Fluid Dynamics (CFD) Model," Japan/US Seminar on Two-Phase Flow Dynamics, Santa Barbara, California.

[47] Lefebvre A. H. (1989), "Atomization and Sprays", Hemisphere Publishing Corporation.

[48] Leonerdo da Vinci (1509), "Del moto e misura dell'acqua", Original from Harvard University.

[49] Lopez de Bertodano M. A. (1998), "Two fluid model for two-phase turbulent jets", Nuclear Engineering and Design 179, pp. 65-74.

[50] Merker G. P., Schwarz C., Stiesch G., Otto F. (2001), "Verbrennungsmotoren. Simulation der Verbrennung und Schadstoffbildung", Teubner.

[51] Michels U. (2008), " Euler-Strahlmodell für Düseninnenströmung und Strahlausbreitung", PhD Thesis, Aachen.

[52] Michels U., Krüger C., König G., Blessing M., Schwarz V., Merker G. P. (2004), "Analysis of the Influence of the Injection Strategy on Cavitating Nozzle Flow, Spray Formation and Combustion in a Heavy Duty Truck Engine Effects on Spray and Mixture Formation", THIESEL 2004, Valencia.

[53] Münch K.-U., "Modellierung des Einspritzvorganges unter dieselmotorischen Bedingungen", A. Leipertz (Hrsg.), Berichte zur Energie- und Verfahrenstechnik (BEV), Heft 97.1, ESYTEC, Erlangen, S. 107-136.

[54] Munz C.-D., Westermann T. (2006), "Numerische Behandlung gewöhnlicher und partieller Differentialgleichungen", Springer.

[55] Nordin N. (2001), "Complex Chemistry Modeling of Diesel Spray Combustion", Ph. D. Thesis, Chalmers.

[56] O'Rourke P. J. (1981), "Collective Drop Effects on Vaporizing Liquid Sprays", Ph. D. Thesis, Princeton.

[57] O'Rourke P.J (1989), "Statistical Properties and Numerical Implementation of a Model for Droplet Dispersion in Turbulent Gas", Journal of Computational Physics, 83.

[58] O'Rourke P.J, Bracco F. V. (1980), "Modelling of Drops Interaction in Thick Sprays and a Comparison with Experiments", Stratified Charge Automotive Engineering Conference.

[59] O'Rourke P.J., Amsden, A.A. (1987), "The Tab Method for Numerical Calculation of Spray Droplet Break-up", SAE Paper 872089.

[60] Panton R.L. (1996), "Incompressible Flow", Second edition, John Wiley & Sons.

[61] Petersson N. A. (1999), "Hole-Cutting for Three-Dimensional Overlapping Grids", SIAM Journal on Scientific Computing, Vol. 21, No. 2, pp. 646-665.

[62] Pilch M., Erdman C.A. (1987), "Use of breakup time data and velocity history data to predict the maximum size of stable fragments for acceleration – induced breakup of liquid drop", Int. J. Multiphase Flow, Vol.13, No. 6, P. 741-757.

[63] Ranz W. E., Marshall W. R. (1952), "Evaporation from Drops: Part I+II", Chem. Eng. Prog., Vol. 48, pp. 141-146, pp. 173-180.

[64] Rao S. (2001), "A Probability Density Function Time-scale Model for Combustion Using Large Eddy Simulation", Master of Science Thesis, ERC Wisconsin-Madison.

[65] Rayleigh L. (1883), "Investigation of the character of the equilibrium on an incompressible heavy fluid of variable density", Proceedings of the London Mathematical Society, Vol. 14, pp. 170 - 177.

[66] Reeks M. W. (1991), "On a kinetic equation for the transport of particles in turbulent flows Phys.", Fluids A 3 (3), pp. 446-456.

[67] Reitz R. D. (1987), "Modeling Atomization Processes in High-Pressure Vaporizing Sprays", Atomization and Spray Technology, 3:309-337.

[68] Reitz R. D. (1994), "Computer Modeling of Sprays", Spray Technology Short Course, Pittsburgh.

[69] Richardson L. F., Gaunt J. A. (1927), "The Deferred Approach to the Limit," Philos. Trans. R. Soc. London Ser. A, Vol. 226, pp. 299-361.

[70] Rieber M. (2004), "Numerische Modellierung der Dynamik freier Phasengrenzflächen in Zweiphasen Strömungen", Ph. D. Thesis, Stuttgart.

[71] Rifkin J. (2000), "The Age of Access: How the Shift from Ownership to Access Is Transforming Capitalism", Ed. Tarcher.

[72] Roache P.J. (1993), "A Method for Uniform Reporting of Grid Refinement Studies," Proc. Of Quantification of Uncertainty in Computation Fluid dynamics, Edited by Celik, et al., ASME Fluids Engineering Division Spring Meeting, Washington D.C., June 230-240, ASME Publ. No. FED-Vol. 158.

[73] Robert Bosch GmbH, Kraftfahrzeugtechnik (2004), "Diesel-Speichereinspritzsystem Common Rail", Fachwissen Kfz-Technik, Dieselmotor-Management, ISBN-3-7782-2062-4.

[74] Sander W., Weigand B., Jellinghaus K., Beheng K. D. (2006), "Direct Numerical Simulation of Breakup Phenomena in Liquid Jets and of Colliding Raindrops", High Perfomance Computing in Science and Engineering '05, 129-142, Springer Verlag, Berlin.

[75] Schiller L., Naumann A. (1933), "A drag coefficient correlation", VDI Zeits. 77, 318-320.

[76] Schneider B. (2003), "Experimentelle Untersuchungen zur Spraystruktur in transienten, verdampfenden und nicht verdampfenden Brennstoffstrahlen unter Hochdruck", Ph. D. Thesis, Zürich.

[77] Schwarz V., König G., Dittrich P., Binder K. (1999), "Analysis of Mixture Formation, Combustion and Pollutant Formation in HD Diesel Engines using Modern Optical Diagnostics and Numerical Simulation", SAE Paper No. 1999-01-3647.

[78] Siegel R., Howell J. R. (1981), "Thermal radiation Heat Transfer", Hemisphere Publishing, Washington.

[79] Sirignano W. A., Rangel R. H., Dunn-Rankin D., Orme M. E. (1996), "Generation, Vaporization, and Combustion of Droplet Arrays and Streams", Recent Advances in Spray Combustion: Spray Atomization and Drop Burning Phenomena, Band 1, S. 327-380.

[80] Sivathanu Y. R., Faeth G. M. (1990), "Generalized State Relationships for Scalar Properties in Non-Premixed Hydrocarbon/Air Flames", Combustion and Flame, 82:211-230.

[81] Snir M., Otto S., Huss-Lederman S., Walker D., Dongarra J. (1998), "MPI - The Complete Reference, Volume 1, The MPI Core", MIT Press, 2. Edition.

[82] Sparrow E. M., Gregg J. L. (1958), "The variable Fluid Property Problem in free Convection", Trans. Of ASME, 80, pp. 879-886.

[83] Stahl M., Damaschke N., Tropea C. (2006), "Experimental Investigation of Turbulence and Cavitation Inside a Pressure Atomizer and Optical Characterization of the Generated Spray", ICLASS 06, Kyoto, Paper ID ICLASS06-116.

[84] Steger J. L., Dougherty F. C., Benek J. A. (1983), "A Chimera Grid Scheme", Advances in Grid Generation, K. N. Ghia and U. Ghia, eds., ASME FED-Vol. 5.

[85] Steiner R. (2004), "Modellbildung und strömungsmechanische Simulation der dieselmotorischen Verbrennung", Ph. D. Thesis, Karlsruhe.

[86] Steiner R., Bauer C., Krüger C., Otto F., Maas U. (2004), "3D-Simulation of DI-Diesel Combustion applying a Progress Variable Approach accounting for Complex Chemistry", SAE-Paper 2004-01-0106.

[87] Stralin P. (2004), "CFD Modeling of Mixture Formation in Direct Injected HCCI Engines", Licentiate Thesis, KTH Stockholm.

[88] Su T.F., Patterson M.A., Reitz R.D., Farrell, P.V. (1996), "Experimental and Numerical Studies of High Pressure Multiple Injection Sprays", SAE 960861.

[89] Suhs N. E., Rogers S. E., Dietz W. E. (2002), "PEGASUS 5: An Automatic Pre-Processor for Overset-Grid CFD", AIAA Paper 2002-3186, AIAA 32nd Fluid Dynamics Conference, St. Louis.

[90] Sun Han (2006), "On the Vaporization of Droplets at Elevated Pressure", Ph. D. Thesis, Stuttgart.

[91] Taylor G. I. (1950), "The instability of liquid surfaces when accelerated in a direction perpendicular to their planes", Proceedings of the Royal Society of London, Series A, Mathematical and Physical Sciences, Vol. 201, No. 1065, pp. 192 - 196.

[92] Thom A. (1933), "The Flow Past Circular Cylinders at Low Speeds", Proceedings of the Royal Society of London, A141, pp. 651-666, London.

[93] Versteeg H. K., Malalasekera W. (1995), "An Introduction to Computational Fluid Dynamics. The Finite Volume Method", Longman.

[94] Wenzel P., Gezgin A., Steiner R., Krüger C., Netzell K., Lehtiniemi H., Mauss F. (2006), "Modeling of the Soot Particle Size Distribution in Diesel Engines", THIESEL 2006, Valencia.

[95] Williams F. A. (1986), "Combustion Theory", 2nd Edition, Addison-Wesley Publishing Co., Reading, MA.

[96] Wilms J. (2005), "Evaporation of Multicomponent Droplets", Ph. D. Thesis, Stuttgart.

[97] Youngs D. L. (1982), "Time-Dependent Multi-Material Flow with Large Fluid Distortion", in K. W. Morton and M. J. Baines editors, Numerical Methods for Fluid Dynamics, Academic Press.

Lebenslauf

SUZZI DANIELE

- GEBURTSDATUM	**04.11.1978**
- GEBURTSORT	**Bologna, Italien**
- STAATSANGEHÖRIGKEIT	**Italien**
- E-MAIL	**daniele.suzzi@gmx.net**

Ausbildung

07/2004 – 04/2009
Doktorarbeit an der Universität Stuttgart (ITLR – Institut für Thermodynamik der Luft- und Raumfahrt, Prof. B. Weigand).

09/1997 - 10/2003 (Studium)
Universitá degli Studi di Bologna
Studiengang: Allgemeiner Maschinenbau
Abschluss: Diplom-Ingenieur

09/1993 - 07/1997 (Schulbildung)
„Liceo Scientifico E. Fermi" (Wissenschaftliches Gymnasium), Bologna
Abschluss: Mathematik und Physik

Berufserfahrung

10/2008 - heute
Research Center Pharmaceutical Engineering GmbH, *Graz, Österreich*
Abteilung: Virtual Pharmaceutical Engineering (Area I)

06/2007 - 09/2008
Das virtuelle Fahrzeug Kompetenzzentrum (VIF – The virtual vehicle competence centre), *Graz, Österreich*
Abteilung: Advanced Aerodynamics (Area B)

07/2004 - 06/2007
DaimlerChrysler AG, *Stuttgart, Deutschland*
Abteilung: Forschung Fahrzeugaufbau und Antriebe / Simulation und Aufladung – GR/VPE (Group Research / Vehicle Powertrain, Emissions Control)

01–06/2004
AVL List, *Graz, Österreich*
Abteilung: AST – Advanced Simulation Technologies